

*Synthesis and Surface Modification
of Semiconductor Nanocrystals*

Dissertation

Zur Erlangung des Grades

Doktor der Naturwissenschaften

Am Fachbereich

Chemie, Pharmazie und Geowissenschaften
der Johannes Gutenberg-Universität Mainz

vorgelegt von

Renguo Xie

geboren in Jilin Province / P. R. China

Mainz, 2006

Table of Contents

1. Introduction -----	1
2. Synthesis and properties of CdSe nanocrystals-A general review -----	5
2.1 Electronic and optical properties of semiconductors-----	5
2.1.1 Bulk Semiconductors-----	5
2.1.2 Nanocrystalline Semiconductors-----	5
2.2 Synthesis and growth of nanocrystals-----	10
2.3 Methods for the synthesis of semiconductor nanocrystals-----	12
2.3.1 Sol Process -----	12
2.3.2 Micelles-----	13
2.3.3 Chemical vapor deposition-----	14
2.4 Growth mechanism of nanostructures of different shapes-----	15
2.4.1 Effect of monomer concentration-----	15
2.4.2 Solution-liquid-solid and solution-liquid-solid mechanism-----	17
2.5 Chemical surface modification of nanocrystals-----	18
2.5.1 Inorganic surface passivation-----	18
2.5.2 Surface modification by functionalized molecules-----	20
2.6 Applications-----	22
3. Experimental -----	25
3.1 Approaches for nanocrystal synthesis -----	25
3.2 Chemicals-----	36
3.3 Synthesis methods-----	27
3.3.1 CdSe nanocrystals-----	27
3.3.2 Shell growth on CdSe core nanocrystals-----	27
3.4 Spectroscopic techniques-----	28
3.4.1 Absorption-----	28
3.4.2 Fluorescence-----	28
3.4.3 NMR-----	29
3.5 Techniques for structural characterization-----	29
3.5.1 TEM-----	29
3.5.2 XRD-----	29
3.5.3 EDX-----	30
3.5.4 DLS-----	30

4. Synthesis and characterization of type-I multi-shell nanocrystals	31
4.1 Introduction	31
4.2 Results and discussion	33
4.2.1 Reaction conditions for shell growth of different compounds	33
4.2.2 Structure characterization	34
4.2.3 Optical properties	42
4.2.4 Chemical characterization	47
4.2.4.1 Chemical stability	47
4.2.4.2 Photochemical stability	48
4.2.4.3 Thermal stability	50
4.3 Conclusion	51
4.4 Preparation methods	52
5. Synthesis and characterization of type-II ZnTe/CdX (X= S, Se, Te) core/shell nanocrystals	55
5.1 Introduction	55
5.2 Results and discussion	56
5.2.1 Structure characterization	57
5.2.1.1 TEM	57
5.2.1.2 Size distribution	58
5.2.1.3 XRD	60
5.2.1.4 EDX	61
5.2.2 Optical properties	62
5.2.2.1 Absorption	62
5.2.2.2 Photoluminescence	64
5.3 Conclusion	68
5.4 Preparation methods	69
6. Synthesis of various CdSe architectures	71
6.1 Introduction	71
6.2 Results and discussion	72
6.2.1 Spherical core/shell nanocrystals	73
6.2.1.1 Structural characterization	73
6.2.1.2 Optical properties	75
6.2.2 Pyramidal nanocrystals	77
6.2.3 Tetrapod nanocrystals	78

6.2.3.1	Structural characterization	79
6.2.3.2	Tetrapodal nanocrystals with different arm shapes	83
6.2.3.3	Optical properties	85
6.2.4	Nail-shaped nanocrystals	86
6.2.4.1	Structural characterization	86
6.2.4.2	Optical properties	90
6.2.5	Chess-figure shaped nanocrystals	93
6.2.6	Y-figure shaped nanocrystals	95
6.3	Conclusion	97
6.4	Preparation methods	99
6.4.1	Synthesis of zinc blende cores	99
6.4.1.1	ZnTe seeds	99
6.4.1.2	ZnSe seeds	99
6.4.1.3	ZnS seeds	99
6.4.2	Synthesis of CdSe architectures using different cubic cores	100
6.4.2.1	Injection procedures	100
A)	Injection solutions	100
B)	Three injection methods	100
C)	Calculation of injected amounts	100
6.4.2.2	Synthesis of spherical CdSe nanocrystals	100
6.4.2.3	Synthesis of pyramidal CdSe nanocrystals	101
6.4.2.4	Synthesis of tetrapod CdSe nanocrystals with rod shaped arms	101
6.4.2.5	Synthesis of tetrapod CdSe nanocrystals with nail shaped arms	102
6.4.2.6	Synthesis of nail shaped CdSe nanocrystals by ZnS, ZnSe or ZnTe nanocrystals	102
6.4.2.7	Synthesis of “chess-figure” shaped CdSe nanocrystals using ZnSe or ZnTe seeds	102
6.4.2.7	Synthesis of “Y” shaped CdSe nanocrystals	103
7.	Organic surface modification of nanocrystals	104
7.1	Introduction	104
7.2	Transfer into the aqueous phase by various ligands	105
7.2.1	Mercaptopropionic acid (MPA)	105
7.2.2	Peramino- β -cyclodextrin	107

7.2.2.1 Structure and size of water soluble multi-shell nanocrystals---	108
7.2.2.2 Optical properties of water soluble multi-shell nanocrystals---	119
7.2.2.3 Conclusion-----	121
7.2.3 Aminoethanethiol (AET) -----	122
7.2.3.1 Transfer into the aqueous phase -----	122
7.2.3.2 Coupling to Cy5-dye molecules-----	123
7.3 Calixarene functionalized nanocrystals-----	127
7.3.1 Calixarene with four amino groups-----	127
7.3.2 Calixarene with four thiol groups-----	129
7.4 Preparation methods -----	131
8. Summary-----	134
References-----	136
Publication list-----	147
Curriculum Vitae-----	148
Acknowledgments-----	149

1. Introduction

The last decade has witnessed an exponential growth of activities in the field of nanoscience and nanotechnology worldwide, driven both by the excitement of understanding new science and by the potential hope for applications and economic impacts. The largest activity in this field up to date has been in the synthesis and characterization of new materials consisting of particles with dimensions in the order of a few nanometers, so-called nanocrystalline materials. ^[1-8] Semiconductor nanomaterials such as III/V or II/VI compound semiconductors exhibit strong quantum confinement behavior in the size range from 1 to 10 nm. Therefore, preparation of high quality semiconductor nanocrystals has been a challenge for synthetic chemists, leading to the recent rapid progress in delivering a wide variety of semiconducting nanomaterials.

Semiconductor nanocrystals, also called quantum dots, possess physical properties distinctly different from those of the bulk material. Typically, in the size range from 1 to 10 nm, when the particle size is changed, the band gap between the valence and the conduction band will change, too. In a simple approximation a particle in a box model has been used to describe the phenomenon^[9]: at nanoscale dimensions the degenerate energy states of a semiconductor separate into discrete states and the system behaves like one big molecule. The size-dependent transformation of the energy levels of the particles is called “quantum size-effect”. Quantum confinement of both the electron and hole in all three dimensions leads to an increase in the effective bandgap of the material with decreasing crystallite size. Consequently, both the optical absorption and emission of semiconductor nanocrystals shift to the blue (higher energies) as the size of the particles gets smaller. This color tuning is well documented for CdSe nanocrystals whose absorption and emission covers almost the whole visible spectral range. As particle sizes become smaller the ratio of surface atoms to those in the interior increases, which has a strong impact on particle properties, too. Prominent examples are the low melting point ^[8] and size/shape dependent pressure resistance ^[10] of semiconductor nanocrystals.

Given the size dependence of particle properties, chemists and material scientists now have the unique opportunity to change the electronic and chemical properties of a material by simply controlling the particle size. In particular, CdSe

nanocrystals have been widely investigated. Mainly due to their size-dependent optoelectronic properties ^[11, 12] and flexible chemical processibility ^[13], they have played a distinguished role for a number of seminal studies ^[11, 12, 14, 15]. Potential technical applications have been discussed, too. ^[8, 16-27]

Improvement of the optoelectronic properties of semiconductor nanocrystals is still a prominent research topic. One of the most important approaches is fabricating composite type-I core-shell structures which exhibit improved properties, making them attractive from both a fundamental and a practical point of view. Overcoating of nanocrystallites with higher band gap inorganic materials has been shown to increase the photoluminescence quantum yields by eliminating surface nonradiative recombination sites. ^[28] Particles passivated with inorganic shells are more robust than nanocrystals covered by organic ligands only and have greater tolerance to processing conditions necessary for incorporation into solid state structures or for other applications. Some examples of core-shell nanocrystals reported earlier include CdS on CdSe ^[29], CdSe on CdS, ^[30] ZnS on CdS, ^[31] ZnS on CdSe ^[28, 32], ZnSe on CdSe ^[33] and CdS/HgS/CdS ^[34]. The characterization and preparation of a new core-shell structure, CdSe nanocrystals overcoated by different shells (CdS, ZnS), is presented in chapter 4.

Type-I core-shell structures as mentioned above greatly improve the photoluminescence quantum yield and chemical and photochemical stability of nanocrystals. The emission wavelengths of type-I core/shell nanocrystals typically only shows a small red-shift when compared to the plain core nanocrystals. ^[30, 31, 35] In contrast to type-I core-shell nanocrystals, only few studies have been conducted on colloidal type-II core/shell structures ^[36-38] which are characterized by a staggered alignment of conduction and valence bands giving rise to a broad tunability of absorption and emission wavelengths, as was shown for CdTe/CdSe core-shell nanocrystals. ^[36] The emission of type-II core/shell nanocrystals mainly originates from the radiative recombination of electron-hole pairs across the core-shell interface leading to a long photoluminescence lifetime. Type-II core/shell nanocrystals are promising with respect to photoconduction or photovoltaic applications as has been discussed in the literature. ^[39] Novel type-II core-shell structures with ZnTe cores are reported in chapter 5.

The recent progress in the shape control of semiconductor nanocrystals opens new fields of applications. For instance, rod shaped CdSe nanocrystals can enhance

the photo-electro conversion efficiency of photovoltaic cells, ^[40, 41] and also allow for polarized emission in light emitting diodes. ^[42, 43] Shape control of anisotropic nanocrystals can be achieved by the use of surfactants, ^[44, 45] regular or inverse micelles as regulating agents, ^[46, 47] electrochemical processes, ^[48] template-assisted ^[49, 50] and solution-liquid-solution (SLS) growth mechanism. ^[51-53] Recently, formation of various CdSe nanocrystal shapes has been reported by the groups of Alivisatos ^[54] and Peng, ^[55] respectively. Furthermore, it has been reported by the group of Prasad ^[56] that noble metal nanoparticles can induce anisotropic growth of CdSe nanocrystals at lower temperatures than typically used in other methods for preparing anisotropic CdSe structures. Although several approaches for anisotropic crystal growth have been reported by now, developing new synthetic methods for the shape control of colloidal semiconductor nanocrystals remains an important goal. Accordingly, we have attempted to utilize a crystal phase control approach for the controllable synthesis of colloidal ZnE/CdSe (E = S, Se, Te) heterostructures in a variety of morphologies. The complex heterostructures obtained are presented in chapter 6.

The unique optical properties of nanocrystals make them appealing as *in vivo* and *in vitro* fluorophores in a variety of biological and chemical investigations, in which traditional fluorescence labels based on organic molecules fall short of providing long-term stability and simultaneous detection of multiple emission colours [References]. The ability to prepare water soluble nanocrystals with high stability and quantum yield has led to promising applications in cellular labeling, ^[57, 58] deep-tissue imaging, ^[59, 60] and assay labeling ^[61, 62]. Furthermore, appropriately solubilized nanocrystals have been used as donors in fluorescence resonance energy transfer (FRET) couples. ^[63-65] Despite recent progress, much work still needs to be done to achieve reproducible and robust surface functionalization and develop flexible (bio-) conjugation techniques. Based on multi-shell CdSe nanocrystals, several new solubilization and ligand exchange protocols have been developed which are presented in chapter 7.

The organization of this thesis is as follows: A short overview describing synthesis and properties of CdSe nanocrystals is given in chapter 2. Chapter 3 is the experimental part providing some background information about the optical and analytical methods used in this thesis. The following chapters report the results of this work: synthesis and characterization of type-I multi-shell and type-II core/shell nanocrystals are described in chapter 4 and chapter 5, respectively. In chapter 6, a

high-yield synthesis of various CdSe architectures by crystal phase control is reported. Experiments about surface modification of nanocrystals are described in chapter 7. At last, a short summary of the results is given in chapter 8.

2. Synthesis and properties of CdSe nanocrystals-A general review

2.1 Electronic and optical properties of semiconductors

2.1.1 Bulk semiconductors

Macrocrystalline semiconductors, free of defects, consist of three-dimensional networks of ordered atoms in which the large number of atoms leads to the generation of sets of molecular orbitals with very similar energies which effectively form a continuum. At 0 K the lower energy levels, or valence band, are filled with electrons, while the conduction band consisting of the higher energy levels is unoccupied. These two bands are separated by an energy gap (E_g), the magnitude of which is a characteristic property of the bulk macrocrystalline material. Materials normally considered as semiconductors typically exhibit band gaps in the range 0.3-3.8 eV. At temperatures above 0 K, electrons in the valence band may receive enough thermal energy to be excited across the band gap into the conduction band. An excited electron in the conduction band together with the resulting hole in the valence band forms an "electron-hole pair". The charge carriers in a semiconductor can form a bound state when they approach each other in space. This bound electron-hole pair, known as a Wannier exciton, is delocalized within the crystal lattice and experiences a screened Coulombic interaction. The Bohr radius of the bulk exciton is given by eq. 1 (ϵ represents the bulk optical dielectric coefficient, e the elementary charge, and m_e^* and m_h^* the effective mass of the electron and hole, respectively).(see: Reference [66])

$$a_B = \frac{\hbar^2 \epsilon}{e^2} \left[\frac{1}{m_e^*} + \frac{1}{m_h^*} \right] \quad (1)$$

2.1.2 Nanocrystalline semiconductors

Quantum confinement is a widely used terminology in the study of nanocrystals. In a bulk crystal, the properties of the material are independent of the size and are only chemical composition-dependent. As the size of a crystal decreases to the nanometer regime, the size of the particle begins to modify the properties of the crystal. The electronic structure is altered from the continuous electronic bands to discrete or quantized electronic levels. As a result, the continuous optical transitions between the electronic bands become discrete and the properties of the nanomaterial become size-dependent. Two fundamental factors, both related to the size of the

individual nanocrystal, distinguish their behavior from the corresponding macrocrystalline material. The first is the high dispersity (large surface/volume ratio) associated with the particles, with both the physical and chemical properties of the semiconductor being particularly sensitive to the surface structure. The second factor is the actual size of the particle, which can determine the electronic and physical properties of the material. The optical absorption spectra of nanocrystalline compound semiconductors ^[1-8] show blue shifts in their absorption edge as the size of the particles decreases, which cannot be explained by classical theory. ^[11, 67, 68] Such size dependent optical properties are examples of the size quantization effect which occurs when the size of the nanoparticle is smaller than the bulk-exciton Bohr radius, a_B (eq 1), of the semiconductor. ($a_B = 56 \text{ \AA}$ for CdSe) (Text from reference: [66])

For semiconductor nanoparticles the electron and hole are closer together than in the macrocrystalline material, and so the Coulombic interaction between electron and hole cannot be neglected. Based on the basis of the effective mass approximation, quantum mechanical calculations of a “particle in a box” give series of discrete quasi-molecular energy levels. Thus, for electrons the energy levels are located within the conduction band, and for holes the energy levels are located within the valence band. According to the energy of the transition from the highest hole state to the lowest electronic state in the nanocrystal, Brus showed ^[3, 67, 68] for CdE (E) (S or Se) nanocrystallites that the size dependence on the energy of the first electronic transition of the exciton (or the band gap shift with respect to the typical bulk value) can be approximately calculated using

$$\Delta E = E_{\text{gap}} + E(h) + E(e) = E_{\text{gap}} + \hbar^2\pi^2/(2R^2)[1/m_h^* + 1/m_e^*] - 1.8e^2/\epsilon R \quad (2)$$

where E_{gap} is the energy gap of the bulk semiconductor. $E(h)$, $E(e)$ are the confinement energies for hole and electron respectively, R is the radius of the nanocrystal, m_h^* , m_e^* are the effective masses of the hole and electron, respectively. $1.8e^2/\epsilon R$ is the term due to Coulomb interaction of electron and hole, e the charge of the electron, and ϵ the dielectric constant. $E(h)$ is higher than $E(e)$ for the reason of stronger curvature of the energy dispersion of the conduction band with respect to the valence band or, in other words, because m_h^* is higher than m_e^* (for example, $m_h^* = 0.5 m_e^0$, $m_e^* = 0.119 m_e^0$ for CdSe).^[69] Equation 2 is illustrated by figure 2.1.1

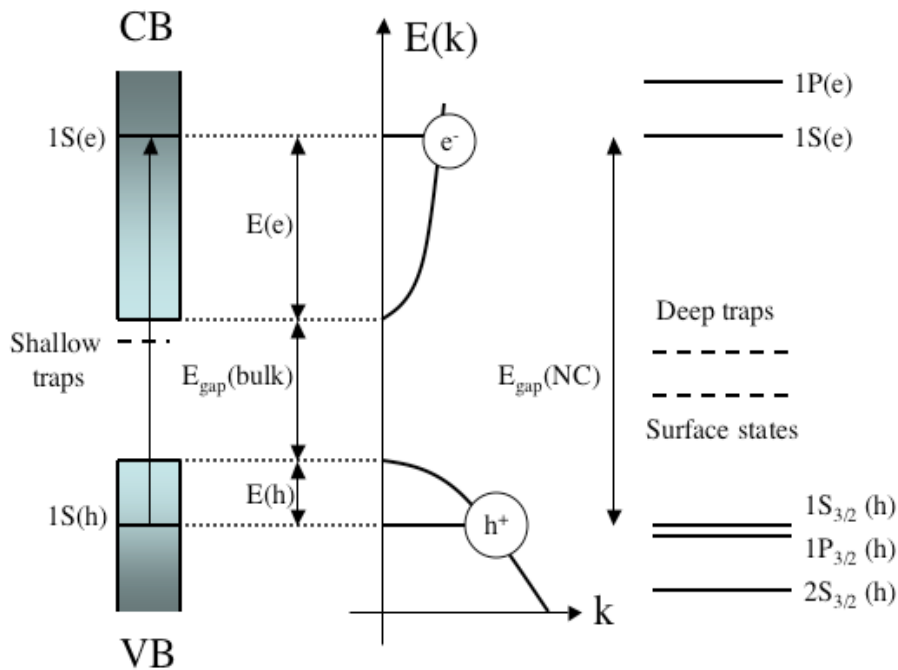


Figure 2.1.1 Electronic state diagram of nanocrystalline semiconductor (left part) schematically represents eq. 2. The graph in the middle shows the dispersion of the energy of the conduction and valence bands, respectively, of the semiconductor with direct energy gap in k – space; k is the wave vector of the reciprocal space. The right part represents the electron and hole states of CdSe nanocrystal in the strong confinement regime. The dashed lines represent surface states and deep traps of the nanocrystal. After reference [69, 70]

In equation 2 the Coulomb term shifts the first excited electronic state to lower energy, scaling with R^{-1} , while the quantum localization terms shift the state to higher energy, scaling with R^{-2} . Consequently, the first excitonic transition (or band gap) increases in energy with decreasing particle diameter. This prediction has been confirmed experimentally for a wide range of semiconductor nanocrystallites, [1, 3, 6] with a blue shift in the onset of the absorption of light being observed with decreasing particle diameter. Moreover, the valence and conduction bands in nanocrystalline materials consist of discrete sets of electronic levels and can be viewed as a state of matter between that of nanocrystal and bulk material. (Text from reference: [66]) In fact, the transitions according to the calculated energy levels are found in the absorption spectrum of CdSe nanocrystals as presented in figure 2.1.2.

Other theoretical methods have been used to explain the size-dependent electronic properties of semiconductor nanoparticles. Descriptions of the different

theoretical methods can be found in the published work of Brus, ^[11, 67, 68] Weller et al., ^[71, 72] Nosaka, ^[73] Wang and Herron, ^[74] among others.

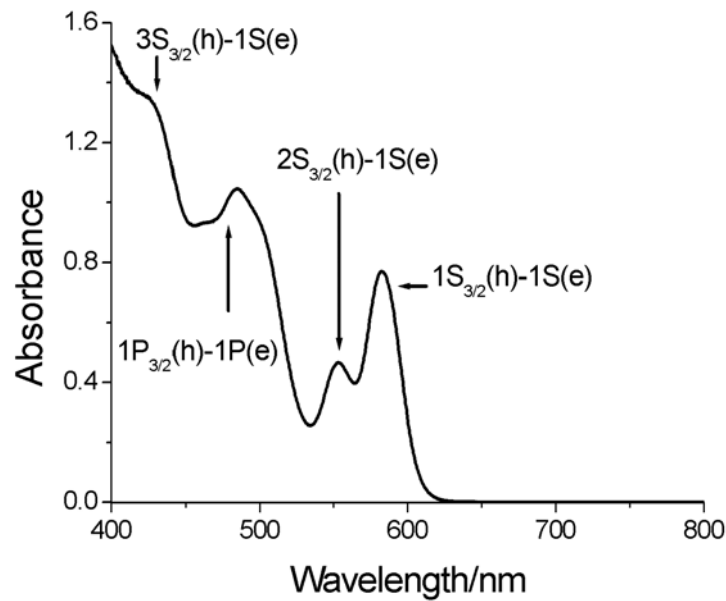


Figure 2.1.2: Absorption spectrum of CdSe nanocrystals prepared in this thesis with the resolved transitions (see also Figure 2.1.1).

The optical properties of semiconductor nanoparticles have been studied extensively with different optical techniques and theoretical considerations. ^[8, 9, 16, 75-77] The optical absorption spectrum of a nanocrystalline semiconductor provides an accessible and straightforward method for the evaluation of quantum size effects.

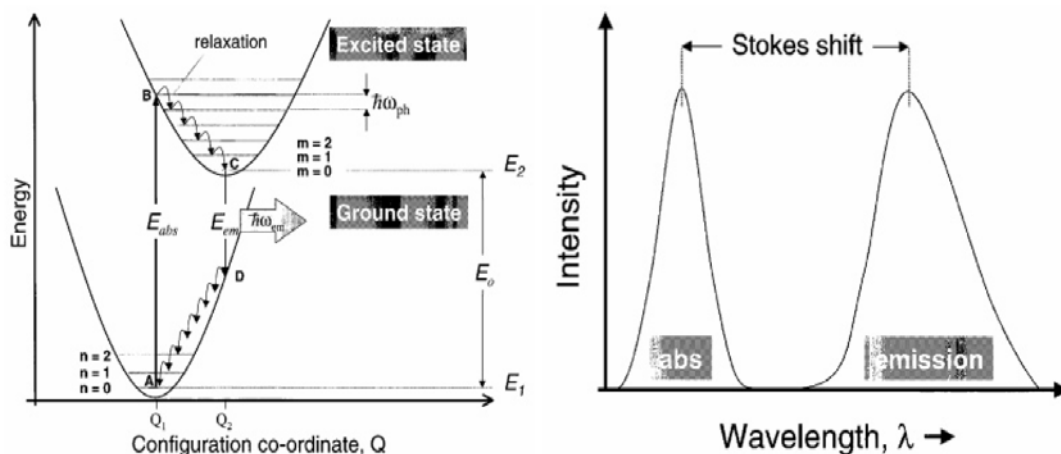


Figure 2.1.3 (Left) Illustration of absorption and emission transitions as well as the vibrational levels in a configurational coordinate diagram. (Right) Illustration of optical absorption, a PL emission peak and the Stokes shift for a nanocrystal. After reference [9]

Figure 2.1.3 shows an illustration of the optical absorption and emission transitions as well as the vibrational levels in a configurational coordinate diagram. Furthermore, it illustrates the optical absorption of the lowest transition, the photoluminescence emission peak, and the Stokes shift for a nanocrystal. The reason for the resonant Stokes shift is the splitting of the $1S_{3/2}(h) - 1S(e)$ lowest excitonic state due to asymmetry of the wurtzite structure of the nanocrystals and electron-hole interaction. After excitation by light, the optical transitions can occur through different ways of electronic relaxation such as nonresonant, resonant, and interband transitions, which correspond to transition energies below, equal to, and above the band gap of the semiconductor, respectively. [78] Sometimes, in fluorescence spectra of nanocrystals along with the maximum peak a broad red shifted peak is observed (especially for small particle size). This peak was assigned to the “trap fluorescence” introduced by surface states/traps of poorly passivated nanocrystals. [79]

As shown in figure 2.1.2, optical absorption spectroscopy is the most commonly used technique in exploring the quantum effects of semiconductor nanoparticles. By using this method, one can observe the development of discrete features in the spectra and the enlargement of the energy gap in semiconductor nanocrystals. [8, 16, 75] The discrete optical transitions in the absorption spectra have been observed in many monodispersed nanoparticle systems. [16, 80, 81]

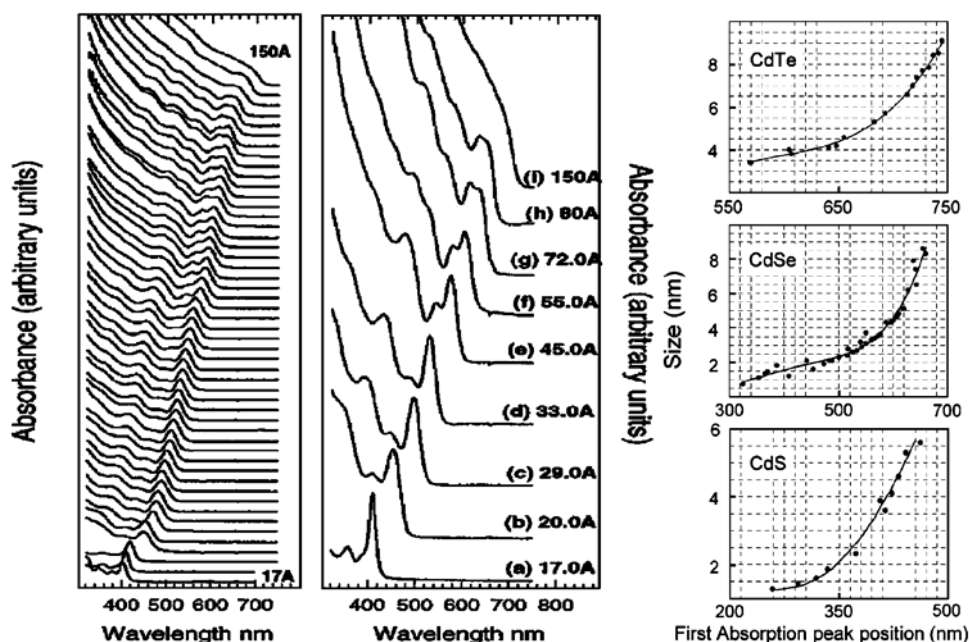


Figure 2.1.4 (Left, middle) Observation of discrete electronic transitions in optical absorption for a series of sizes of monodispersed CdSe nanocrystals. After reference [16] (Right) First absorption peak change versus the size of the nanoparticle. After references [16, 80]

Figure 2.1.4 shows the absorption spectra for a series of CdSe nanoparticles of different sizes. In addition, it shows how the first absorption peak changes as the nanoparticle size changes for CdSe, CdS, and CdTe nanocrystals. The absorption spectra show a continuous red shift as the size of the particle increases, and up to 10 discrete optical transitions can be resolved, which correspond to the transitions between the discrete energy levels of the nanocrystals as shown in figure 2.1.1. However, often the discrete states are not readily visible in the absorption spectra due to inhomogeneous broadening, which can be traced to the size, shape, and surface defect distributions in the nanoparticles.

A high-quality absorption spectrum of monodisperse nanocrystals can be used to calculate and calibrate the size and size distribution of the synthesized nanocrystals. On the basis of research on model semiconductor CdSe nanoparticle systems, the correlation between the first excitonic peak position and the size taken from the TEM or X-ray diffraction patterns provides reliable optical sizing of CdSe nanocrystals. The absorption of nanocrystals was also employed for evaluation of the scaling laws for the concentration,^[82] the absorption cross-section^[83] and extinction coefficients^[82, 84] of the CdSe nanocrystals as well as the oscillator strength of the transitions close to the band edge.^[80, 84, 85]

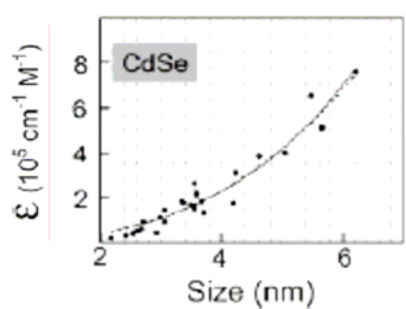


Figure 2.1.5 Extinction coefficient of particles at the first absorption peak position for CdSe nanocrystals as a function of size. After reference [80]

2.2 Synthesis and growth of nanocrystals

The chemical growth of nanometer-sized materials inevitably involves the process of particle formation from solution.^[86, 87] For a particular solvent, there is certain solubility for a solute, whereby addition of any excess solute will result in formation of nanocrystals. Therefore, for nucleation to occur, the solution must be supersaturated either by directly dissolving the solute at higher temperature and then

cooling to low temperature, or by adding the necessary reactants to produce a supersaturated solution during the reaction. [16, 86] The precipitation process then basically consists of a nucleation step followed by particle growth stages.

Generally, there are three kinds of nucleation processes: homogeneous nucleation, heterogeneous nucleation, and secondary nucleation. Homogeneous nucleation occurs in the absence of a solid interface by combining solute molecules to produce nuclei. Homogeneous nucleation happens due to the driving force of thermodynamics because the supersaturated solution is not stable in energy. The overall free energy change, ΔG , is the sum of the free energy due to the formation of a new volume and the free energy due to the new surface created. For spherical particles

$$\Delta G = - (4/V) \pi r^3 k_B T \ln(S) + 4\pi r^2 \gamma \quad (3)$$

where V is the molecular volume of the nanocrystals, r is the radius of the nuclei, k_B is the Boltzmann constant, S is the saturation ratio, and γ is the surface free energy per unit surface area. If $S > 1$, ΔG has a positive maximum at a critical size r^* . The critical nuclei size r^* can be obtained by setting $d(\Delta G/dr) = 0$.

$$r^* = 2V\gamma / 3 k_B T \ln(S) \quad (4)$$

According to equation (4), the Gibbs-Thomson equation is given as follows: [86]

$$S_r = S_b \exp(2\sigma V_m / rRT) \quad (\text{see reference [69]}) \quad (5)$$

This relation defines the size dependent growth rate of nanocrystals.

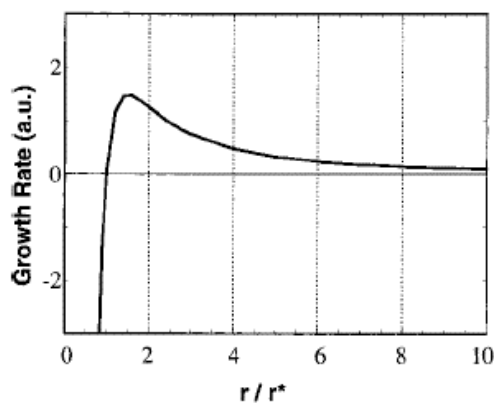


Figure 2.2.1 Variation of the growth rate versus size according to the model of Sigimoto. The figure is adopted from reference [86].

Figure 2.2.1 shows the growth rate of CdSe nanocrystals for a fixed monomer concentration. [86] It is found that very small particles have a negative growth rate, while larger ones have a positive growth rate and they are growing.

Focusing of the size distribution occurs when r is slightly larger than r^* because smaller nanocrystals grow faster than larger ones. When the monomer concentration is depleted, Ostwald ripening (defocusing) takes place because the smaller nanocrystals are shrinking while larger ones are growing.^[87]

2.3 Methods for the synthesis of semiconductor nanocrystals

2.3.1 Sol Process

As discussed in the above section, a general scheme for preparing monodisperse nanostructures requires a single, temporally short nucleation event followed by slower growth on the existing nuclei.^[75] This may be achieved by rapid addition of reagents into a reaction vessel containing a hot, coordinating solvent. Rapid addition of reagents to the reaction vessel raises the precursor concentration above the nucleation threshold. The temperature of the solution is sufficient to decompose the reagents, resulting in a supersaturation of particles in solution. Upon a short nucleation burst, the concentration of these species in solution drops below the critical concentration for nucleation. As long as the consumption of the reactants by the growth of the particles is not exceeded by the rate of precursor addition to the solution, no new nuclei form and the additional material can only add to the existing nuclei. Because the growth of any given nanocrystal is similar to that of all others, the initial size distribution is largely determined by the time over which the nuclei are formed and begin to grow. If the time of nanocrystal growth during the nucleation period is short compared to the subsequent growth processes, the nanocrystals can become more uniform over time as size focusing takes place.^[75, 81, 88]

An alternative synthetic approach involves mixing of the reagents in a vessel at a temperature low enough to preclude any appreciable reaction.^[16, 75, 88, 89] A controlled ramp of the solution temperature accelerates the chemical reaction and produces the required supersaturation, which results in a burst of nucleation. As long as the temperature is adjusted to keep the rate at which the reagents react smaller than or equal to the rate at which the material is added to the existing nuclei, the supersaturated state is never revisited and no new nuclei form. In either approach, the size distribution of the nanocrystal sample is limited primarily by the short time interval in which the initial crystallites form and begin to grow.

In general, the nanocrystal size increases with increasing reaction time as more material is added to the nanocrystal surfaces, and also with increasing temperature as the rate of addition of material to the existing nuclei increases.^[16, 75, 81, 88]

Based on the discussion above, some semiconductor nanocrystals have been synthesized recently. The first examples are II-IV semiconductor nanocrystals. In the synthesis of II-VI nanocrystals, group II sources can be metal alkyls, metal oxide, or organic salts. The group VI sources are often organophosphine chalcogenides (R_3PE) or bistrimethylsilylchalcogenides TMS_2E (TMS, trimethylsilyl) (where E is S, Se, and Te). High-boiling coordinating solvents include R_3P , R_3PO , alkyl phosphites, alkyl phosphates, pyridines, alkylamines, and furans. CdO , $CdCO_3$, $Cd(Ac)_2$, Me_2Cd , etc., can be used as Cd sources. By tuning the reaction parameters, different sizes and shapes of $CdSe$,^[55, 75, 80, 81, 88, 90-93] CdS ,^[81, 88, 94] $CdTe$,^[80, 88, 94-96] $ZnSe$ ^[97] and ZnS ^[98] nanocrystals have been successfully prepared. Another example is monodisperse III-V semiconductor nanocrystals. High-quality InP and $InAs$ nanocrystals have been synthesized by rapid mixing and heating of group III and V precursors in high-boiling, coordinating solvents.^[99] Typically, $InCl_3$ is employed as an In source to form InP and $InAs$ with TMS_3P or TMS_3As in R_3P/R_3PO solvents. The resulting nanocrystals can then be dissolved in non-polar solvents. Another example is the preparation of monodisperse IV-VI semiconductor nanocrystals:^[100, 101] $PbSe$ nanoparticles are synthesized by rapidly injecting lead oleate and trioctylphosphine selenide (TOPSe) dissolved in trioctylphosphine into diphenyl ether at 150 °C. The reaction temperature is adjusted in the range of 90-220 °C to obtain different sizes of $PbSe$ nanoparticles.^[102]

2.3.2. Micelles

Reverse micelles are formed in non-aqueous media where the hydrophilic headgroups are directed towards the core of the micelles and the hydrophobic groups are directed outward.^[103] Such reverse micelles can be formed by ionic surfactants with alkyl chains alone, such as diethyl sulfosuccinate (DES), or a mixture of ionic and nonionic surfactants with a short oxyethylene chain dissolved in organic solvents.

Reverse micelles are usually thermodynamically stable mixtures of four components: surfactant, cosurfactant, organic solvent, and water. Some suitable surfactants are sodium dodecyl sulfate (SDS), cetyltrimethylammonium bromide (CTAB), and Triton-X. The droplet size controls the size of the particles and can be

tuned by changing w , where w is the ratio $[\text{H}_2\text{O}]/[\text{surfactant}]$.^[103] The major change in the particle size is obtained at low water content. When the water content increases, the size of the water droplet within the micelle increases, and thus the particle size increases until around $w = 20$, the point when the particle size reaches a plateau. For II-VI semiconductors, such as CdS, ZnS, CdMnS, CdZnS, and CdTe, it is possible to control the particle diameter from 1.8 to 4 nm.^[104]

In case of normal micelles, the hydrophobic hydrocarbon chains of the surfactants are oriented toward the interior of the micelle, and the hydrophilic groups of the surfactants are in contact with the surrounding aqueous medium. For example CdS nanocrystals can be obtained by this way.^[105] The droplet size can increase to a dimension that is much larger than the monolayer thickness of the surfactant because the inside pool of water or oil is enlarged. As the surfactant concentration increases further, micelles can be deformed and can change into different shapes, which makes it possible to synthesize different nanoparticle shapes.^[106] Importantly, the quality of particles prepared by using micelle methods is not better than that of particles prepared in high temperature route as discussed above.

2.3.3 Chemical vapor deposition (CVD)

In CVD, the vaporized precursors are introduced into a CVD reactor and adsorb onto a substance held at an elevated temperature. These adsorbed molecules will either thermally decompose or react with other gases/vapors to form crystals. The CVD process consists of three steps: (a) mass transport of reactants to the growth surface through a boundary layer by diffusion, (b) chemical reactions on the growth surface, and (c) removal of the gas-phase reaction byproducts from the growth surface. Nucleation in the gas phase is homogeneous, whereas nucleation on the substrate is heterogeneous. Catalysts, usually transition metal particles such as Fe, Ni, and Co, are also used in the CVD process. For example, strain-growth is used to produce nanoparticles in the CVD process.^[107-110]

2.4 Growth mechanism of nanostructures of different shapes

2.4.1 Effect of monomer concentration

Nanocrystals of various shapes have been successfully synthesized over the past years. In particular, dot-^[16] rod-^[111-113] spindle-^[111, 112] and tetrapod shaped^[111, 112, 114] semiconductor nanocrystals have been fabricated as shown in figure 2.4.1.

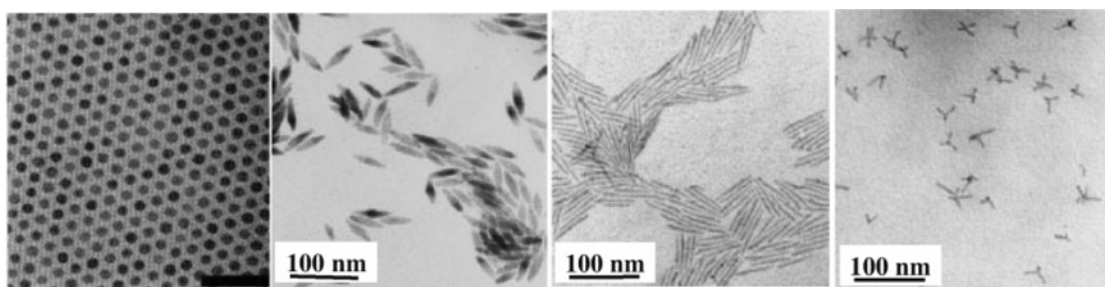


Figure 2.4.1 Different shapes of CdSe nanoparticles (from left to right): dots, spindle-shaped, rod-shaped, and tetrapod-shaped. After reference [55, 111]

Because the properties of nanosized materials are strongly influenced by their shape, it is very important to explore the growth mechanisms that lead to a particular nanocrystal shape to systematically produce the desired material. Peng et al. have investigated the growth mechanisms for developing various shapes of II-VI semiconductors using the hot TOPO/TOP sol-gel process^[111] described above. From the previous sections, we have learned that a given monomer concentration leads to a critical nanoparticle size. Any crystals with smaller sizes will have higher solubility and thus will dissolve in the solution. When the monomer concentration is depleted due to particle growth, the critical size becomes larger than the average size present. Consequently, Ostwald ripening^[86] or defocusing occurs, where the size distribution broadens. Therefore, the nucleation stage plays a key role in determining the size/shape of the resulting nanocrystals

Following consideration by Peng, at low monomer concentrations or long enough growth time, all nanocrystals grow toward the topology with the lowest chemical potential, and this leads to the generation of isotropic dots only. On the other hand, a medium monomer concentration can support anisotropic growth in a three dimensional growth stage and consequently lead to spindle shaped nanocrystals. At high monomer concentration, magic-size nanoclusters (see Figure 2.4.2) (clusters with local minimum chemical potential because of their closed-shell configurations) promote the formation of rods or other metastable elongated structures. If the remaining monomer concentration in the sample solution is still extremely high, the solution could supply a sufficient amount of monomers for each seed to fully grow arms on the four (111) facets of a zinc blende structure of tetrahedral seeds, and leading to tetrapod-shaped nanoparticles as shown in figure 2.4.2

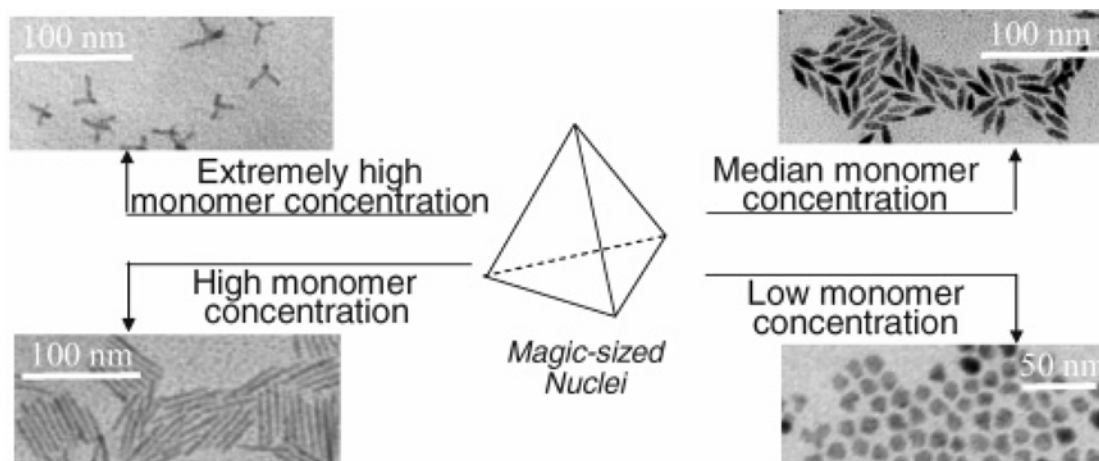


Figure 2.4.2 Illustration of the growth conditions for different CdSe nanocrystal shapes. The figure is adopted from reference [111]

In reality, the monomer concentration remaining in the reaction solution is always depleted by the nucleation and growth of the nanocrystals. If the reaction time is sufficiently long, the monomer concentration should drop to a level lower than that required for a given shape, and the nanocrystals should eventually evolve to the most stable spherical shape if no additional monomers are added to the reaction system.

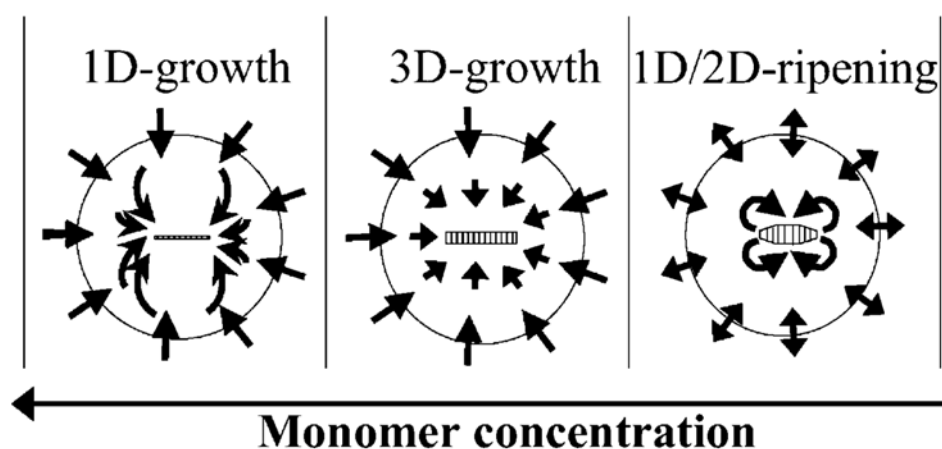


Figure 2.4.3 Illustration of the three growth stages of elongated CdSe nanocrystals at different monomer concentrations. The figure is adopted from references [111, 112]

Figure 2.4.3 illustrates the three stages for the shape evolution of a rod-shaped nanocrystal as the monomer concentration decreases. The third stage is one-dimensional-to-two-dimensional intraparticle ripening. During this stage, there is no net monomer exchange between the nanocrystals and the solution, and the number of nanocrystals remains constant. Due to the differences in chemical potential between

different facets of the nanocrystals, the monomers on the nanocrystals move in an intraparticle manner to convert rod-shaped nanocrystals to spherical shaped ones.^[111, 112]

2.4.2 Vapor-liquid-solid and solution-liquid-solid mechanism

Figure 2.4.4 illustrates the growth process of nanowires in many CVD processes, where catalysts are usually employed.^[51] The growth of nanocrystals follows the vapor-liquid-solid growth mechanism, in which the vapor phase condenses on the catalyst and forms a co-alloy in liquid phase, and the target solid wire grows after nucleation from this liquid phase resulting from the continuing condensation of the vapor phase. Usually, the catalyst defines the diameter of the structure and localizes the reactant at the end of the growing nanowire. The liquid catalyst alloy cluster serves as a preferential site for absorption of reactant (i.e., there is a much higher sticking probability on liquid vs solid surfaces) and, when supersaturated, acts as the nucleation site for crystallization. Preferential one-dimensional growth occurs in the presence of the reactant as long as the catalyst remains as a liquid. The specific composition (catalyst, nanowire material) to form a liquid alloy with the nanowire material of interest and the synthesis temperature are key parameters for the well-controlled growth of nanocrystals.

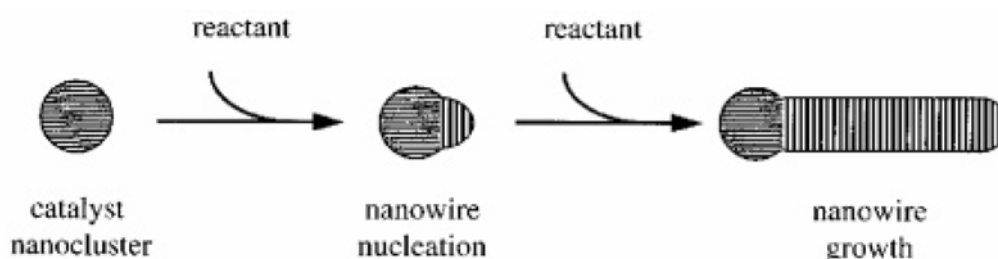


Figure 2.4.4 Schematic diagram illustrating the catalyst supported synthesis of nanowires. Reactant material, which is preferentially absorbed on the catalyst cluster, is added to the growing nanowire at the catalyst-nanowire interface. Figure is adopted from reference^[51]

In an extension of the synthesis of nanowires, effort has also been directed toward alternative solution based approaches such as solution-liquid-solid. These schemes ultimately rely on a metal catalyst particle for promoting nanowire growth as in the case of CdSe nanowires, which are prepared using Au/Bi catalysts at high temperature ($>300\text{ }^{\circ}\text{C}$).^[115] More recently, the controlled growth of anisotropic CdSe

structures including dots, rods and multi-rods has been reported by using noble metal nanoparticles (Au, Ag, Pd, and Pt) as seed at lower temperature. [56]

2.5 Chemical surface modification of nanocrystals

2.5.1 Inorganic surface passivation

The surface plays an important role for the properties of nanoparticles, including solubility, reactivity, stability, melting point, and electronic structure.^[8] At the same time, the surface is the region where the nanoparticles come into contact with other materials and therefore plays a vital role in the construction of superlattices in the fabrication of new devices and in the conjugation with target molecules. Thus, the chemical modification of the surface of nanoparticles is a very important field.

During growth of the nanoparticles, organic stabilizing agents are present to prevent nanoparticle aggregation and precipitation. In addition various inorganic materials have been utilized as capping materials on the surface of nanoparticles through covalent or ionic interactions. [16, 116] These capping groups can stabilize nanocrystals in solution and passivate surface electronic states in semiconductor nanocrystals. For example, CdSe nanocrystals have been capped with ZnS, [28, 32] CdS [29] or ZnSe [33] to improve not only the photoluminescence quantum yield but also the stability of nanocrystals to develop a reliable processing chemistry. However, for different shell materials combined with e.g. CdSe cores, type-I and type II core/shell structures are possible.

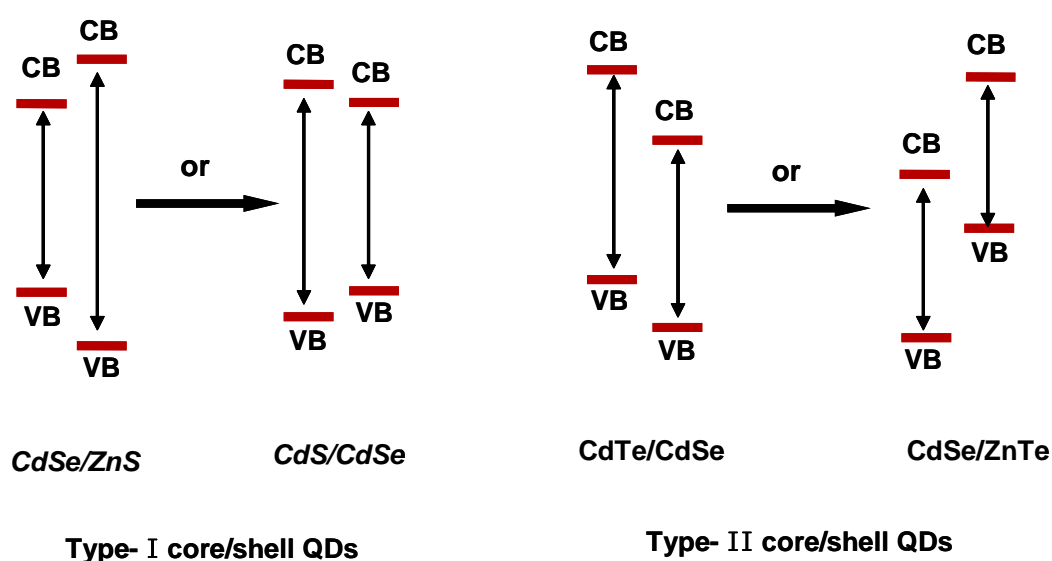


Figure 2.5.1 Various examples for type-I and type-II core/shell structures

A) Type-I core/shell structures: The band offsets are such that the conduction band (CB) of the shell is of higher energy (or lower energy) than that of the core, and the valence band (VB) of the shell is of lower energy (or higher energy) than that of the core. Both electron and hole are confined together either in the core or shell. The emission of type-I nanocrystals depends either on the size of the core or the shell. Such core/shell nanocrystals have been shown to be generally more robust against chemical degradation or photo-oxidation. Depending on the energetic band positions and lattice mismatches of semiconductor shell materials in combination with a CdSe core, the properties of core/shell nanocrystals passivated using different materials are also different, although the passivating shell generally protects the core and reduces surface degradation. On the basis of results reported in literature,^[29, 32] an ideal, high quality multi-shell core/shell nanocrystal with CdSe core was synthesized by combination of different shell materials during this thesis. This result will be discussed in detail in chapter 4. On the other hand, also reverse type-I core/shell structure can be fabricated. An example is CdS/CdSe core/shell nanocrystals where emission comes from the shell material as described in chapter 6. In this case, the optical properties of the core/shell structure can be tuned by changing the thickness of the shell.

B) Type-II core/shell structures: A type II nanoparticle is defined as following: Both the valence and conduction bands of the core are lower (or higher) than those of in the shell. As a result, one charge carrier is mostly confined to the core, while the other is mostly confined to the shell. This core/shell structure results in some new optical properties which can not be obtained from type-I structures. For instance, due to the slow electron-hole recombination extraordinarily long radiative lifetimes have been found. On the other hand, type-II structures give access to wavelengths that would otherwise not be available with a single material (core and shell materials). The emission of type-II core/shell nanocrystals mainly originates from the radiative recombination of electron-hole pairs across the core-shell interface. Therefore, the photoluminescence of type-II core/shell can be tuned by increasing the thickness of the shell materials and by variation of the size ratio of core and shell. For example, near infrared emission has been obtained in case of CdTe/CdSe or CdSe/ZnTe core/shell nanocrystals.^[36] In this thesis, a new type-II core/shell system with ZnTe cores is described in detail in chapter 5.

2.5.2 Surface modification by functionalized molecules

Besides modifying the properties of the bare nanoparticles, organic molecules also play a role as the connecting media of the nanoparticles to the outside world. For example, in the superlattices of nanoparticles, they define the space distances between nanoparticles.^[16, 117] On the other hand, in nanoparticle based drug delivery, they connect the nanoparticles to the therapeutic agents.^[118]

Considering potential applications based on the optical properties of nanocrystals, a very important field is fluorescent labeling in biology.^[19, 21, 63] High quality nanocrystals with hydrophobic ligands are well established in organic solvents by now. At present, besides development of synthesis techniques to prepare new nanocrystals, much work is devoted to surface modification of nanocrystals to render them to become water soluble for bio-applications.^[19, 21, 63, 119-122]

Nanocrystals prepared using high-temperature routes in organic solvent have no intrinsic aqueous solubility. Thus, phase transfer to aqueous solution requires surface functionalization with hydrophilic ligands which mediate both the colloid's solubility and serve as a point of chemical attachment for biomolecules (see Reference [123]). A representative list of such ligands and the corresponding hydrophilic nanocrystals is provided in table 2.1. These strategies can be grouped into three major routes. The first uses 'cap exchange' and involves the substitution of the native ligands (TOP/TOPO) with bi-functional ligands, each presenting a surface anchoring moiety to bind to the inorganic nanocrystal surface (for example, thiol), and an opposing hydrophilic end group (for example, hydroxyl, carboxyl) to achieve water-compatibility.^[19, 21] The second strategy involves formation of polymerized silica shells functionalized with polar groups, which insulate the hydrophilic nanocrystal (Table 2.1c).^[124] The third method preserves the native ligands (TOP/TOPO) on the nanocrystals and uses variants of amphiphilic copolymers and phospholipids to tightly interleave the alkylphosphine ligands through hydrophobic attraction, whereas the hydrophilic outer block permits aqueous dispersion and further derivatization (see table 2.1 d, f and g).

In fact, the advantages of each strategy have to be carefully weighted against the drawbacks. For example, compact mono-mercapto ligands (Table 2.1a) have short shelf lives (<1 week) due to dynamic thiol interactions.^[125] On the contrary, dithiol dihydrolipoic acid ligands improve long-term stability from ~1 week to 1–2 years, suggesting that polydentate thiolated ligands could be even more effective.^[120, 125, 126]

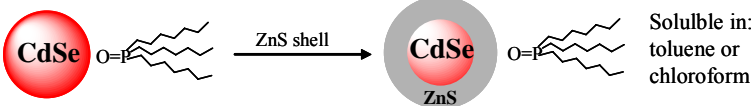
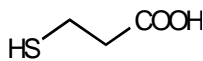
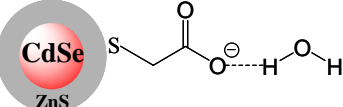
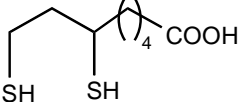
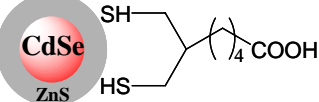
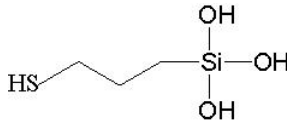
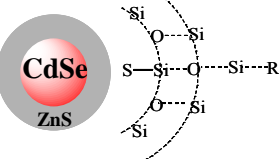
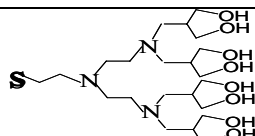
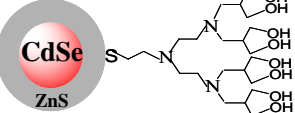
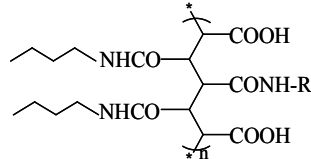
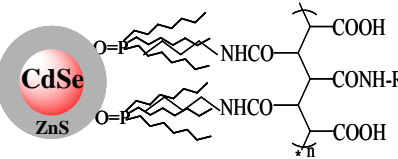
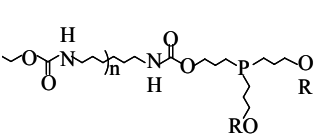
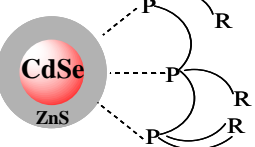
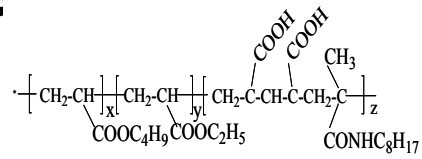
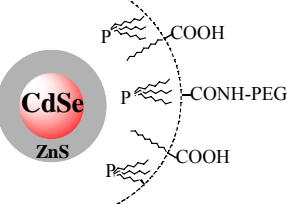
		
Representative surface ligands	Nanocrystal-ligand complex	Example
A 		Mercaptopropionic acid
B 		Dihydrolipoic acid derivatives
C 		Mercaptopropyl silanols
D 		Dendrimer box
E 		Modified acrylic acid polymer
F 		Oligomeric phosphine
G 		Amphiphilic triblock copolymer

Table 2.1 Schematic of generic nanocrystal stabilized in water. Examples (A-G) are surface-capping strategies with the nanocrystal and the aqueous environment. After reference:[19, 21, 39, 57, 59, 119-122, 124, 126-129]

However, carboxylic acids and almost all carboxyterminated ligands limit dispersion to basic pH. [125] Silica shells and polymer/phospholipids encapsulation provides stability over a broader pH range, but result in substantially larger hydrophilic nanocrystals. For example, phospholipids and block copolymer coatings tend to

increase the diameter of CdSe–ZnS nanocrystals from ~4–8 nm before encapsulation to ~20–30 nm, a size that although smaller than most mammalian cells can still limit intracellular mobility and may preclude fluorescence resonance energy transfer (FRET)-based investigations.^[125] A preliminary semiconductor example of new ligands, leading to water soluble, pH sensitive multi-shell nanocrystals with high quantum yield is described in chapter 7.

2.6 Applications

Compared with bulk materials, low-dimensional nanoscale materials with their large surface areas and possible quantum confinement effects exhibit distinct electronic, optical and chemical properties. Here several potential applications for CdSe nanocrystals are briefly discussed in the following:

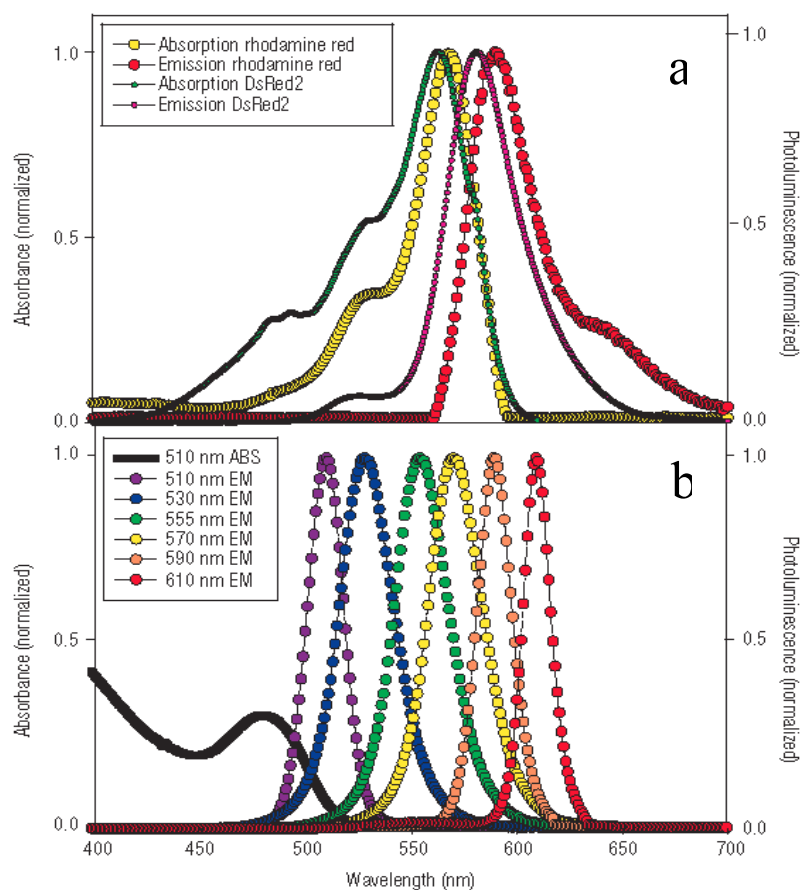


Figure 2.6.1 Comparison of rhodamine red/DsRed2 spectral properties to CdSe nanocrystals highlighting how multiple narrow, symmetric nanocrystal emissions can be used in the same spectral window as that of an organic dye. (a) Absorption (Abs) and emission (Em) of rhodamine red DsRed2. Reference [130] (b) Abs and Em of six different nanocrystals.. The black line shows the absorption of the 510-nm emitting nanocrystals. Reference [131, 132]

One important direction is that fluorescent semiconductor nanocrystals have the potential to revolutionize biological imaging.^[58, 123] Traditional dye molecules used as biolabels have some drawback.^[58] For example, the intrinsic photophysical properties of organic and genetically encoded fluorophores, which generally have broad absorption/emission profiles (Figure 2.6.1a) and low photobleaching thresholds, have limited their effectiveness in long-term imaging. The seminal publications describing the first biological uses of nanocrystal-fluorophores foresaw that their unique properties could overcome these issues.^[19, 21] Nanocrystal properties of interest to biologists include high quantum yield, high molar extinction coefficients^[32, 83], broad absorption with narrow, symmetric photoluminescence (PL) spectra (full-width at half-maximum ~25–40 nm) (Fig. 2.6.1 b), large effective Stokes shifts (Fig. 2.6.1 b), high resistance to photobleaching and exceptional resistance to photo- and chemical degradation.^[125, 133-135]

In recent publications, it was shown that photovoltaic cell devices and light-emitting diodes (LEDs) can be fabricated by using CdSe nanocrystals. In case of the photovoltaic cells, Alivisatos and co-workers demonstrated how semiconductor nanorods could be used to enhance the processibility and efficiency.^[40, 41] They fabricated thin-film photovoltaic devices by blending CdSe nanorods with polythiophenes to obtain hybrid materials. The intrinsic features and thus performance of such a device could be tuned by controlling the aspect ratio of the nanorods. They also found that nanorods were superior to spherical dots in photovoltaic applications, because they could provide a direct path for electrical transport at much lower loading.

More recently, a photovoltaic device was prepared by using rod shaped CdSe and CdTe nanocrystals, which form a kind of type-II heterostructures as reported by Alivisatos and co-workers.^[136] The heterostructure results in efficient charge transfer and separation between the two inorganic nanorod components with staggered energy levels. These devices were stable in air, and post-fabrication processing, for example sintering CdTe/CdSe bilayer cells, gave a power conversion efficiency of 3%.

Other potential applications have been suggested as follows: Devices fabricated from single nanocrystals have been proposed, such as a single-electron transistor based on CdSe nanocrystals.^[137, 138] A design for a solid-state laser, based on the luminescence properties of CdSe quantum dots,^[139] in a host material such as poly (methyl methacrylate) has been described, where the wavelength of the emitted

light is determined by the size of the nanocrystallites chosen. In addition, semiconductor nanocrystals show great promise for use in light-emitting diodes (LEDs), which have been widely studied for display applications by some groups. [25, 140, 141]

In conclusion, there are almost unlimited research opportunities being explored by many laboratories around the world in the area of semiconductor nanomaterials. The scientific and technical potential of these nanostructures is promising, and the future of this field of nanoscience is certainly bright.

3. Experimental

3.1 Approaches for nanocrystal synthesis

For synthesizing CdSe nanocrystals, a revolutionary technique was invented by the group of Bawendi.^[75] However, the preparation steps require inert atmosphere, and the method was performed inside a commercial glove box containing less than 1 % of O₂ and H₂O, under slight overpressure of nitrogen at 3 – 4 mbar. Simpler methods for the synthesis of CdSe nanocrystals can be performed in a setup as shown in figure 3.1, showing an air-free system for preparation of correlative chemical materials. Experiments were done under vacuum at about 1-4 mbar. The temperature was controlled at a heating rate of 10-15 °C/min in the temperature interval 20 – 800 °C under a continuous argon flow of 20-30 ml/min.

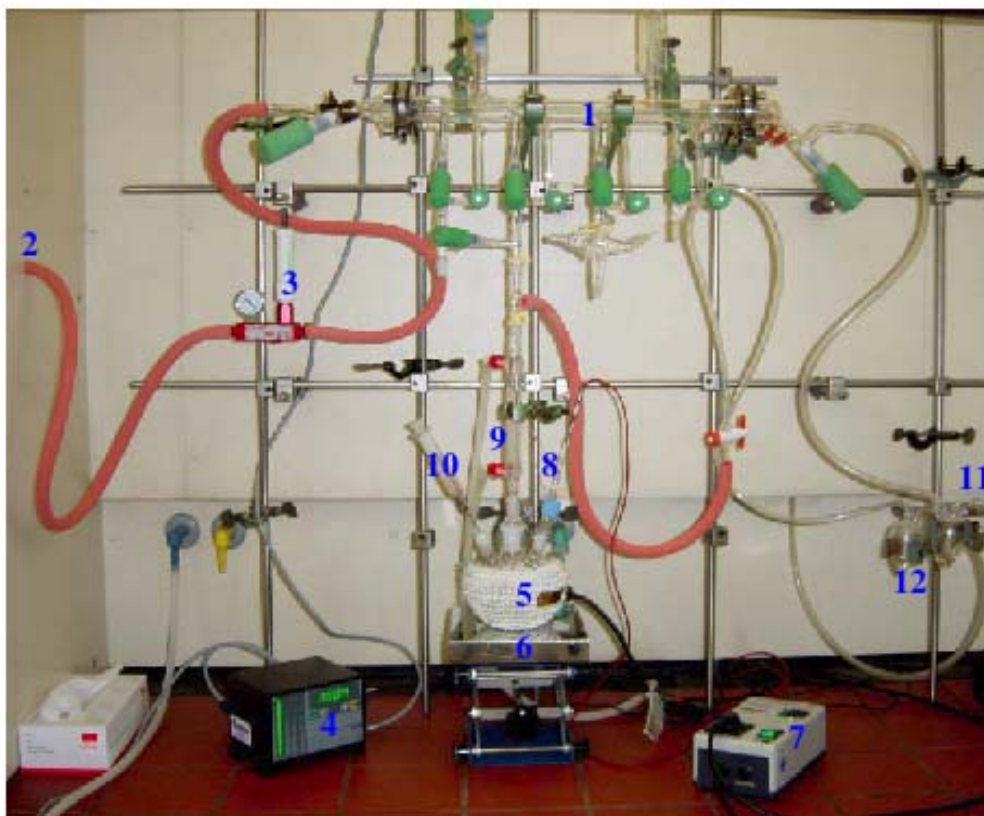
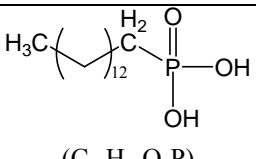
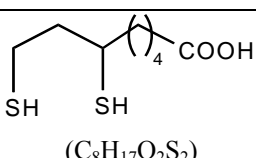
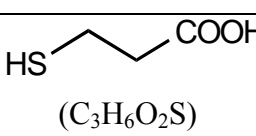


Figure 3.1 Experimental setup for synthesis of nanocrystals. 1. Schlenk glass ware; 2. To vacuum pump; 3. Pressure regulator; 4. Pressure controller; 5. Electrical heating bath; 6. Magnetic stirrer; 7. Temperature regulator; 8. Temperature controller stick; 9. Reverse water cooler stick; 10 Syringe; 11. To argon cylinder; 12. Gas counters.

3.2 Chemicals

Compound (grad)	Chemical Structure	Boiling Point	Density g/ml	Molecular Weight	Supplier
Trioctylphosphine-oxide (TOPO) (99%)	$[\text{CH}_3(\text{CH}_2)_7]_3\text{PO}$ ($\text{C}_{24}\text{H}_{51}\text{OP}$)	~360 °C		386.65	Aldrich
Trioctylphosphine (TOP) (90%)	$[\text{CH}_3(\text{CH}_2)_7]_3\text{P}$ ($\text{C}_{24}\text{H}_{51}\text{P}$)	290~291 °C/ 50 mm Hg	0.831	370.64	Aldrich
Oleic acid (OA) (90%)	$\text{CH}_3(\text{CH}_2)_7\text{CH}=\text{CH}-$ $-(\text{CH}_2)_7\text{COOH}$ ($\text{C}_{18}\text{H}_{34}\text{O}_2$)	~195 °C/ 1.2 mm Hg	0.89	282.46	Aldrich
Octadecene (ODE) (90%)	$\text{CH}_3(\text{CH}_2)_{15}\text{CH}=\text{CH}_2$ ($\text{C}_{18}\text{H}_{36}$)	320~325 °C	0.789	252.48	Aldrich
Octadecylamine (ODA) (97%)	$\text{CH}_3(\text{CH}_2)_{17}\text{NH}_2$ $\text{C}_{18}\text{H}_{39}\text{N}$	232 °C/ 32 mm Hg		269.51	Aldrich
Oleylamine (OAm) (90%)	$\text{CH}_3(\text{CH}_2)_7\text{CH}=\text{CH}-$ $-(\text{CH}_2)_7\text{CH}_2\text{NH}_2$ ($\text{C}_{18}\text{H}_{37}\text{N}$)	348~350 °C	0.813	267.5	Aldrich
Tetradecyl-phosphonic acid (TDPA)	 ($\text{C}_{14}\text{H}_{31}\text{O}_2\text{P}$)	120~130 °C/ 0.2 mm Hg		278.4	Lab
Lipoic acid,	 ($\text{C}_8\text{H}_{17}\text{O}_2\text{S}_2$)	169~172 °C/ 1 mm Hg		208.4	Lab
Diethylzinc (98%)	$(\text{CH}_3\text{CH}_2)_2\text{Zn}$ $\text{C}_4\text{H}_{10}\text{Zn}$	98 °C	0.74	123.51	Strem Chemicals
Hexamethyl-disilathiane (90%)	$(\text{CH}_3)_3\text{Si-S-Si}(\text{CH}_3)_3$ ($\text{C}_6\text{H}_{18}\text{Si}_2\text{S}$)	164 °C	0.846	178.4	Aldrich
<i>N</i> -Ethyl- <i>N'</i> -(3-dimethylaminopropyl)carbodiimide (EDC)(98%)	$(\text{CH}_3)_2\text{N}-(\text{CH}_2)_3-$ $-\text{N}=\text{C}=\text{N}-\text{C}_2\text{H}_5$ ($\text{C}_8\text{H}_{17}\text{N}_3$)			191.71	Aldrich
Mercaptopropionic acid (MPA)(99%)	 ($\text{C}_3\text{H}_6\text{O}_2\text{S}$)	110~111	1.12	106.4	Aldrich
Tetracosan (99%)	$\text{CH}_3(\text{CH}_2)_{22}\text{CH}_3$ ($\text{C}_{24}\text{H}_{50}$)	~360 °C		338.65	Aldrich
CdO (99.99%)			8.18	128.4	Aldrich

ZnO (99%)			5.61	81.37	Aldrich
S (99.98%)			2.36	32	Aldrich
Se (99.5%)			4.81	78.96	Alfa
Te (99.5%)			6.24	127.6	Alfa

3.3 Synthesis methods

3.3.1 CdSe nanocrystals

As discussed above, a wide range of chemical methods has been reported for the preparation of semiconductor nanocrystals. In case of the synthesis of CdSe nanocrystals, we employed a sol process which is called molecular precursor route. In the following, several synthetic methods for the preparation of CdSe nanocrystals using molecular precursor methods are introduced.

In general, the synthetic approach by molecular precursors involves thermal treatment of a reacting solution containing molecular precursors of Cd and Se, leading to a burst of nuclei and a further growth up to the desired size and shape. The organometallic precursor route was developed by Murray et al. in 1993,^[75] which involved the reaction of the cadmium organometallic precursor dimethyl cadmium with a Se precursor in a hot coordinating solvent (thioctylphosphine oxide, 360°C). Nowadays, it is generally acknowledged that the reactant dimethyl cadmium is an expensive, pyrophoric, and hazardous material. In 2001, Peng et al.^[88] developed a much simpler and “greener” non-organometallic precursor route using inexpensive and less toxic CdO instead of Cd(CH₃)₂ to produce CdSe nanocrystals. Recently, approaches using non-coordinating solvents such as octadecene (ODE) instead of coordinating solvents such as TOPO have been extensively studied.^[94, 142] As a combination of the advantages of two synthetic routes, we adopted the synthesis of CdSe nanocrystals (including various CdSe architectures) from CdO precursors and a cheap non-coordinating solvent (ODE). A typical synthetic route will be described in chapter 4.

3.3.2 Shell growth on CdSe core nanocrystals

Traditionally fabricated CdSe core/shell structures^[32] containing a ZnS or CdS shell grown by the use of active precursors, such as diethyl zinc, trimethylsilane sulfide and dimethyl cadmium, have not yet reached the same quality like the growth

of plain core nanocrystals in terms of size and size distribution control. In principle, the reactivity of the precursors should be weak enough to prevent independent nucleation, but sufficiently strong to promote the epitaxial growth around the existing CdSe core nanocrystals. Therefore, relatively stable, inexpensive, and safe alternative precursors should be more suited for the growth of high-quality core/shell nanocrystals than the traditional organometallic precursors.^[29, 32] To further control the thickness of the shells, a new successive ion layer adsorption and reaction method (SILAR)^[143] can be used for the growth of core/shell semiconductor nanocrystals with precise thickness control. The key feature of the SILAR method is that the precursors of the anionic and cationic components of the shell compound semiconductor are introduced in an alternating fashion. Importantly, only two subsequent additions are required for the growth of one layer of the shell semiconductor.

3.4 Spectroscopic techniques

3.4.1. Absorption

UV visible absorption spectra were taken with the spectrometer OMEGA 20 from Bruins Instruments. Cuvettes with two or four quartz windows and a thickness of one centimeter were used. Spectra of the solutions were taken against the respective pure solvent reference. The OMEGA software package allowed the calculation of absorption coefficients of the dissolved compounds. The recorded spectra were usually shown as optical density versus wavelength and were transferred into ASCII files and further processed with the ORIGIN software package.

3.4.2. Fluorescence

Photoluminescence and fluorescence excitation spectra were measured with a FluoroMax-2 spectrofluorimeter from ISA JOBIN YVON-SPEX Instruments S. A., Inc. 1 cm thick cuvettes with four quartz windows were used as sample cells. The optical density of the solutions was preliminary checked by the absorption spectra and kept below OD~0.1 for reliable fluorescence measurements.

The fluorescence quantum yield of nanocrystals was determined as following: A solution of the standard dye (Rhodamine B or perylene imide) was excited at a wavelength where the optical density of the solution was equivalent to that of the nanocrystals. The integrals over the obtained fluorescence spectra were compared,

assuming that the fluorescence quantum yield of the dye solutions was 100 %. The optical intensity of both solutions at the first absorption peak was < 0.1 . The spectra were usually displayed as fluorescence intensity vs. wavelength and were transferred into ASCII files and further processed with the ORIGIN software.

3.4.3 Nuclear magnetic resonance (NMR) spectra

^1H NMR spectra were recorded on a Bruker DRX400 Avance Instrument (400 MHz). Chemical shifts were calibrated to the residual signal of a deuterated solvent.

3.5 Techniques for structural characterization

3.5.1 Transmission electron microscopy (TEM)

The low-resolution images were taken on a Philips EM-420 transmission electron microscope with an acceleration voltage of 120 kV. The nanocrystal samples were purified by acetone precipitation from chloroform or toluene solution or by hexane/methanol extraction. Samples for TEM were prepared by depositing a drop of a nanocrystal toluene solution onto a copper grid supporting a 5 nm thin film of amorphous carbon. The excess liquid was removed with filter paper, and the grid was dried in air. Randomly oriented nanocrystals on the TEM substrate were obtained by using a diluted nanocrystal solution with an absorbance at the first absorption peak of the nanocrystals below about 0.05. If the absorbance was above 0.2, densely packed monolayers and multilayers of nanocrystals were observed.

High-resolution TEM pictures were taken using a Tecnai F30ST with a field emission gun operated at 300kV.

3.5.2 Powder X-ray diffraction (XRD)

Powder Wide-angle X-ray diffraction (WAXS) was performed with a Siemens θ -- θ diffractometer (D500T) in reflection geometry using Cu-K α radiation from a Siemens generator (Kristalloflex 710 H) operating at 35 kV and 30 mA, and a graphite monochromator. Measurements were performed in a 2θ (θ : diffraction angle) range from 18 to 70 degrees. Approximately 10 mg of nanocrystals were dispersed in a minimum volume of toluene (0.2 ml). The nanocrystal solution was deposited onto low-scattering quartz plates, and the solvent was evaporated under mild vacuum.

3.5.3 Energy-dispersive X-ray spectroscopy (EDX):

For elemental analysis a Tecnai F30ST (FEI) with a field emission gun operating at 300kV, equipped with an EDX spectrometer with a Si/Li detector and an ultra thin window, was used. The analysis was performed in scanning mode with a beam diameter of ~1nm at room temperature.

3.5.4. Dynamic light scattering (DLS)

Hydrodynamic radii (R_h) of the nanocrystals have been determined by dynamic light scattering (DLS) using an experimental setup consisting of a He-Ne laser (JDS Uniphase 1145p-3083, JDS Uniphase, 632.8 nm, 25 mW output power), goniometer SP-86(ALV), and an ALV-3000 digital correlator/structurator. The particle size polydispersity has been estimated from exponential decay fits of the time-intensity-correlation functions (in case of water-soluble particles), and from the 2nd cumulant in case of the much smaller (on average) hydrophobic precursor nanocrystals. All light scattering measurements have been carried out with filtered samples (Millipore LG filters of pore size 0.2 μm).

4. Synthesis and characterization of type-I multi-shell nanocrystals

4.1 Introduction

CdSe nanocrystals are considered as promising candidates for various applications because their emission color can be precisely adjusted from blue to red. Besides the development of synthesis techniques to prepare high quality CdSe samples, [75, 88] much experimental work is devoted to molecular surface modification to improve the luminescence efficiency [144, 145] and colloidal stability of the particles or to develop a reliable processing chemistry. [13, 146] To solve these problems, several methods of inorganic surface modification have been developed to completely passivate the CdSe nanocrystals, in which growing a thin shell of a wide band gap semiconductor (ZnS or CdS) [28, 29] on the outside of the nanocrystals results in a type-I core/shell structure where the band gap of the core lies energetically within the band gap of the shell material and the photo generated electrons and holes are mainly confined inside the CdSe core. Such core-shell particles not only exhibit efficient luminescence with stability superior to single phase particles, but also have been shown to be more robust against chemical degradation or photo-oxidation. [29]

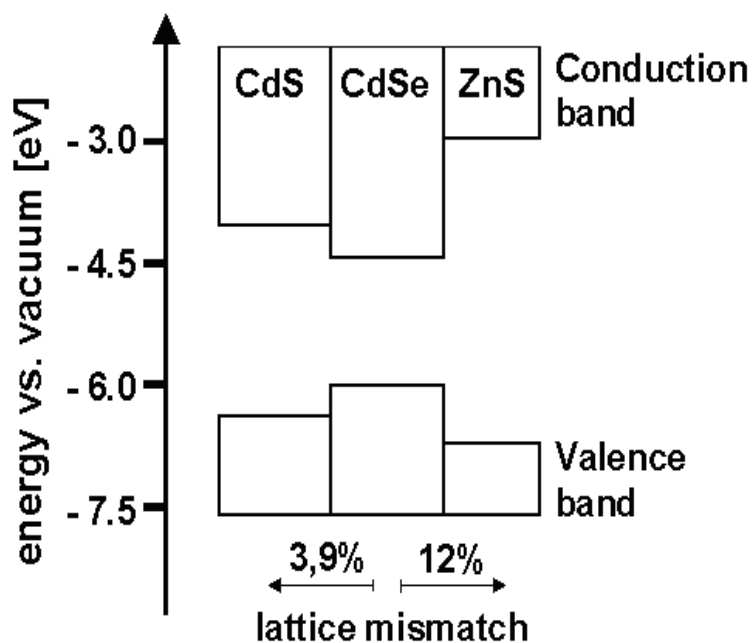


Figure 4.1 Energetic band positions and lattice mismatch of bulk semiconductor material combinations used in this chapter. Lattice mismatch was calculated using this formula: $\text{lattice mismatch} = (c_{\text{core}} - c_{\text{shell}}) / c_{\text{core}}$; Here c is the bulk lattice parameter of a wurzite structure compound. $C_{\text{CdSe}} = 7.10 \text{ \AA}$, $C_{\text{CdS}} = 6.75 \text{ \AA}$ and $C_{\text{ZnS}} = 6.25 \text{ \AA}$.

Basically, there are different requirements for “ideal” core/shell nanocrystals both from a crystallographic and electronic point of view. Two main factors have to be considered while choosing the semiconductor material for the passivating shell. First, in order to produce particles with high crystallinity, the core and shell materials should have similar lattice parameters such that the shell-growth happens in an epitaxial manner without the formation of structural defects. The second factor is the band offset between the core and the shell regions that should be sufficiently high so that carriers are confined into the core region and kept separated from the surface, where defects can lead to undesired nonradiative relaxation processes.

A typical traditional core/shell nanocrystal^[32] with CdSe core is CdSe/ZnS, where the ZnS shells provide a good passivation of the cores. However, the large mismatch (ca. 12% see Figure 4.1) between CdSe and ZnS lattice parameters induces strain at the interface between the core and the shell. It has been shown that if the thickness of the ZnS shell exceeds 2 monolayers, the interfacial strain leads to formation of misfit dislocations relaxing the nanocrystal structure.^[32] These defects in the ZnS shell negatively affect both the PL efficiency and stability of CdSe/ZnS nanocrystals with thick shells. Another effect of the lattice mismatch is the formation of particles with irregular shape and a broad size distribution upon increasing ZnS-shell thickness.^[28]

Another sample is the CdSe/CdS core/shell structure, where the lattice mismatch between the core and the shell materials is relatively small (ca. 3.9% see Figure 4.1). Epitaxial growth of the CdS shell has been reported in some papers.^[29, 146, 147] In addition, this core/shell structure exhibits very high quantum yields. However, the band gap of CdS is not large enough to provide the potential barrier necessary to block both electrons and holes inside the CdSe core. Moreover, the CdS shell can be excited by UV light broadly used in biological applications. This direct excitation of the nanocrystal shell causes its fast photooxidation that makes CdSe/CdS nanocrystals less suitable for a number of applications.

To combine the advantages of both shell materials (CdS and ZnS), a general way of improving photoluminescence yield, stability and robustness of luminescent nanocrystals is systematically studied in our work, where the composition of the shell is gradually changed from CdS to ZnS in radial direction with atomic precision. Our approach is based on engineering both band gap energy and lattice spacing inside a heterogeneous nanocrystal. We have used the “Successive Ion Layer Adsorption and

Reaction” (SILAR) method^[143] to prepare a new kind of CdSe-NC with a sandwich shell-structure consisting of a CdSe core surrounded by 2 monolayers (MLs) CdS, followed by 2~4 MLs $Zn_{0.5}Cd_{0.5}S$ and finally 2 MLs ZnS as the outermost shell. Such a multi-shell structure allows a stepwise change of the lattice spacing from the emitting CdSe core to the protecting ZnS shell and therefore should lead to a considerable reduction of the strain inside nanocrystals. For comparison, we also synthesized different core/shell particles with the same overall shell thickness of CdS, ZnS or $Zn_xCd_{1-x}S$ using the SILAR method. The various nanocrystals will be compared in respect to their crystallinity, size distribution, fluorescence quantum yield and chemical stability.

4.2 Results and discussion

4.2.1 Reaction conditions for shell growth of different compounds by SILAR.

In order to conduct a comparative study of different shell materials, in our work the SILAR method^[143, 147] was used to synthesize core/shell CdSe/CdS/ $Zn_{0.5}Cd_{0.5}S$ /ZnS nanocrystals and several other core/shell systems, including CdSe/CdS, CdSe/ $Zn_{0.5}Cd_{0.5}S$ and CdSe/ZnS. All these samples were prepared from the same CdSe-cores with a similar overall shell thickness under different experimental conditions by using green precursors such as ZnO, CdO and elementary sulfur. Based on these experiments, it was found that the reaction temperature played a critical role for the growth of different shell materials through SILAR in the solvent ODE. Evidently, the accumulated thickness of the shell after each injection decreased systematically as the reaction temperature decreased. This means that the precursors added into the solution through injection did not grow on the surface of the existing nanocrystals at lower temperatures (<200°C). However, at high temperature (>260°C) the reaction of the shell material might lead to the nucleation and subsequent formation of particles rather than to epitaxial growth of the shell. In addition, high temperature made it difficult to prevent Ostwald ripening of the core and core/shell nanocrystals. On the other hand, the SILAR approach is crucial for the growth of our core/shell nanocrystals, since in this way one can precisely control the amount of the precursors to grow a consecutive shell through theoretical

calculations. It will be shown further below (figure 4.3) that the theoretically expected diameter of the particles after the growth of the shells is comparable to the experimental results determined by TEM. In case of the synthesis of CdSe/CdS core/shell particles, it has been demonstrated by the group of Peng that the CdS shell was growing almost exclusively onto the surface of the CdSe nanocrystals at an optimum temperature of 240 °C using CdO and sulfur precursors in an ODE/ODA solvent mixture.^[143] These core/shell particles could be controlled well in diameter with narrow size distribution and they have a high photoluminescence quantum yield of more than 40%.

The growth of ZnS shells around the CdSe nanocrystals by SILAR, using ZnO and S precursors, was studied under different reaction temperatures (from 200 °C to 260 °C). We found that the reaction temperature is crucial for the shell growth: at lower temperature, the ZnS material did not grow completely onto the CdSe-cores, because no red-shift of UV-Vis- and PL-peak but a strong additional absorption in the UV-range was observed. This conclusion has also been verified by the finding that the diameter of the particles did not change according to TEM measurements. At high temperature, we found that the diameter of the core starts to grow further due to Ostwald ripening. In addition, small particles formed in conclusion from the precursors can be also observed in the TEM pictures. All experimental results indicated that the maximum quantum yield of about 50% could be achieved when the reaction temperature was set at 245°C for the growth of the ZnS shell onto CdSe cores.

Based on these results, the growth of ZnS, CdS and ZnCdS shells onto the CdSe cores using CdO, ZnO and S precursors was performed at a reaction temperature of 245 °C by the SILAR method. The different core/shell particles with the same CdSe core were prepared under identical experimental conditions independent of the particular shell material.

4.2.2 Structural characterization

Several techniques were used to monitor the growth of the shells and characterize the structure, crystallinity, and composition of the prepared particles. The wide-field TEM-images (Figure 4.2 A-E) illustrate the size and morphology of the

CdSe core nanocrystals and the corresponding representative core/shell nanocrystals with different shell thicknesses. The core/shell nanocrystals formed long ranged, well-ordered two-dimensional super-lattices, which indicates that the size and shape of the particles are quite mono-disperse. In our experiments, we found that the images of the core-CdSe nanocrystals show a slightly different shape before (A) and after heating to 240 °C for 5 ~ 10 min.(B). It should be noted that CdSe nanocrystals were synthesized using TOPO as a solvent in presence of TDPA, and therefore the nanocrystals obtained were slightly elongated. Therefore, an additional annealing process was necessary to get more spherical CdSe particles for the growth of isotropic core/shell structures as shown in Figure 4.2 (B). For dot shaped CdSe cores, the growth process was performed as described in the experimental section. Figure 4.2 (C) shows particles after growth of 2 ML CdS, image (D) displays the core/shell sample with 5.5 MLs (2 ML CdS and 3.5 ML $Zn_{0.5}Cd_{0.5}S$, and finally (E) and (F) show the core/shell sample with a coverage of 7.5 MLs (2 ML CdS, 3.5 ML $Zn_{0.5}Cd_{0.5}S$ and 2 ML ZnS).

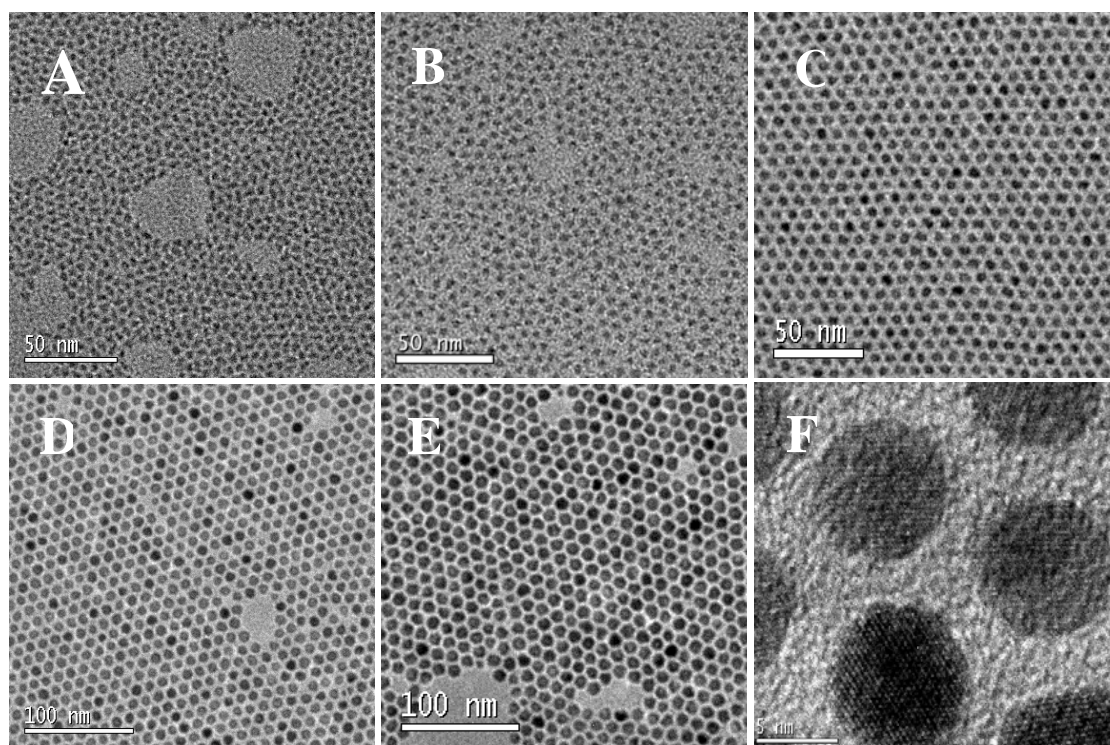


Figure 4.2 TEM images of the plain CdSe-cores and core/shell nanocrystals obtained under typical reaction conditions: (A) TEM images of CdSe-cores, whose shape is slightly elongated with aspect ratio of 1.5 - 2; (B) (A) after heating to 240 °C in ODE/ODA. During annealing the particles became more spherical; (C) (B) plus 2 monolayers of CdS; (D) (C) plus 3.5 monolayers of $Zn_{0.5}Cd_{0.5}S$; (E)/(F) (C) plus 2 monolayers of ZnS.

As mentioned before, the shape of the CdSe core nanocrystals is slightly elongated with particle dimensions of 3.2 nm along the crystallographic a- and b-directions and 5.8 nm along the c- direction. These values have been determined by TEM and XRD. Figure 4.3 shows the size histograms of the CdSe core and corresponding core/shell particles already shown in figure 4.2. We assume that the CdSe nanocrystals used as the core have the same volume as an ideal spherical particle with a mean diameter of 3.8 nm. The diameter of the core/shell nanoparticles increases to 5.3 nm after the growth of a 2 ML CdS shell with 3.3% standard deviation of the size distribution. With the further growth of the shell, the diameter of core/shell reaches up to 7.9 nm after coverage with 3.5 MLs of $Zn_{0.5}Cd_{0.5}S$ with 2.1% standard deviation of size distribution, and finally increased to 9.2 nm after the growth of the outmost shell of 2 ML ZnS (with 2.4% standard deviation). Thus, a core/shell nanocrystal with 7.5 MLs of the shell material, including 2 ML CdS / 3.5 ML $Zn_xCd_{1-x}S$ / 2 ML ZnS, was obtained by using the SILAR method. It should be noted that with the increase of the shell thickness, the particle size histograms narrowed further and were better than that of the plain core particles. Similar results were observed when dot-shaped CdSe particles were used as the cores.

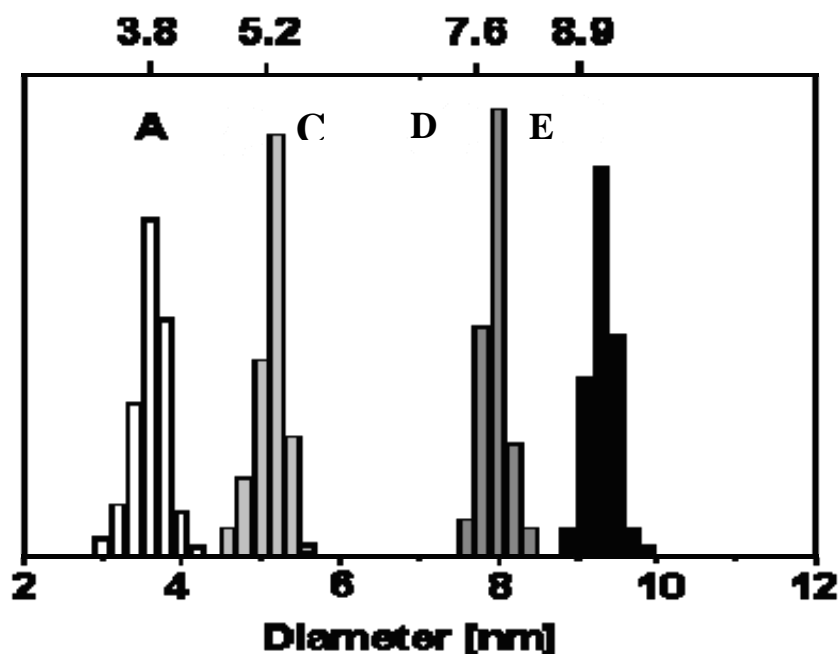


Figure 4.3 Size histograms for the series of samples shown in Figure 4.2. For the longest dimension for over 200 particles in each sample has been measured: (A) Histogram of CdSe-cores; (C) (A/B) plus 2 monolayer CdS; (D) (C) plus 3.5 monolayer $Zn_{0.5}Cd_{0.5}S$; (E) (D) plus 2 monolayer ZnS. The numbers on top mark the “theoretical” values for the expected diameters from geometric considerations.

In figure 4.4, a HRTEM image of a single CdSe/CdS/Zn_{0.5}Cd_{0.5}S/ZnS nanocrystal is shown. Similarly to most of the particles in figure 4.2F, the HRTEM image of this nanocrystal reveals continuous lattice fringes throughout the whole particle, demonstrating the highly crystalline nature of the core/shell nanocrystal. This particular particle is viewed along the crystallographic c-direction. Correspondingly, figure 4.4B shows the Fourier transform of the image, which is in almost perfect agreement with the calculated diffraction pattern of the CdSe wurzite structure, aligned along the [001] crystal face direction (Figure 4.4C). The blurry appearance at the rim of this particle shown in figure 4.4A might be due to the molecular ligands.

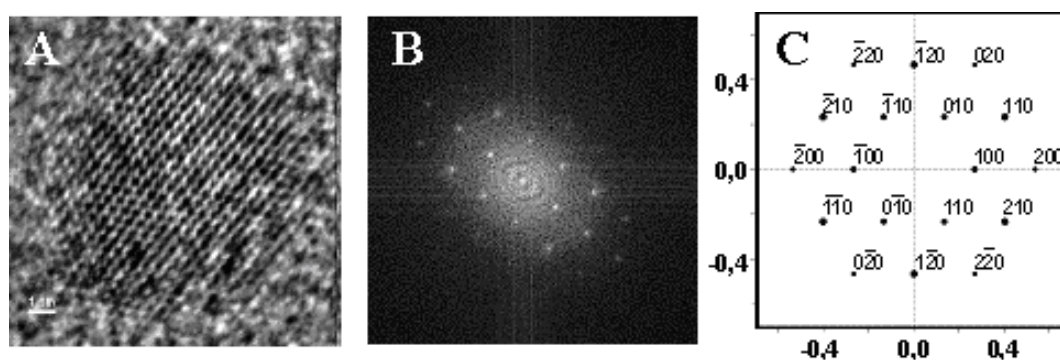


Figure 4.4. (A) HRTEM image of a CdSe/CdS/Zn_{0.5}Cd_{0.5}S/ZnS nanocrystal demonstrating its high crystallinity. (B) Fast-Fourier-Transform of the TEM image ($d_{FT(100)} = 3.77\text{\AA}$) shown in (A) which corresponds to the simulated diffraction pattern of the [001] crystal face of a wurzite CdSe particle ($d_{calc(001)} = 3.724\text{\AA}$) (C).

For comparison, we also synthesized other core/shell nanocrystals using CdSe cores of the same size, with a 6 ML CdS shell, 6 ML CdS/Zn_{0.5}Cd_{0.5}S or 6 ML ZnS shell, respectively. The TEM images of these core/shell particles are given in figure 4.5. The CdSe/CdS core/shell nanocrystals with 6ML shells shown in figure 4.5 B were prepared as reported by Peng et al. ^[143] The CdSe/ZnS core/shell nanocrystals shown in figure 4.5F were synthesized by the standard method using diethylzinc and (TMS)₂S as the precursors. The other core/shell particles shown in figure 4.5 (B-E) were synthesized by using the new “green” precursors (CdO, ZnO and S powder) and the SILAR method. It can be seen that the shape of these core/shell nanocrystals is spherical with a similar diameter of about 7 nm. However, the CdSe/ZnS core/shell nanoparticles synthesized with a thick ZnS shell showed non-spherical irregular shapes (see Figures 4.5 E and F). This indicates that the imperfect growth of a thick ZnS shell is not due to the synthetic method but rather related to the “material

difference” between CdSe and ZnS. Therefore, to reduce the interfacial strain between the CdSe core and the ZnS shell, engineering the lattice spacing by changing gradually the shell composition in the radial direction seems to be the general way to achieve narrow in situ size distributions of heterogeneous nanocrystals like the multi-shell core/shell nanocrystals shown in figure 4.5 D.

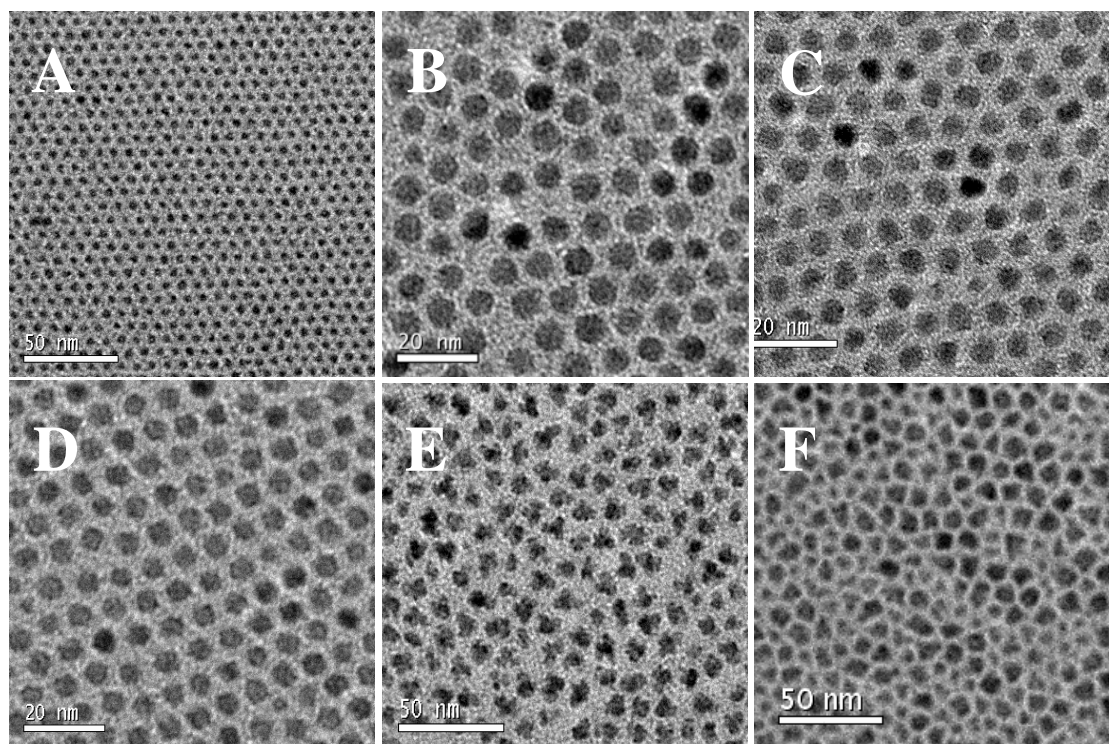


Figure 4.5. (A) CdSe cores.(B) CdSe/CdS core/shell particles, (C) CdSe/Zn_{0.5}Cd_{0.5}S core/shell-particles, (D) CdSe/2 ML CdS / 2 ML Zn_xCd_{1-x}S / 2 ML ZnS core/shell particles (E) CdSe/ZnS core/shell particles which were prepared by the SILAR method. (F) CdSe/ZnS core/shell particles which were prepared using ZnEt₂ and (TMS)₂S precursors, All core-shell particles had a nominal shell thickness of 6 MLs.

The crystallographic properties of the nanocrystals have been obtained by comparison of the powder-XRD patterns of core and core/shell nanocrystals. Figure 4.6 shows the XRD patterns of the CdSe core and several kinds of core/shell particles, and the theoretical diffraction patterns of the wurzite bulk materials of CdSe,^[148] CdS^[149] and ZnS,^[150] respectively. The powder XRD of the CdSe cores shown in figure 4.6 A comes from elongated CdSe cores which have been shown in figure 4.2 A. We found that the diffraction peak positions match the theoretical values of wurzite structure CdSe well. The only difference is that the diffraction peaks of CdSe

nanocrystals are broader than those of bulk CdSe, ^[151] which can be well explained by the reduced size of the CdSe particles. In order to prove this structure, the diffraction data (solid line) were analyzed in respect to the particle size by using a Pawley-fit ^[151] and Scherrers formula. ^[152] The calculated values are consistent with the particle dimensions of 3.2 nm across the crystallographic a- and b-directions and 5.8 nm along the c-direction, which corresponds to the TEM-results presented in figure 4.2 A.

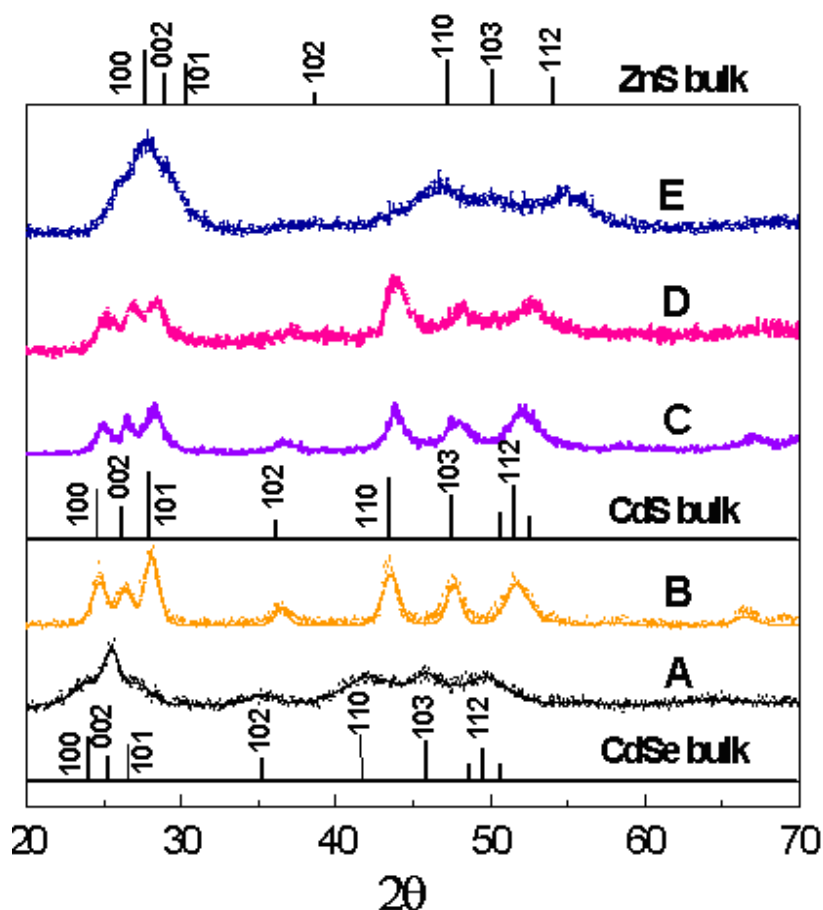


Figure 4.6 Powder XRD patterns of different samples: (A) CdSe particles, (B) CdSe+ 6ML CdS particles. (C) CdSe + 6ML Zn_{0.5}Cd_{0.5}S particles, (D), CdSe/2ML CdS/ 2 ML Zn_{0.5}Cd_{0.5}S /2 ML ZnS particles,(E) CdSe/6ML ZnS particles. The bulk wurtzite CdSe, CdS and ZnS references are given as line patterns. The solid lines of the pattern A and (black) B (yellow) are obtained by theoretical fits using the size of CdSe and CdSe/CdS particles

Powder XRD patterns of core/shell particles synthesized from the same CdSe core particles are shown in figure 4.6 (B-E). There, the core was covered with 6 MLs of different shell materials. Sample (B) is covered with 6MLs of CdS, sample (C) with 6MLs of a Zn_{0.5}Cd_{0.5}S-alloy, sample (D) with 2ML CdS/ 2 ML Zn_{0.5}Cd_{0.5}S/ 2

ML ZnS- and finally sample (E) with 6 MLs of ZnS. For all these core/shell particles, we found that the XRD peak positions are much different from those of the CdSe-core material. This indicates that all the shell materials have grown onto the surface of the CdSe cores. Since the volume fraction of the shell is more than 90% of the total particle volume. Therefore, the peak positions are much more corresponding to the shell bulk materials than to the CdSe core material. For example, the diffraction peak positions of curve (B) are very close to the values of CdS. At the same time, the diffraction peak widths are much narrower than those of the core because of the larger particle diameter. For sample, (C) (Cd/ZnS-alloy shell) and (D) (multi-layer shell) the peak positions are slightly shifted toward the bulk values of ZnS due to the increasing amount of ZnS. In fact, the outmost 2 MLs of ZnS in sample (D) have a volume fraction of about 30%, but the peak width remains relatively narrow. It shows that multi-shell nanocrystals have high crystallinity and regular shape. In contrast, the peak positions of sample E covered with only 6 MLs of ZnS are close to the ZnS values and the peak widths are very broad, although the particles have a larger diameter of about 7 nm similar to that of the samples B, C and D.

While a more detailed analysis of the diffraction patterns from the core/shell particles is desirable, several qualitative arguments can be raised from the data at hand. Especially the CdS material seems to grow without the formation of lattice defects, because the peak widths are very narrow. In a first approximation we fitted the diffraction pattern of sample (B) with the same procedure as mentioned above^[151] and obtained the hexagonal lattice parameters $a=b=0.4156$ nm and $c=0.675$ nm. These values are much closer to CdS ($a=b=0.412$ nm, $c=0.668$ nm) than to CdSe ($a=b=0.430$ nm, $c=0.701$ nm). For sample (E), where the shell consists of ZnS only, the broad diffraction peaks go along with a broad diameter distribution and irregular particle shapes as observed by TEM. Obviously, the large lattice mismatch between CdSe and ZnS leads to an imperfect shell growth and a short coherence length of the diffracted X-rays, which in turn results in broad diffraction peaks. The diffraction patterns of sample (C) and (D) appear to be very similar to each other and very much different from (E). Therefore, we assume that even though the volume fraction of ZnS is relatively high (35% in sample C and even 58% in sample D) the shell growth still happens in an epitaxial manner, because the stress can be released in the radial direction.

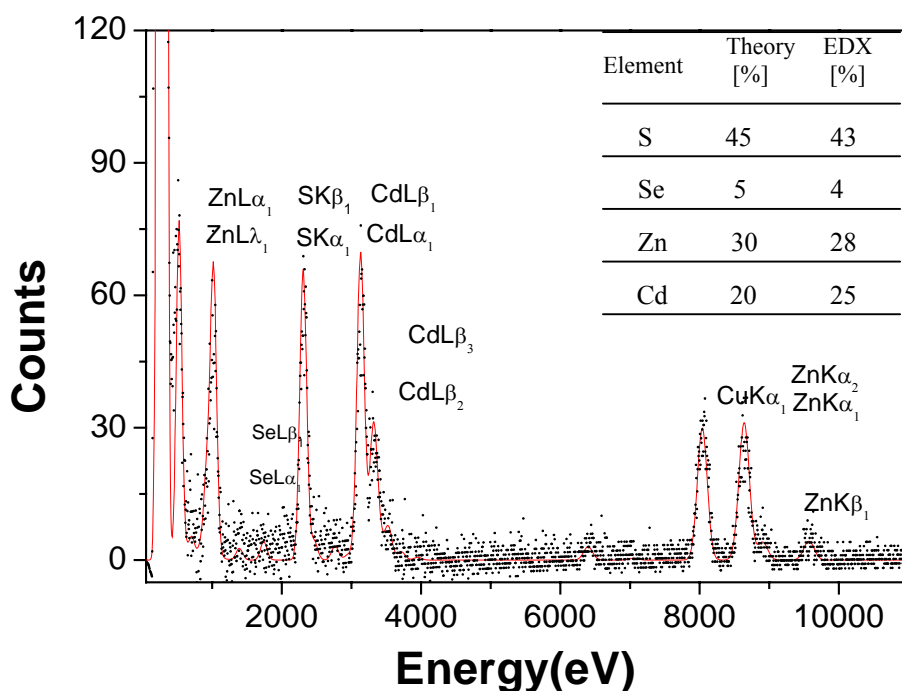


Figure 4.7 EDX spectrum of an array of 7 particles of CdSe-core (2 ML CdS / 3.5 ML $Zn_{0.5}Cd_{0.5}S$ / 2 ML ZnS)-shell nanocrystals prepared on a copper grid. The inset illustrates the comparison of theoretical and experimental values.

In order to further identify the chemical composition of the particles we used EDX spectroscopy in parallel and scanning mode. The analysis has been performed with the Cd-L, Zn-L, S-K and Se-L lines with the elements C, O, Cu and Si included in the background. To avoid the effects of drift and to reduce the contamination of the sample during measurement, we did not investigate a single particle but 5-10 particles in parallel. Figure 4.7 shows the EDX spectrum of 7 particles where the CdSe-cores were covered with a shell composition of 2 MLs CdS, 3.5 MLs $Zn_{0.5}Cd_{0.5}S$ and 2 MLs ZnS. It can be seen that the Se bands are almost completely hidden by the background signal, while the other elemental bands can clearly be resolved. However, a quantitative analysis results in a composition of $Cd_{20}Zn_{30}Se_5S_{45}$ for the 7 selected multi-shell particles investigated. This needs to be compared to the elemental distribution as calculated for an “ideal” core shell particle, which would have the stoichiometry of $Cd_{25}Zn_{28}Se_4S_{43}$. The correspondence of the theoretical and experimental values suggests that the individual particles have the composition assumed and that no separated ZnS and/or CdS particles have been formed during the shell growth.

4.2.3 Optical properties

Figure 4.8 shows the UV-Vis absorption and PL-spectra of multi-shell core/shell nanocrystals during shell growth. The spectra labeled with the letters (A-E) are corresponding to the same samples that were shown in the TEM images in figure 4.2 and the size histograms in figure 4.3. The sharp features of the absorption spectra and the narrow PL peaks are consistent with the narrow size distribution of the core/shell nanocrystals shown in figures 4.2 and 4.3. The absorption spectrum roughly maintained its overall shape after shell growth, with a slight broadening of features.

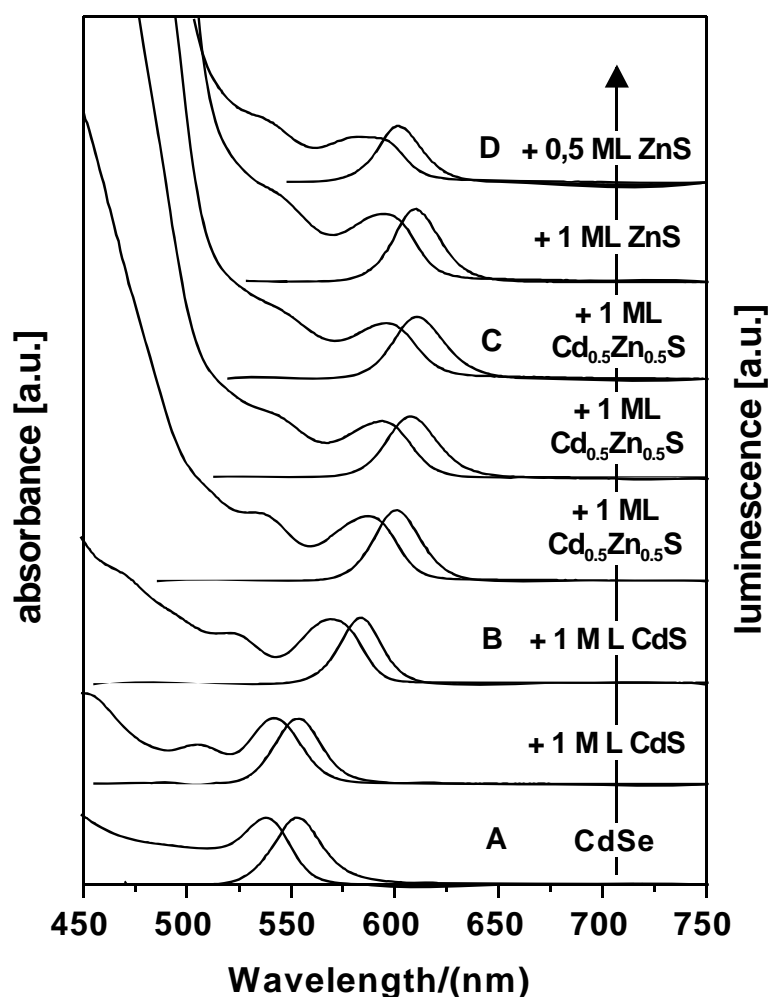


Figure 4.8 Evolution of the absorption and photoluminescence spectra upon consecutive growth of the concentric shells. The spectra labeled with the letters A-E were taken from the same samples as in the TEM pictures A-E in Figure 4.2 and the corresponding size distributions in Figure 4.3.

At the same time, the spectra shift to the red due to the larger extension of the electronic wave function leaking out into the shell materials.^[153] However, we found that a slight blue-shift was observed in the absorption and PL-spectra when the last two layers of ZnS shells were grown onto the surface of CdSe/CdS/Zn_{0.5}Cd_{0.5}S nanoparticles. An even larger blue shift in the spectrum can be observed when the reaction solution was kept for 30 min at 260 °C. In fact, such a blue shift has been reported by other research groups.^[154] For example, the growth of a composite CdS/ZnS shell onto CdSe nanorods resulted in blue shift under annealing by a laser. When CdSe nanocrystals were covered with a ZnS shell at high temperature (>250°C), interfused type nanocrystals were produced due to the diffusion of the shell components into the core at high temperatures. This resulted in a blue shift compared to the initial core reported by Jang et al.^[154] In our work, we had observed the blue-shift phenomenon only if the particles are covered with an additional ZnS shell. We think that the reason of this blue-shift observed in the spectrum is the partial formation of a Zn_xCd_{1-x}S alloy shell due to the diffusion of Zn into the core. Of course, it is very easy for the Zn atoms to diffuse into the Cd rich regions of the shell at high temperature, which has been reported by Zhong et al.^[155-157] Therefore, the blue-shift corresponds to an increase of the band-offset of the shell (from ZnS shell to ZnCdS) and hence an increase of the effective confinement.^[155, 156]

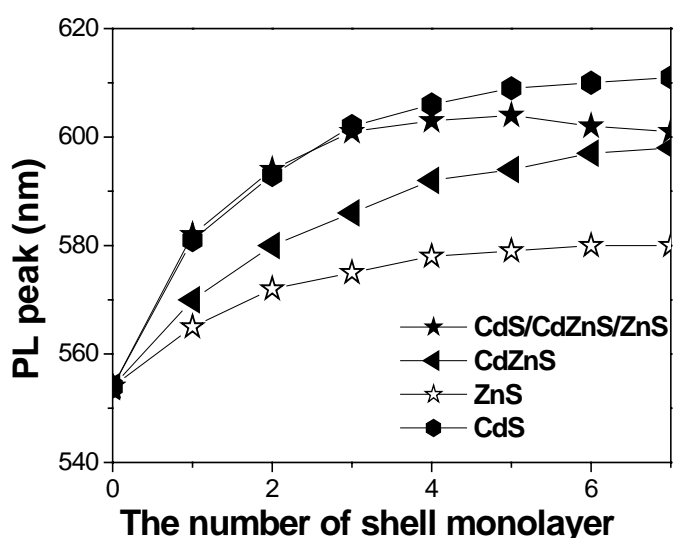


Figure 4.9 Evolution of the PL-peak position for several core/shell particles. The PL-band shifts towards longer wavelength upon shell growth on the CdSe-cores due to the decrease in confinement. The multi shell particles show a slight blue shift upon growth of the outer ZnS layers.

In order to further verify this assumption, the evolution of the PL peak position upon growth of CdSe/CdS/Zn_{0.5}Cd_{0.5}S/ZnS core/shell nanocrystals and other core/shell nanocrystals, including CdSe/CdS, CdSe/Zn_{0.5}Cd_{0.5}S and CdSe/ZnS was determined. Note that all the core/shell nanoparticles were prepared from the same batch of CdSe-cores, and were covered using same monolayer shells with different materials, respectively. Figure 4.9 presents the evolution of the PL peak position for these different core/shell particles. It can be seen that the red shift for the CdSe/CdS particles is about 55 nm after growth of 7 monolayer CdS shells. This shift is much more pronounced than for the CdSe/ZnS core/shell nanocrystals, which have a red shift of 25 nm after covering the cores by a shell thickness of 7 monolayers.

For the Zn_{0.5}Cd_{0.5}S alloy shell, the evolution of the position of the PL-band lies in between those of the ZnS and CdS shell. In case of the PL of the CdS/Zn_{0.5}Cd_{0.5}S/ZnS multi-shell, one can see that initially it follows the graph of the CdSe/CdS particles, because the first two monolayers in both cases consist of CdS. Then the position of the PL-band after the growth of three layers of the Zn_{0.5}Cd_{0.5}S alloy shifts slightly toward lower energy, and is further blue shifted upon the final growth of the outermost 2 ML of ZnS. Obviously, the final position of the PL-band is similar to that of the CdSe/Zn_{0.5}Cd_{0.5}S particles with alloyed shell. However, for the CdSe/CdS/Zn_{0.5}Cd_{0.5}S/ZnS multi-shell particle, the outermost shell comprised a volume fraction of 65 % ZnS corresponding to a volume fraction of 35% CdS only within this shell. This is in contrast to the purely alloyed shell, where the volume fractions of ZnS and CdS are equal (50%). Therefore, we assume that the blue shift mainly happens at the interface between CdS and ZnS due to the inter-diffusion effect at high temperature (260°C). On the other hand, if these shell would become genuine alloy shells, we assume that the PL position should be the same as that of the completely alloy shells shown in figure 4.9. Therefore, we conclude that the outer surfaces of the CdSe/CdS/Zn_{0.5}Cd_{0.5}S/ZnS multi-shell particles are still ZnS-rich, which could also explain the “chemical effects” discussed below.

The PL QY and full width at half maximum (FWHM) of the emission peak were recorded for growing nanocrystals with different shell thicknesses as shown in figure 4.10. The experimental results revealed that the PL QY of the core/shell nanocrystals greatly increased compared to the core nanocrystals. Peng et al. reported that the PL QY of the core/shell CdSe/CdS synthesized in TOPO using the SILAR

method is about 40%.^[147] In contrast, the PL QY of the core/shell nanocrystals in the multi-shell systems reaches up to 80%. Importantly, this value almost keeps constant with increasing shell thickness after the maximum was reached. Even if the core was covered by seven shells, the PL QY still remained at about 70%. At the same time, we also found that the PL FWHM of the core/shell nanocrystals became slightly smaller than that of the original core particles.

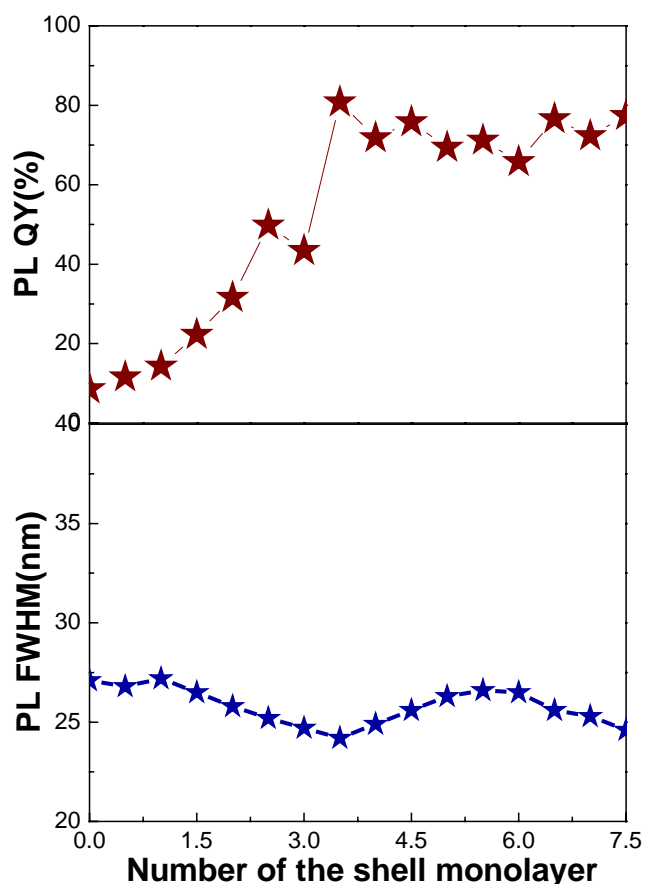


Figure 4.10 The evolution of FWHM and PL QY of CdSe/CdS/Zn_{0.5}Cd_{0.5}S/ZnS core/shell nanocrystals versus the number of shell monolayers from CdS, Zn_xCd_{1-x}S and ZnS.

For comparison, we also determined the PL-QYs of different core/shell nanocrystals prepared from the same CdSe cores. Figure 4.11 presents the PL evolution of several core/shell nanoparticles. It can be seen that the QY of the plain CdSe-core particles is of an order of 20% only. It can increase to about 60% upon coverage with two MLs of ZnS, CdS or Zn_{0.5}Cd_{0.5}S by the SILAR method, independent of the shell material. However, the further growth by addition of ZnS monolayers leads to a reproducible decrease in the QY, as shown in figure 4.11. It indicates that defects have formed after the growth of relative thick ZnS-shells.

Therefore, it is supposed that the reason for the decrease in the QY is not the growth process itself but indeed the accumulated lattice strain. In contrast, the QY for the particles with CdS-shell, Zn_{0.5}Cd_{0.5}S-shell or CdS/Zn_{0.5}Cd_{0.5}S/ZnS-multiple shell is even slightly increasing upon further shell growth. It should be noted that the absolute values were slightly different from batch to batch. The final QYs of the particles with the CdS- and Zn_{0.5}Cd_{0.5}S shells were in the range of 65%. The CdS/Zn_{0.5}Cd_{0.5}S/ZnS multi shell nanocrystals showed a slightly higher QY of about 70 %.

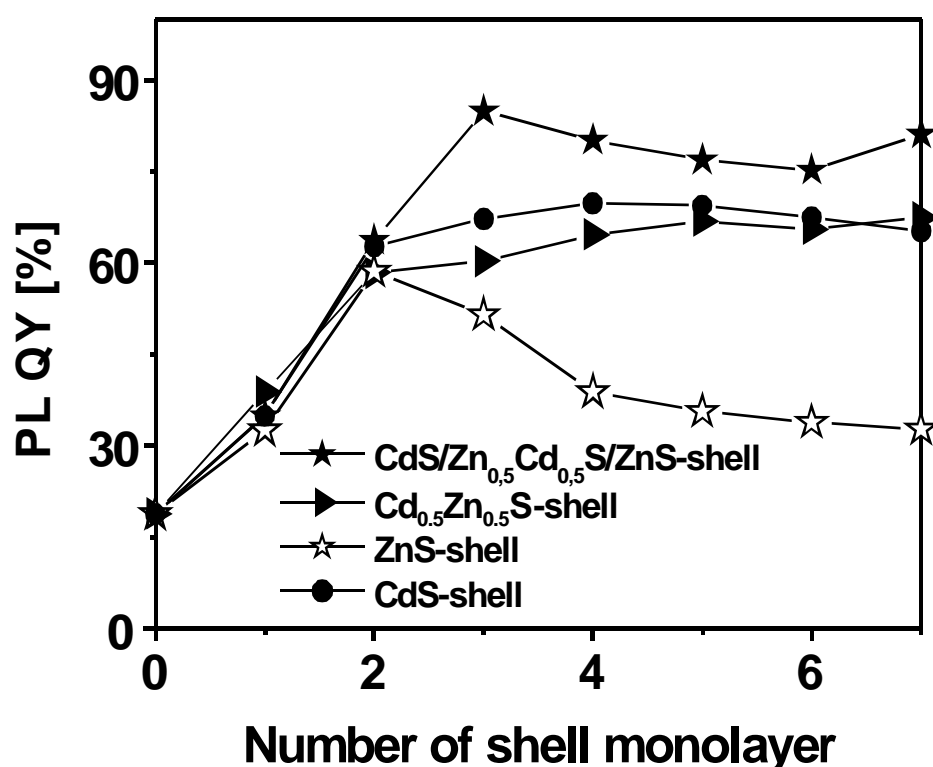


Figure 4.11 Evolution of PL QY for several core/shell particles. The QY is increasing upon shell growth due to the electronic passivation of the surface. For the CdSe/ZnS core/shell particles, the QY decreases for shell thicknesses larger than 2 MLs, probably due to lattice imperfections within the shell.

The data presented here indicate that the growth of a “sandwich alloyed shell” onto the CdSe core can decrease strain, and therefore is favorable for the growth of high quality core/shell dots. During the growth of the shell, a darkening and brightening phenomenon was reported in literature ^[147] after the S and Cd precursors were injected into the reaction mixture. This phenomenon was of minor importance in our systems as shown in figure 4.10.

4.2.4 Chemical characterization

4.2.4.1 Chemical stability

In some applications, nanocrystals need to resist many operations including site-selection separation and purification. In the following experiments, various treatments were carried out for different core/shell nanocrystals with focus on ODA/OA covered particles and the QYs before and after the treatment were determined. In general, nanoparticles show high QYs in presence of amine functionalized ligands (ODA).^[145] However, this trend can only be observed in solutions with an excess of the ligands, probably because of the dynamic exchange equilibrium between ligands on the surface and in solution.^[158] In addition, it has been reported that amines are more strongly bound to the CdSe/CdS particles than to the plain CdSe cores.^[147]

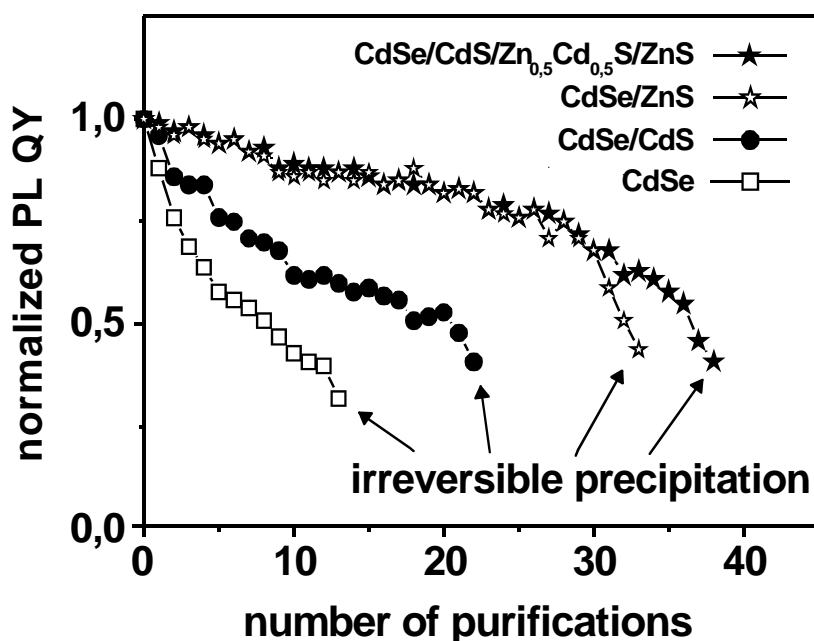


Figure 4.12: Evolution of the relative photoluminescence quantum yield upon repeated precipitation and redispersion of TOPO/ODA covered CdSe cores and several ODA covered core/shell particles in chloroform solution. The relative QY and the colloidal stability is higher for particles with an outer shell of ZnS.

Here, we investigated the “colloidal stability” in detail by performing repeated precipitation of the particles and successive redispersion in pure solvents until the nanocrystals could not be re-dispersed anymore. The CdSe core was synthesized in a 1:1 mixture of TOPO/ODA. It can be seen that the PL-QY of the CdSe cores as

shown in figure 4.12 drops very fast upon repeated precipitation by addition of methanol and redispersion into chloroform. The experiment also showed that the particles could not be re-dissolved anymore after about 10 purification cycles. Under the same conditions, the CdS covered core/shell particles could be repeatedly purified more than 20 times before they became insoluble, which is consistent with earlier observations reported by the group of Peng.^[159] However, when the outer surface shell of the nanocrystals was a ZnS shell, the nanocrystals could tolerate even more purification experiments. As shown in figure 4.12, the CdSe/ZnS particles and the CdSe/CdS/Zn_{0.5}Cd_{0.5}S/ZnS-multi-shell particles could be purified more than 30 times before they became insoluble. This suggests that the amines are more strongly bound to Zn-sites on the surface of the nanocrystals than to Cd-sites. In all cases, we found that the PL QY of core/shell nanocrystals with an outer CdS layer was lower than that of nanocrystals with ZnS shells. It should be noted that the absolute PL-QY of the multi-shell particles is still of the order of 25% before irreversible precipitation, while the QYs of the CdSe/CdS and CdSe/ZnS core shell particles is only 10-15% and 5-10%, respectively.

4.2.4.2 Photochemical stability

An important issue especially for the use of semiconductor nanocrystals in optical applications is the evolution of the optical properties under continuous irradiation. The photochemical stability of the nanocrystals exposed to O₂ under UV light radiation was studied in a similar fashion as described in the literature.^[159] The nanocrystal solutions were irradiated by UV light with high power (100W) in presence of O₂. In this context it is often observed that nanocrystals degrade with increasing irradiation time due to photo oxidation.^[144] The evolution of the optical density and relative fluorescence intensity upon irradiation of oxygen saturated solutions of the different nanoparticles in chloroform are shown in figures 4.14 A and 4.14 B, respectively. It can be seen that the absorption of the CdSe particles drops rapidly and the particles precipitate after an irradiation period of 1.5 h. As described in literature,^[29] CdSe particles overcoated with a CdS shell show high chemical and photochemical stability. By comparison of the different core/shell particles, we found that the nanocrystals with a topmost layer of ZnS were most stable, and the optical density changed only slightly until the particles precipitated from solution, i.e. after 12 days for the particles with the pure ZnS-shell and 10 days for the multi-shell particles.

The stability of the CdSe/CdS core/shell nanoparticle was in between, which means that CdS is more sensitive to oxygen than ZnS.

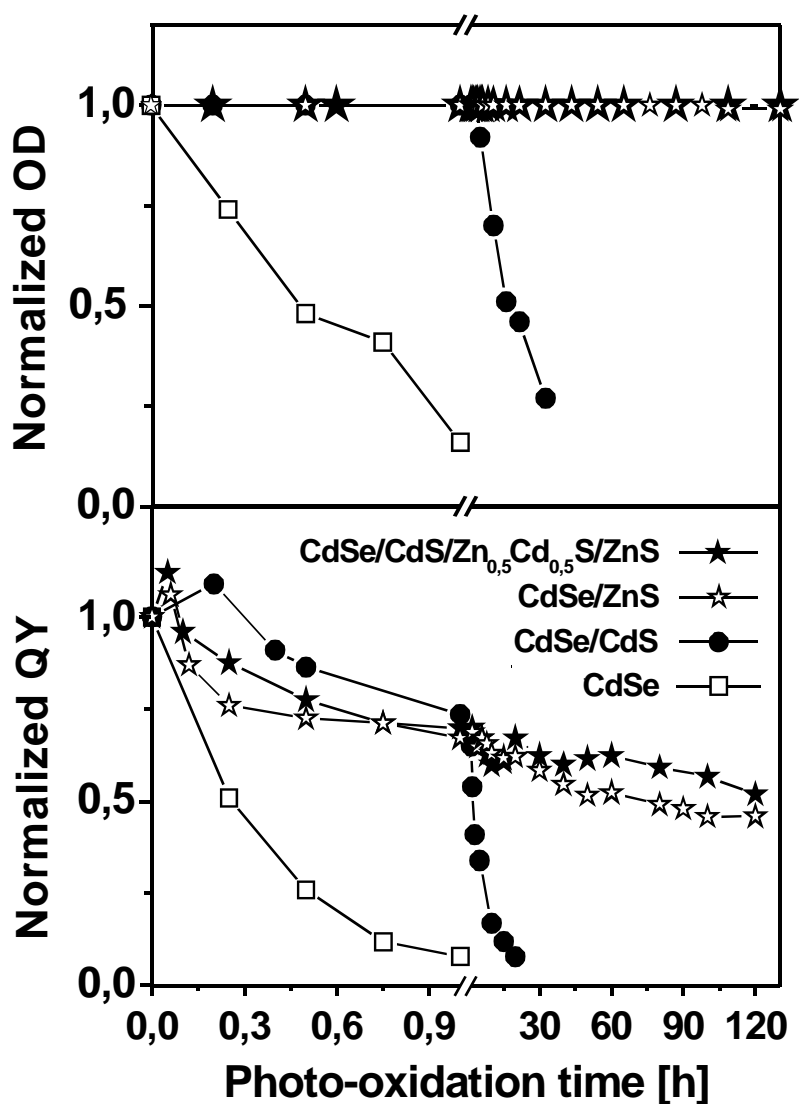


Figure 4.14 Photo-chemical stability of nanocrystals in oxygen saturated chloroform solutions under UV-irradiation. **A:** Change in optical density and **B:** change in photoluminescence quantum yield for the CdSe-cores and different core shell particles (for details: see text).

While studying the PL properties of the nanocrystals under photo-oxidation conditions, a brightening phenomenon was observed only the first minutes of irradiation for most of the particles^[160] as shown in figure 4.14 B. At longer times the PL QY of all samples investigated decreased little by little, most likely as a result of photo oxidation processe on the particle surface. In general, we could observe a

similar trend as for the change of the absorption spectra. The fluorescence of the pure CdSe nanocrystals decreased very fast and was accompanied by a blue shift of the fluorescence band position from 570 to 510 nm, which is attributed to a shrinking of the CdSe core. The fluorescence intensity of the CdSe/CdS core shell particles decreased to a lower degree initially, and we could also observe a shift of the fluorescence band; in this case from 620 nm to 610 nm. In contrast, a shift of the fluorescence band could neither be observed for the CdSe/ZnS particles nor for the multi-shell particles. At the same time, the fluorescence intensities of those samples decreased only by approximately 50% upon illumination for more than 120 hours.

Obviously, the particles with an outer layer of ZnS show a much higher photochemical stability. This is most likely due to the higher band offset introduced by the ZnS material as compared to CdS, which results in a lower charge density of the photo generated charge carriers on the particle surface and hence a lower probability of surface oxidation. Therefore, the particles with an outer layer of ZnS show a higher chemical stability and also a higher long-term fluorescence intensity.

4.2.4.3 Thermal stability

The thermal stability of the nanocrystals was studied applying similar methods as reported in literature. ^[159] The purified nanocrystal powder was examined by sintering at 150°C for about 2 days under air. The experimental results indicate that the plain core CdSe nanocrystals did not resist the harsh heating treatment. After sintering, the product could not be dissolved in organic solvents, and showed no PL

Table 4.1. PL QY of the core and core/shell nanocrystals before and after sintering at 150°C under air.

	QY in %			
Sample	CdSe	CdSe/CdS	CdSe/ZnS	CdSe/CdS/ZnCdS/ZnS
before sintering	26	51	38	69
after sintering	0	28	28	53

emission. For the core/shell nanocrystals, we found that the nanocrystals were all well maintained and no change of the UV absorption and PL spectra was detected, besides a decrease of the PL QY for all the samples as given in table 4.1. It should be stressed that the PL QY of CdSe/CdS and CdSe/ZnS core/shell nanocrystals after sintering still remains at about 50% and 70% of their original values respectively. However, the QY of the new multi-shell core/shell nanocrystals after sintering was even at 80% of its original value. The excellent thermal stability of the core/shell nanocrystals shows that irreversible aggregation of the nanocrystals in the solid state can be efficiently suppressed after growth of thick inorganic shells onto the core. These results show that the storage times of nanocrystals can be improved by coating with a thick inorganic shell, which prevents photo-oxidation and agglomeration at high temperatures.

4.3 Conclusion

A synthetic procedure for the production of multi-shell nanocrystals based on the idea of crystal lattice similarity has been developed during this thesis. To combine the advantages of both CdS shell and ZnS shell materials, we have used the newly developed SILAR technique to gradually change the shell composition in radial direction from CdS to ZnS. In this way, the lattice strain can relax in radial direction and the particles show a high crystallinity, similar to pure CdS shells. At the same time, the band offsets are quite high and the particles are electronically well passivated, similar to pure ZnS-shells. The new multilayer structure of the shells with different band gap energies decreases greatly strain during the growth of the shells. It therefore is favorable for forming high quality nanocrystals even if seven monolayer shells are coated onto plain core nanocrystals. In addition, the PL QY of multi-shell core/shell nanocrystals can reach about 80% with a corresponding FWHM in emission band of about 22-27 nm. This narrow spectral width mainly arises from the uniform particle size and shape. The experiments presented in this chapter show that the new multi-shell core/shell nanocrystals possess superior stability against photo-oxidation, chemical oxidation, thermal treatments and processing in comparison to corresponding plain core nanocrystals and other core/shell nanocrystals, such as CdSe/CdS and CdSe/ZnS. The results also show that the passivation shell of semiconductor nanocrystals can now be engineered in a defined way leading to particles with high crystallinity, well defined electronic structure and distinct chemical

surface properties. The extremely stable multi-shell nanoparticles therefore should be an ideal species for studying size dependent chemical and physical properties.

4.4 Preparation methods

A: Synthesis of CdSe cores: TOPO capped CdSe nanocrystals were synthesized using the following standard method:^[88] For a typical reaction, a mixture of 0.0514 g CdO powder, 0.224 g TDPA, 4.0 g TOPO (or 4.0 g TOPO/ODA-mixture) in a 50 ml three-neck flask was degassed in vacuum for 1 hour and heated to 320 °C under Ar-flow to form an optically clear solution. Then the temperature was lowered to 270 °C, and a solution containing 0.0632 g of Se dissolved in 2.0 g of TBP was injected into the reaction flask. After the injection, the temperature was adjusted to 250 °C for 1 min. After this time the heating mantle was removed and about 15 ml of methanol were injected into CdSe nanocrystal solution (at a temperature of 100 °C) leading to a precipitation of the nanocrystals. After centrifugation and decantation, the particles were dispersed in chloroform or toluene for further processing.

B: Synthesis of CdSe/ZnS core/shell particles using the “traditional” method.^[32] The ZnS shell growth using the “traditional method” was performed as described in the literature. In a typical synthesis, a flask containing 5.0 g of TOPO was heated to 100 °C under vacuum for 1 hour and then cooled to 60 °C. A defined amount of CdSe NCs dispersed in toluene was transferred into the reaction vessel via a syringe, and the toluene was pumped off under vacuum. The solution was heated to the desired temperature (135 °C -230 °C), at which a calculated amount of ZnEt₂ and (TMS)₂S dissolved in TBP was added dropwise into the vigorously stirred reaction mixture during a period of 5-10 min. This stock solution should be handled with care because of the toxicity of ZnEt₂ and the peculiar stench of the (TMS)₂S. After the addition was complete, the mixture was cooled to 100 °C and left stirring for 2 hours. Finally, the CdSe/ZnS-core/shell nanoparticles were precipitated by addition of methanol, filtered and redispersed for further processing.

C: Preparation of the precursor solution: for shell growth using the SILAR method:^[47] we used precursor solutions containing only metal oxides (CdO and ZnO), elemental sulfur and selenium. The zinc precursor solution (0.1 M) was prepared by dissolving ZnO (0.2034 g) in oleic acid (6.18 g) and ODE (18.0 ml) at

310 °C. The cadmium precursor solution (0.1 M) was prepared by dissolving CdO (0.3204 g) in oleic acid (6.18 g) and ODE (18.0 ml) at 240 °C. The Zn/Cd=1/1 precursor solution (0.1 M) was prepared by dissolving ZnO (0.1017 g) as well as CdO (0.1602 g) in oleic acid (6.18 g) and ODE (18.0 ml) at 300 °C. The sulfur precursor solution (0.1 M) was prepared by dissolving sulfur in ODE at 180 °C. All these solutions were freshly prepared under Ar-atmosphere. The Cd-, Zn- and Cd/Zn-precursor solutions were kept at about 80 °C while the sulfur injection solution was allowed to cool down to room temperature. For each shell growth, a calculated amount of a given precursor solution was injected with a syringe using standard air-free procedures.

D: Calculations of the amount of precursor materials for shell growth: The growth of core/shell nanocrystals using the SILAR method is based on alternating injections of the Zn/Cd- and S-precursors into the solution containing the CdSe-core NCs. The concentration of CdSe-core NCs can be estimated on the basis of UV-Vis spectra. [80, 161] The amount of the injection solution for each monolayer can be deduced from a calculation of the number of surface atoms. In this paper, the average thicknesses of one CdS-ML (0.35 nm) and one ZnS-ML (0.31 nm) are estimated on the basis of the wurzite structure of the respective compounds. Hence the thickness of one monolayer of the alloyed shell ($\text{Zn}_{0.5}\text{Cd}_{0.5}\text{S}$) is assumed to be 0.33 nm, which is consistent with reports from the literature. [156, 162]

E: Preparation of core/shell nanocrystals using the SILAR technique: The SILAR technique allows for growing very complex shells around a given CdSe-core particle. After slightly changing the reaction conditions reported by Li et. al., we synthesized CdSe/ZnS, CdSe/CdS, CdSe/ $\text{Zn}_{0.5}\text{Cd}_{0.5}\text{S}$ and CdSe/CdS/ $\text{Zn}_{0.5}\text{Cd}_{0.5}\text{S}$ /ZnS core/shell nanocrystals with a similar diameter from the same CdSe-core particles. A typical SILAR synthesis was performed as follows: 3 ml ODE and 1 g of ODA were loaded into a 50 ml reaction vessel, heated to 100 °C under vacuum for 1 hour and cooled down to room temperature. The CdSe-NCs in hexane (1.83×10^{-7} mol) were added and the system was kept at 100 °C under vacuum for 30 min to remove the hexane and other undesired materials of low vapor pressure. Subsequently, the solution was heated to 245 °C under Ar-flow and the shell growth was performed. To calculate the amount of Cd-precursor for the growth of the first monolayer, we assumed that the surface of the CdSe-cores consists equally of Se- and Cd-atoms and

therefore used only 50% of the amount of calculated Cd-precursor for a complete ML. Hence, for the “first injection” we used only 0.19 ml instead of 0.37 ml of the Cd-precursor solution. This is followed by alternating addition of Zn-, Cd- or Zn/Cd-precursors and sulfur precursor, respectively. The choice of this growth temperature was the result of an optimization procedure (200–260°C) where the optimization parameter was the fluorescence quantum yield of the CdSe/ZnS core/shell particles after shell growth. The injection solution was quickly added into the reaction flask by alternating addition of Zn-, Cd- or Zn/Cd-precursors and sulfur precursors, respectively, the amount of which was calculated from the respective volumes of concentric spherical shells with a thickness of one hypothetical monolayer. We found that a period of 10 min between each addition was sufficient for the reaction to be completed, because the UV-Vis- and PL-spectra showed no further changes after this time period. The complete coverage procedure of CdSe cores with 2 MLs of CdS, 3.5 MLs of $\text{Zn}_{0.5}\text{Cd}_{0.5}\text{S}$ and 2 MLs of ZnS took about 3 h in total. After this time the solution was kept for another 30 min at 260 °C and finally cooled down to room temperature. For purification 10 ml of hexane were added and the unreacted compounds and by-products were removed by successive methanol extraction at least three times until the methanol phase was clear.

5. Synthesis and characterization of type-II ZnTe/CdX (X=S, Se, Te) core/shell nanocrystals

5.1 Introduction

In the last decade much effort has been focused on core/shell nanocrystals such as CdSe/CdS, ^[29, 147] CdSe/ZnS ^[32] or multi-shell varieties as reported in the literature. ^[163-165] Type-I core/shell semiconductor nanocrystals possess band offsets with the conduction band of the shell (the higher band gap material) higher in energy than that of the core (the lower band gap material), while the relative energies are opposite in the valence band. As a result, charge carriers are mostly confined in the core region, and consequently, the band gap of type-I core/shell particles remains almost constant or shows only a small red-shift in the absorption spectra upon shell growth as compared with the plain core nanocrystals. In contrast to type-I nanocrystals, ^[31, 35, 166] few studies have been carried out on colloidal type-II core/shell nanocrystals ^[36-38] where both the valence and conduction bands of the core are lower (or higher) in energy than those of the shell material. As a result, one carrier is mostly confined to the core, while the other is mainly confined to the shell. Type-II nanocrystals are expected to have many novel properties that are fundamentally different from type-I nanocrystals or binary nanocrystals because of the spatial separation of the charge carriers. For example, type-II structures should give access to PL wavelengths that would otherwise not be available with a single material. In addition, the separation of charges in the lowest excited state of type-II nanocrystals should render these materials more suitable for photovoltaic or photoconduction applications.

In view of this goal, we report here the synthesis and properties of colloidal type-II core/shell nanocrystals, in which different materials were grown onto ZnTe cores. Figure 5.1 presents the band edge positions and band gaps of bulk ZnTe, CdSe, CdS and CdTe. From this diagram it is inferred that in the type-II quantum dots (ZnTe/CdSe, ZnTe/CdS and ZnTe/CdTe) the hole should be mostly confined to the ZnTe core, while the electron should be found predominantly in the CdSe, CdS or CdTe shells. Therefore, the recombination process of excitons involves both the ZnTe core and the corresponding shells, which should give rise to emission energies that are smaller than the band gap of either material. Detailed results will be discussed in the following.

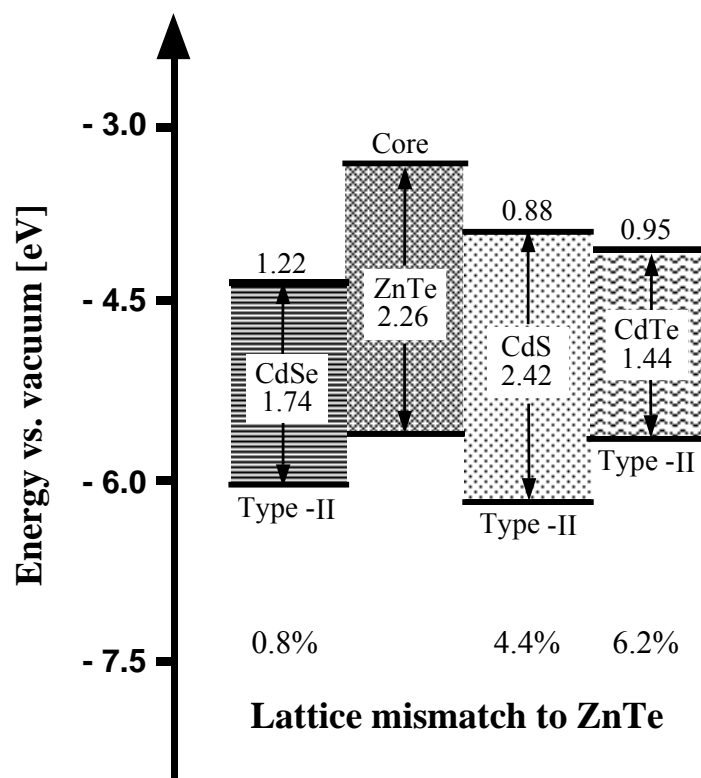


Figure 5.1 Bulk values of the band edge positions and band-gaps for different II-VI semiconductors. The band offsets and lattice mismatches (for zinc blende structure in %) are given relative to ZnTe

5.2 Results and discussion

So far, reports about synthesizing colloidal ZnTe nanocrystals with a bulk direct band gap of 2.26 eV and lattice parameter of 6.10 Å have been rather limited, most likely due to the lack of appropriate synthetic approaches.^[167-169] Furthermore, the preparation of colloidal core/shell nanocrystals with ZnTe cores has not been mentioned in the literature, although ZnTe/CdS,^[170] ZnTe/CdTe^[171] and ZnTe/CdSe^[172] heterostructures assembled by molecular beam epitaxy have been widely studied. Here a one-pot high-temperature route was used to grow ZnTe cores and core/shell nanocrystals with CdSe, CdS and CdTe shells, respectively. The high reaction temperature (270 °C) is necessary to achieve higher crystallinity of the ZnTe nanocrystals in the presence of ODA or oleylamine. We also found that primary amines are important for the growth of ZnTe nanocrystals since ZnTe nanocrystals could not be obtained by using other solvents such as TOPO. For the synthesis of the core/shell structures, we adopted the successive ion layer absorption and reaction

technology (SILAR) to grow CdSe, CdS and CdTe shells onto ZnTe cores with precise thickness control at 240 °C.

5.2.1 Structural characterization

5.2.1.1 TEM

Figure 5.2 shows TEM images of ZnTe nanocrystals at different reaction states. We found that the formation of high-quality ZnTe nanocrystals is favored at a short reaction time (Figure 5.2 A; 3 min.). The ZnTe nanocrystals show a broad size distribution after 5 minutes due to ripening process (Figure 5.2 B). In addition, ZnTe nanocrystals with larger size as shown in figure 5.2 C were obtained by multiple injection methods.

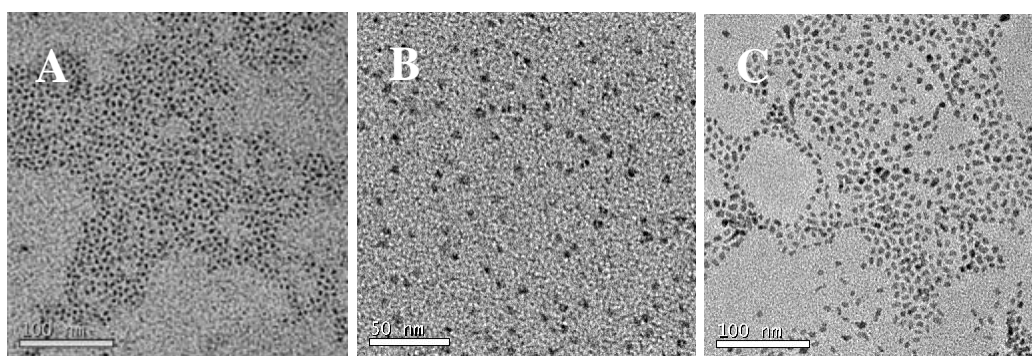


Figure 5.2 TEM images of ZnTe nanocrystals. (A): reaction time -3 minutes. (B): reaction time - 5 minutes. (C) ZnTe nanocrystals with larger size by multi-injection method.

To monitor the growth of the shells and to characterize the structure and composition of the prepared particles, several techniques have been employed. The wide-field TEM-images shown in figure 5.3 (A-E) illustrate nearly uniform size and spherical morphology of the ZnTe nanocrystals and the corresponding representative ZnTe/CdSe core/shell nanocrystals with different shell thicknesses. Image (A) of figure 5.3 shows ZnTe nanocrystals with a diameter of 4.5 nm and narrow size distribution, which is a prerequisite for growing high quality core/shell nanocrystals. With the growth of the CdSe shell, the sizes of the spherical core/shell nanocrystals (TEM size; 1 ML: $d = 5.3$ nm, 2MLs: $d = 5.8$ nm, 3 MLs: $d = 6.5$ nm: 4 MLs: $d = 7.0$ nm) are approximately consistent with the theoretical values (after growth of CdSe

shell; 1 ML: $d = 5.1$ nm, 2MLs: $d = 5.7$ nm, 3 MLs: $d = 6.3$ nm: 4 MLs: $d = 6.9$ nm) predicted by the core size and the shell thickness of particles prepared by the SILAR technique.

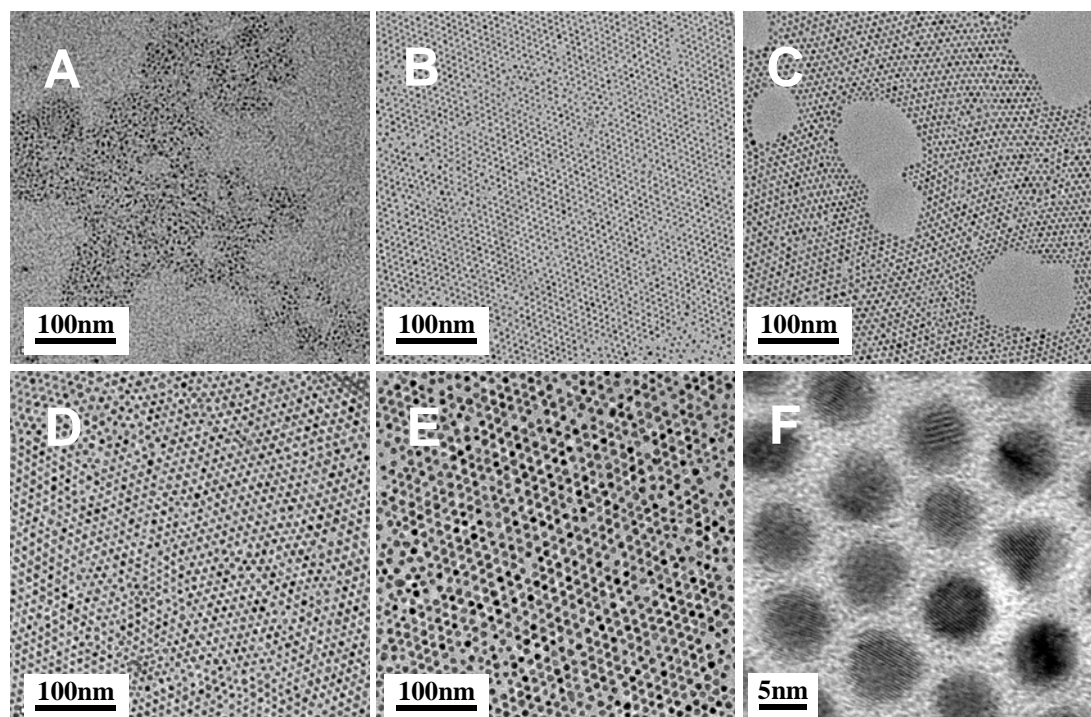


Figure 5.3 TEM images of ZnTe cores and the corresponding ZnTe/CdSe core/shell nanocrystals with different shell thicknesses. The shells were grown successively onto the same ZnTe cores. (A): ZnTe nanocrystals with a diameter of 4.5 nm. (B)-(E): TEM images of ZnTe/CdSe core/shell nanocrystals with 1-4 monolayers of CdSe; (F): HRTEM of ZnTe/CdSe core/shell nanocrystals with 4 monolayers of CdSe (same particles as in (E)).

Figure 5.3 (B-E) presents ZnTe/CdSe core/shell structures with shell thicknesses of 1-4 monolayers. It can be seen that the core/shell particles formed well-ordered two-dimensional superlattices, which indicates the uniformity of the size and shape of the core/shell nanocrystals. Figure 5.3 F shows a high-resolution transmission electron microscopy (HRTEM) image of ZnTe/CdSe nanocrystals with a shell thickness of 4 monolayers (MLs) and overall diameter of about 7.0 nm. The crystalline interior is clearly visible, demonstrating the highly crystalline nature of these core/shell nanocrystals.

5.2.1.2 Size distribution

We also performed the synthesis of other type-II core/shell nanocrystals by using the same technique, in which case the shell materials are CdS and CdTe,

respectively. For comparison, the core/shell particles were prepared from the same batch of ZnTe cores as shown in figure 5.3 A. The SILAR method allowed one to grow the same number of monolayers for each shell material. Figure 5.4 presents the images of core/shell nanocrystals with shell thickness of 4 monolayers from different materials and the corresponding size histograms.

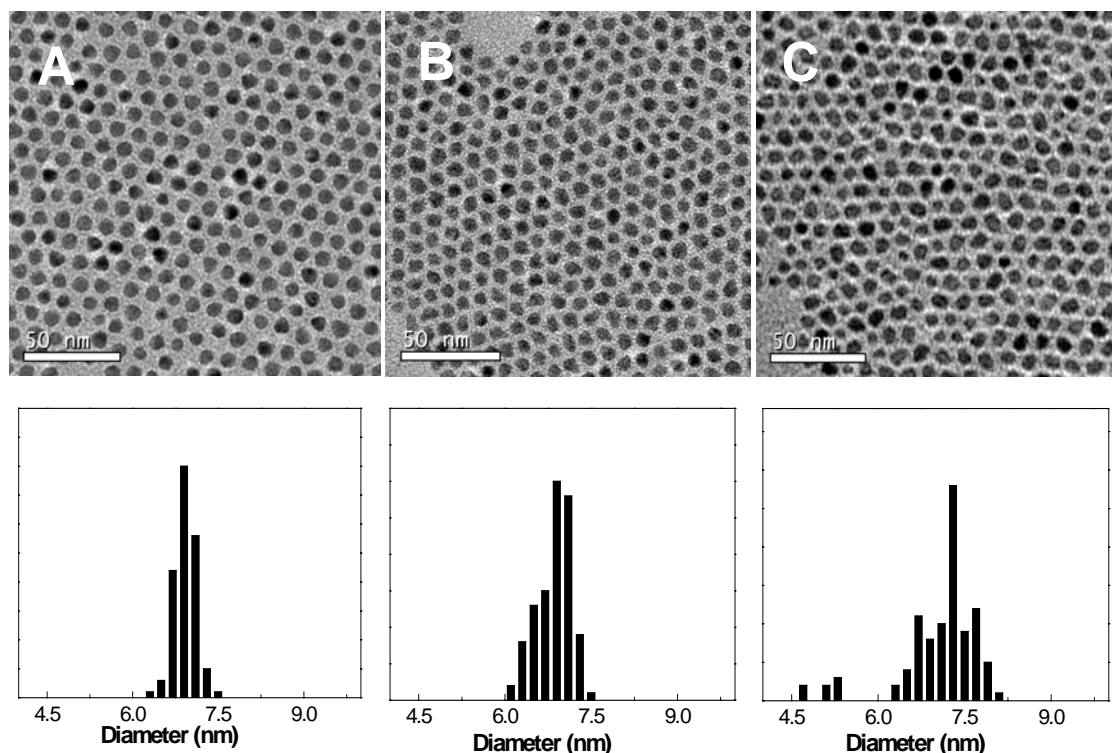


Figure 5.4 TEM images of core/shell nanocrystals based on ZnTe cores with 4 monolayer shells from different materials and corresponding size histograms. The diameter of the ZnTe nanocrystal core is about 4.5 nm. Over 200 particles in each sample have been measured: (A) ZnTe/CdSe core/shell particles. (B) ZnTe/CdS core/shell particles. (C) ZnTe/CdTe core/shell particles. (D), (E) and (F): Histograms of core/shell nanocrystals from (A), (B) and (C) respectively. Scale bar =50 nm.

The size distributions were determined by measuring more than 200 particles of each sample. The standard deviation was calculated using the following formula: $\{\sum(x_i-X)^2/(n-1)\}^{1/2}$, where X is the mean particle size, x_i is the size of particles measured ($i = \text{number } 1, \text{ number } 2 \dots n$) and n is the number of particles measured. The core size is 4.5 nm, and it grows to 7 nm by the addition of the CdSe shell (with 4.1 % standard deviation of the size distribution), 6.9 nm by the addition of the CdS shell (with 5.2% standard deviation of the size distribution) and 7.2 nm by the addition of the CdTe shell (with 8.5% standard deviation of the size distribution). We

found the size histogram of ZnTe/CdSe core/shell nanocrystals to be much narrower than that of ZnTe/CdTe core/shell nanocrystals, while the size histogram of ZnTe/CdS core/shell particles lies in between. Concerning the above material combinations, the lattice parameters of the two components of the core-shell structures is important for the size distribution of particles. For instance, the lattice mismatch is only 0.8 % between CdSe and ZnTe, and a narrow size distribution of ZnTe/CdSe particles was achieved without any purification and post process. Thus, strain effects are negligible during growth of the shells. On the contrary, ZnTe/CdTe core/shell nanocrystals show a broad size distribution due to the larger lattice mismatch (6.2 %) between ZnTe and CdTe. In case of ZnTe/CdS nanocrystals, the lattice mismatch between ZnTe and CdS is 4.4 %. Therefore, the size distribution is in between.

5.2.1.3 XRD

To further characterize the core/shell structures, their crystallographic properties were determined by powder X-ray diffraction (XRD). Figure 5.5 illustrates the diffraction patterns of ZnTe cores and those of ZnTe/CdSe, ZnTe/CdS and ZnTe/CdTe core/shell particles. The ZnTe XRD pattern consists of the characteristic peaks of zinc blende ZnTe, and the peak positions of the ZnTe cores are in agreement with those from bulk zinc blende ZnTe. In case of the ZnTe/CdSe core/shell nanocrystals, the XRD peak positions shift slightly as compared with the ZnTe cores.

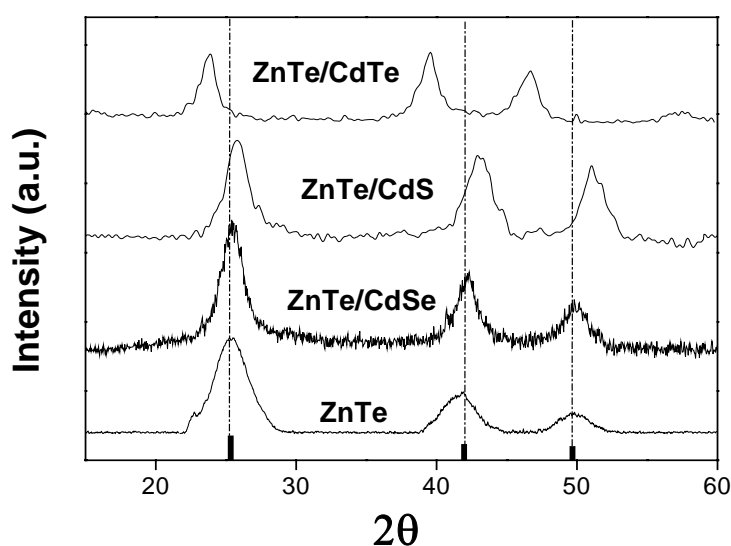


Figure 5.5 XRD patterns of ZnTe nanocrystals and ZnTe/CdSe, ZnTe/CdS and ZnTe/CdTe core/shell nanocrystals. The shell thickness is 4 monolayers in each case. The black bars at the bottom represent the XRD pattern of bulk ZnTe (zinc blende). The lattice parameters are: ZnTe=0.61 nm, CdS=0.5832 nm, CdSe=0.605 nm, CdTe=0.648 nm.

This is consistent with the similar crystal lattice parameter between the zinc blende ZnTe ($a = 0.61$ nm) and the zinc blende CdSe ($a = 0.605$ nm). For the CdS and CdTe shells, the peak positions shift to higher and lower diffraction angles in respect to the ZnTe core spectrum, i.e. towards the positions of bulk CdS ($a = 0.5832$ nm) and CdTe ($a = 0.6477$ nm) zinc blende lattice respectively. In conclusion, the XRD patterns in figure 5.5 indicate that core/shell nanocrystals could be grown from different material combinations.

5.2.1.4 EDX

To determine the composition of ZnTe/CdSe core/shell particles, we used energy dispersive X-ray diffraction (EDX) spectroscopy in parallel and scanning mode. To avoid the effects of drift and to reduce the contamination of the sample during measurement, we did not investigate a single particle but several (5-10) particles in parallel. Figure 5.6 shows the EDX spectrum of seven particles. It can be found that the intensities of the signals from Cd, Se, Te and Zn correspond to the expected values, which suggests that the individual particles have the composition assumed and that no secondary CdSe particles have been formed during the shell growth. The data of XRD and EDX indicate that the shell growth is epitaxial in our system.

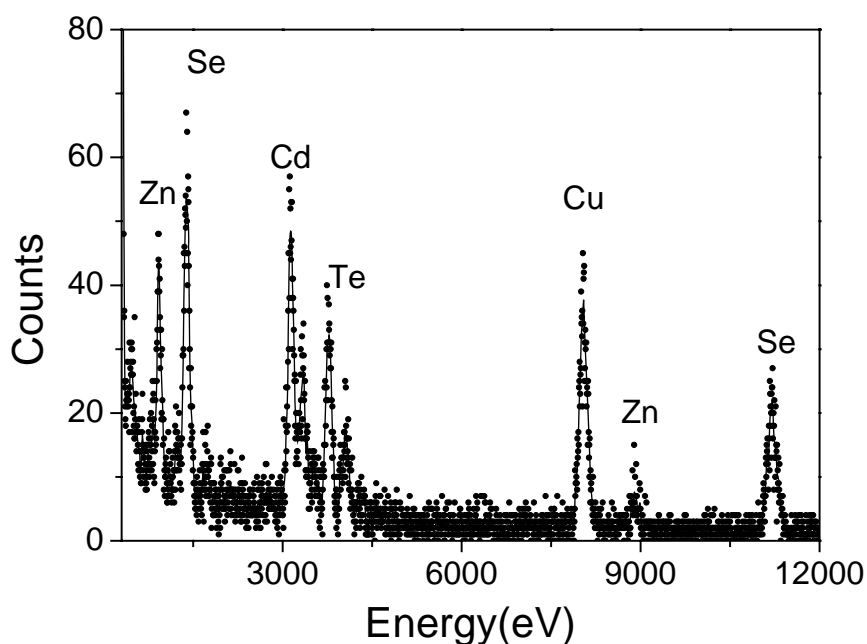


Figure 5.6 EDX spectrum of an array of 7 ZnTe/ CdSe core/shell particles (4 MLs CdSe shell) prepared on a copper grid.

5.2.2 Optical properties

5.2.2.1 Absorption

Figure 5.7 shows the temporal evolution of the absorption spectrum of amine-coated ZnTe particles monitored in the region of the first excitonic transition during the growth at 270 °C. In our system, we found that ZnTe nanocrystals showed a broad size distribution and irregular particle shape after a reaction time of 5 minutes at 270 °C (Figure 5.2 B). To overcome this drawback, we can prepare larger nanocrystals by a multi-injection method, where the precursors were alternately added into the prepared ZnTe solutions. For instance, the purple line shown in figure 5.7 is the absorption spectrum of ZnTe nanocrystals with diameter of ~ 8 nm. It should be noted that the quality of the nanocrystals (size, size distribution) varies for different batches of ZnTe nanocrystals, especially if larger nanocrystals are prepared. In addition, we have found that ZnTe nanocrystals are very sensitive to oxygen. For example, if the samples were exposed to air for several minutes, the solution color changed from slight yellow to slight black.

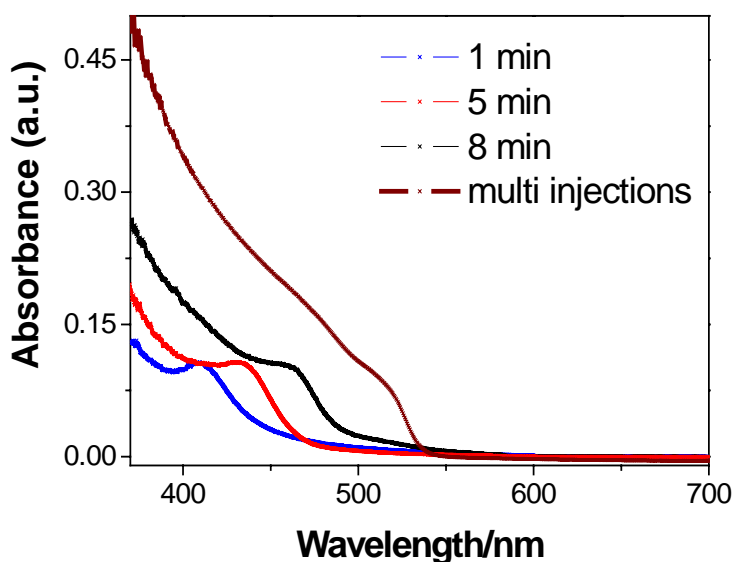


Figure 5.7 Absorption spectra of ZnTe nanocrystals. Blue, red and black lines present the evolution of absorption spectra during a typical reaction. The green line corresponds to larger particles obtained by multiple injection of precursors ($Zn(Et)_2$ and $TOPTe$).

The first excitonic peak visible in figure 5.7 is different from the very broad shoulder reported in the literature,^[167] which confirms that ZnTe nanocrystals

prepared according to the procedure described here have a comparatively narrow size distribution consistent with the TEM images (Figure. 5.3 A). However, we still observed a long tailing of the absorbance in the low energy region. This means that some particles may have been oxidized when the absorption spectra were measured.

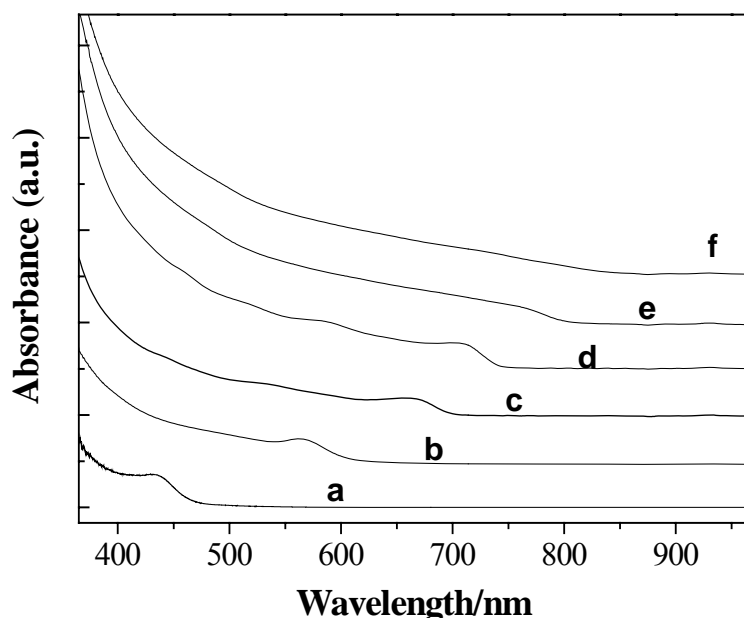


Figure 5.8 Absorption spectra of ZnTe/CdSe core/shell nanocrystals with increasing shell thickness. a) Core with 2.2 nm in radius, core/shells with shell thickness in number of monolayers: b) 0.5, c) 1.0, d) 2.0, e) 3.0, f) 4.0.

Figure 5.8 presents the evolution of absorption spectra upon growth of a CdSe shell on a ZnTe core. It is found that the shell growth is accompanied by a large red shift of the first absorption peak which is discernible up to two monolayers of CdSe. We also found that the absorption spectrum becomes completely featureless and the absorption tail shifts into the IR region ($\lambda > 800$ nm) after the growth of 4 monolayers of CdSe shell. On one hand, we know that the bulk band gaps of ZnTe and CdSe are 2.26 eV and 1.74 eV, respectively. This means that both ZnTe and CdSe nanocrystals do not lead to an emission larger than 550nm or 700 nm. On the other hand, the size of the particles is only about 7.0 nm after the growth of 4 monolayers onto the core. In combination of these factors, we assume that the pure materials (ZnTe or CdSe) can not show near infrared absorption. It had been predicted ^[173] and then experimentally verified that type-II core/shell nanocrystals have relatively small absorbance near the band edge.^[36] This weak oscillator strength of type II nanocrystals results from the

decreased wave function overlap due to the spatial separation of the charge carriers, which makes type II nanocrystals behave as indirect semiconductors. Therefore, our results can be well explained by the formation of a type-II core/shell structure. With increasing shell thickness, the distinctive absorption peak at the band edge vanishes.

5.2.2.2 Photoluminescence

It has not been possible to determine the photoluminescence of pure ZnTe nanocrystals. We found that the ligand/oleylamine itself also shows photoluminescence with a broad emission from 440 nm to 480 nm, although its QY is extremely low (<0.1%). ZnTe nanocrystals should show emission between 400 nm and 500 nm according to the literature.^[167] However, no enhanced signal was observed for ZnTe nanocrystals in comparison to the pure oleylamine. Therefore, we assume that the pure ZnTe cores do not show photoluminescence. The PL spectra of the type-II core/shell structures are shown in figure 5.9.

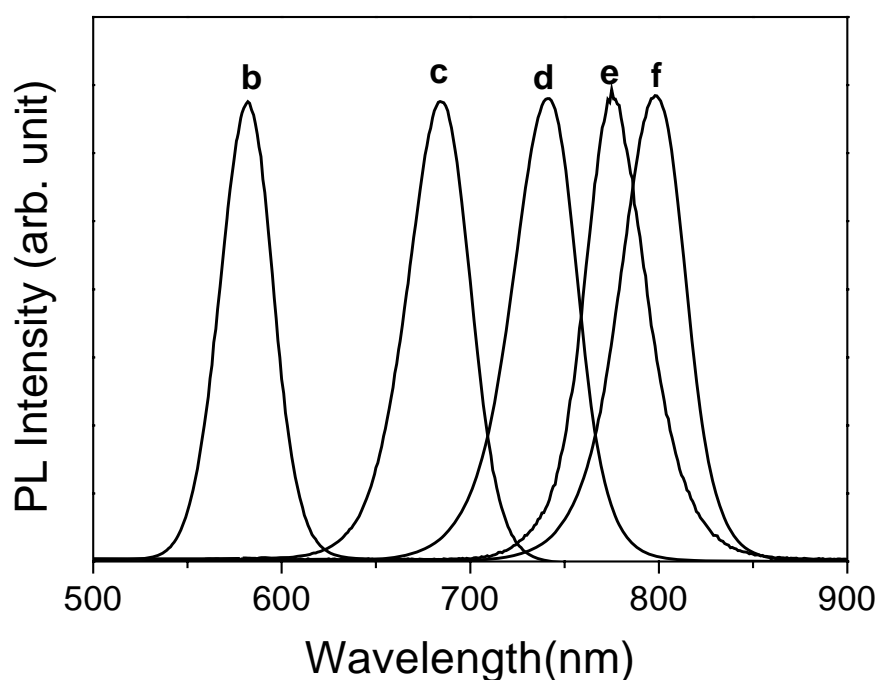


Figure 5.9 Normalized room temperature photoluminescence spectra of different ZnTe/CdSe core/shell nanocrystals. Spectra b) to f) were taken from the same solutions as the corresponding absorption spectra in figure 5.8.

It has been reported^[36] that the emission of type-II core/shell nanocrystals mainly originates from the radiative recombination of electron-hole pairs across the core-shell interface. This is demonstrated by the PL spectra in figure 5.9, where

emission from ZnTe/CdSe nanocrystals is observed at wavelengths longer than the band gap emission of either ZnTe or CdSe. An emission span from the visible to the near-infrared (580 nm-800 nm; Figure 5.9 (b-f)) was covered by successively increasing the shell thickness of CdSe on identical ZnTe cores (diameter: 4.5 nm). We found that the Stokes-shifts between the emission peaks (Figure 5.9 (b-f)) and absorption onsets (Figure 5.8 (b-f)) were about 10-20 nm. Therefore, the PL emission is attributed to an excitonic transition involving the relaxed CdSe electron (conduction band) and ZnTe hole states (valence band), and its wavelength can be effectively tuned by changing the thickness of the shell. In addition, if we change the size of the core, this will result in a different band gap of the core.

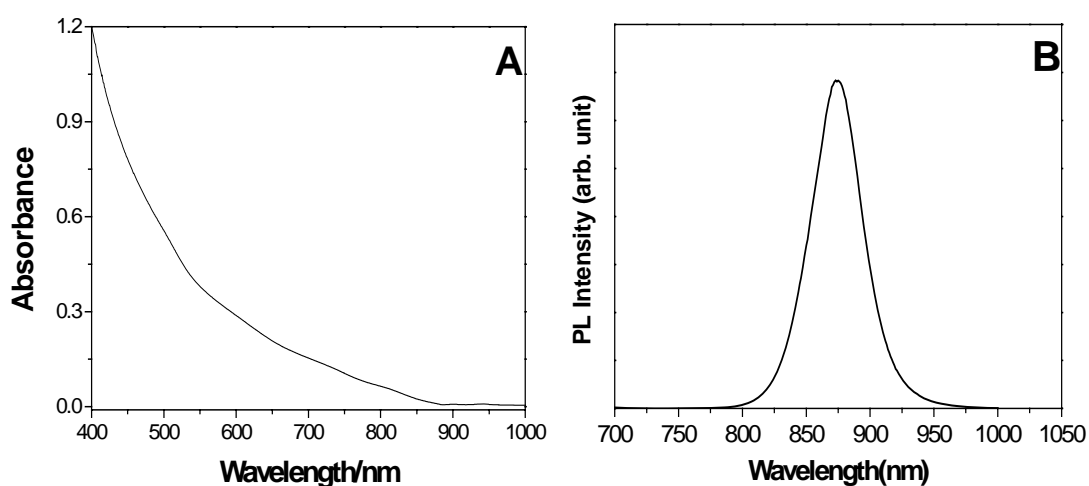


Figure 5.10 Absorption and photoluminescence spectra of ZnTe/CdSe core/shell nanocrystals with 3.6 nm radius and 1.8 nm shell thickness (1.5 MLs).

Figure 5.10 presents the absorption (A) and photoluminescence spectra (B) of ZnTe/CdSe core/shell particles with core size and shell thickness of 3.6 nm radius and 1.8 nm, respectively. For comparison, here we changed the size of the core compared to the samples shown in figure 5.9. The thickness of the shell is 3 monolayers, which corresponds to the spectra shown in figure 5.8e. As a result of the increased core size, these core/shell particles show an emission at about 880 nm. As seen in figures 5.9e and 5.10, the emission of type-II core/shell nanocrystals is also controlled by changing the size of the core. From these results, we conclude that the core size and the thickness of the shell both control the effective band gap through quantum confinement effects in type-II core/shell nanocrystals, whose emission can be tuned

by “playing” with these two variables.

The PL quantum yields of the type-II core/shell nanocrystals and their emission bandwidths (FWHM: full width at half maximum) have also been investigated as shown in figure 5.11. The corresponding values were determined from the same solutions used to measure the emission spectra. It was found that for different runs – starting with different batches of ZnTe cores – the absolute values of the QY were subject to fluctuations of up to a factor of 2-3. Referring to the data from figure 5.11, we found that compared to the plain cores, the PL QY of core/shell nanocrystals is substantially enhanced from the initial value of nearly zero (ZnTe) to 12% after growth of a 0.5 ML CdSe shell onto the cores. At best it can reach up to 28% for a shell thickness of 1.5 ML CdSe, although a maximum QY of 10-20% has been obtained typically. At a shell thickness of 4 monolayers the PL QY drops below 3% and is almost completely gone for 7 MLs. These experimental results confirm the observation that the PL QY of type-II core/shell particles strongly depends on the thickness of the shell. This is a remarkable difference to type-I core/shell nanocrystals which still show a high PL QY at a shell thickness of 7 MLs.

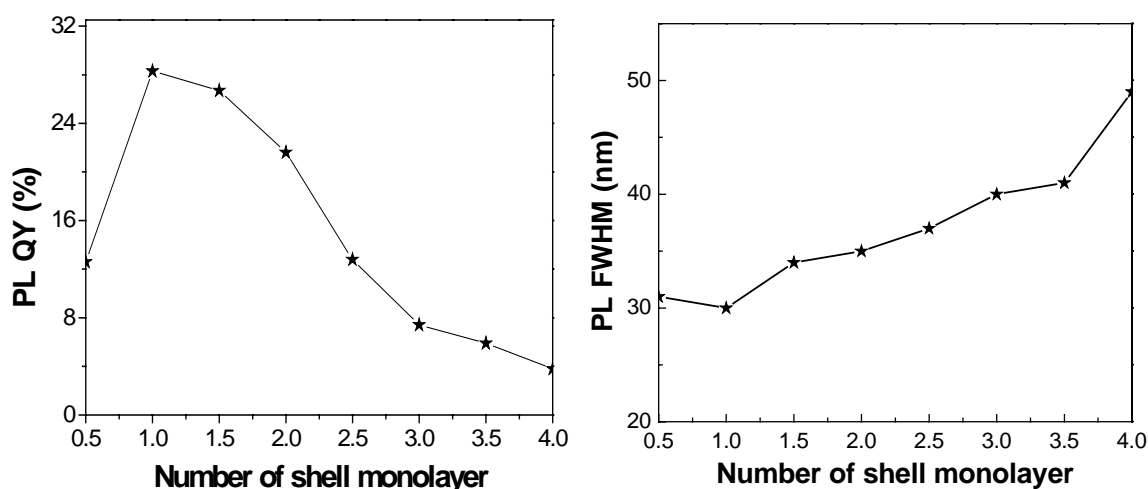


Figure 5.11 The full width at half maximum (FWHM) and PL QY of ZnTe/CdSe core/shell nanocrystals versus the number of CdSe shell monolayers.

Due to the narrow particle size distribution, the emission bandwidths (FWHM) of ZnTe/CdSe core/shell nanocrystals almost keep constant (about 30-50 nm) with increasing shell thickness, although the PL peak shifts from 580 nm to 880 nm. It should be noted that core/shell nanocrystals with larger cores show extremely low QYs. For example, the QY of the core/shell nanocrystals shown in figure 5.10 is only

about 0.5% after the growth of 3 CdSe monolayers. Even if the thickness of the shell is 1-2 monolayers, the QY of these nanocrystals is not over 1%.

Besides ZnTe/CdSe also ZnTe/CdS and ZnTe/CdTe core/shell nanocrystals were investigated during this thesis. Figure 5.12 presents the evolution of absorption and PL spectra during the growth of CdS and CdTe shells onto ZnTe cores. A large red shift was observed in the spectra with the growth of the shell. At the same time, the first absorbance peak almost disappears with increasing shell thickness. Similar results have been observed for ZnTe/CdSe (Figure 5.8). The emission of ZnTe/CdS and ZnTe/CdTe core/shell nanocrystals could be tuned from 580 nm to 800 nm, as seen in figures 5.12 (ii) and (iv).

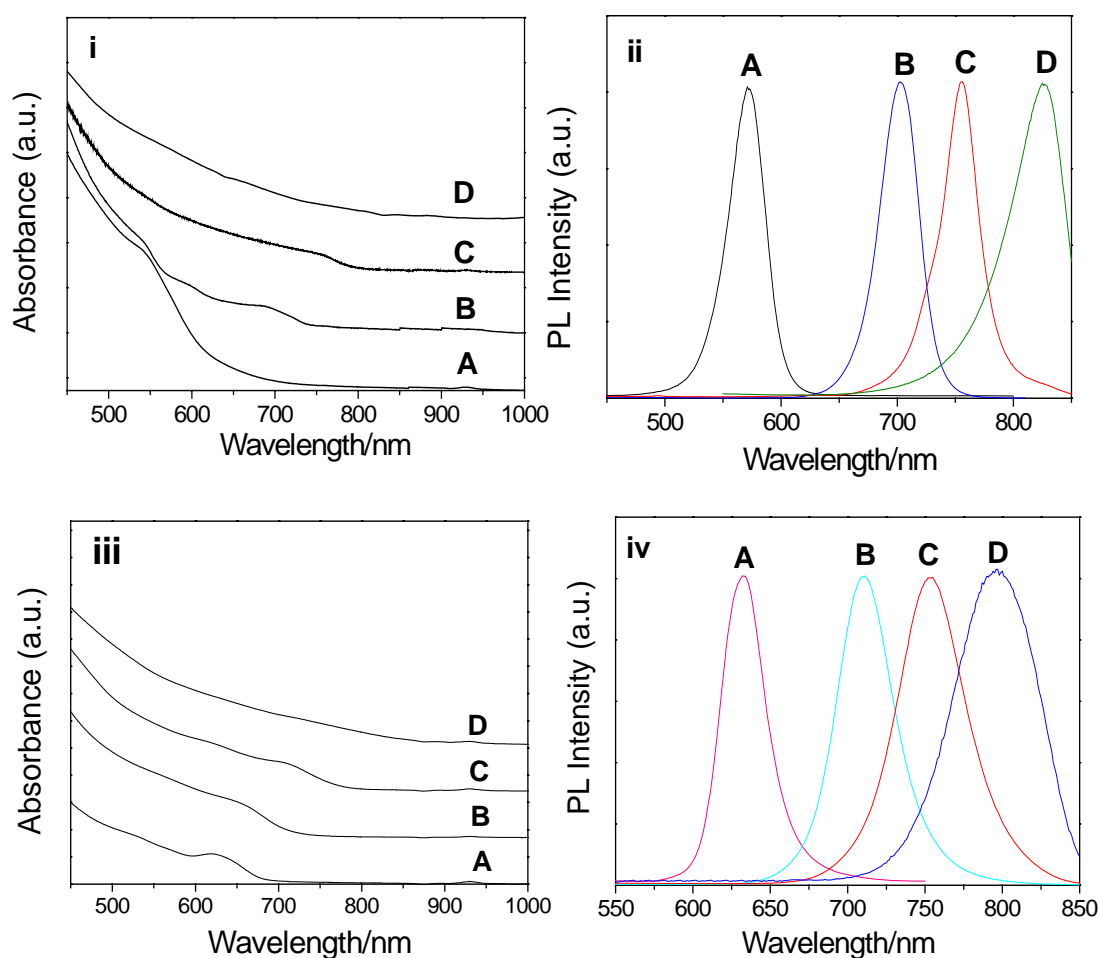


Figure 5.12 Evolution of absorption and PL spectra during growth of CdS ((i) and (ii)) and CdTe((iii) and (iv)) shells on ZnTe cores, respectively. The spectra were obtained for aliquots extracted 2 min after the injections of the CdS or CdTe stock solution. The core was 2.3 nm in radius, the shell thickness was A) 0.5, B) 1.0, C) 2.0, D) 4.0 monolayers

Figure 5.13 shows the PL quantum yields and FWHM of ZnTe/CdS and ZnTe/CdTe core/shell nanocrystals, respectively. We found that their PL QYs can at best reach up to ~15 % after 1.5 monolayer shells, although only 1-5% QY can be obtained in a typical reaction. With increasing thickness of the shell, we also in this case observed that type-II core/shell nanocrystals show extremely low QYs after the growth of more than 3 monolayers. At the same time, the FWHM of ZnTe/CdTe is much broader than that of the ZnTe/CdSe core/shell nanocrystals. In case of the ZnTe/CdS core/shell nanocrystals, the FWHM is almost the same as that of ZnTe/CdSe nanocrystals. These findings are in agreement with the size distributions of nanocrystals as shown in figure 5.4.

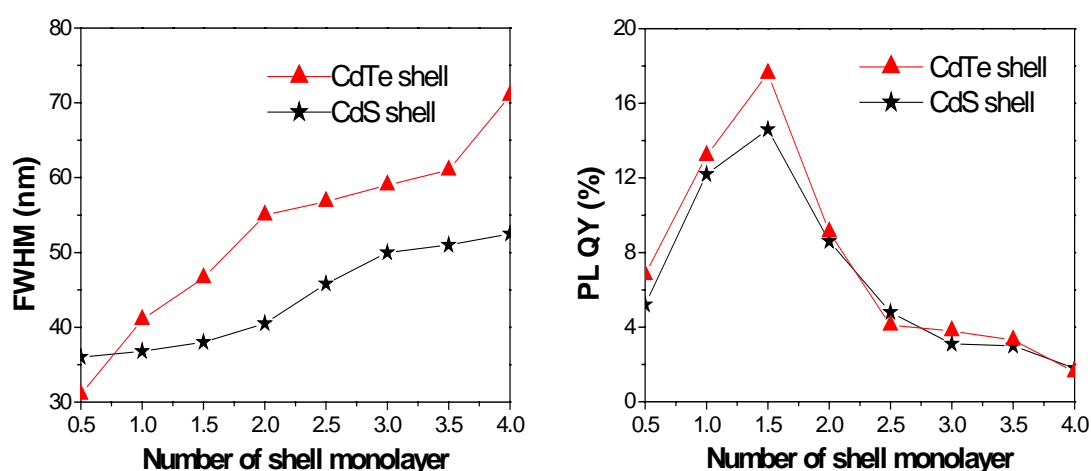


Figure 5.13 The evolution of full width at half FWHM (left) and PL QY (right) of ZnTe/CdS and ZnTe/CdTe core/shell nanocrystals versus the number of CdS and CdTe shell monolayers, respectively.

The emission of the inverse CdSe/ZnTe core/shell nanocrystals also can be tuned from the visible to the near infrared region. When the core/shell structures were inverted (CdS, CdTe and CdSe served as cores and were overcoated by ZnTe), the corresponding core/shell nanocrystals showed extremely low PL QYs ($< 0.2\%$), which is consistent with recent findings reported in the literature.^[37] This observation suggests that holes on the surface of nanocrystals might be more easily captured than electrons.

5.3 Conclusion

In summary, colloidal type-II core/shell nanocrystals have been synthesized using a one-pot process by alternate addition of precursors (CdO, S, Se or Te) into the crude reaction solution of mono-disperse ZnTe cores. The core/shell particles showed a narrow size distribution, and PL QYs of up to 30 % have been obtained. In this context the importance of a thin shell has been clearly demonstrated. The emission of the particles can be widely tuned from the visible into the near-infrared region (580 nm- 900 nm) by increasing the thickness of the shell and by variation of the size ratio of core and shell. In comparison to other NIR emitters like organic dye molecules, the PL QYs of the type-II core/shell particles can reach higher values.^[174] On the other hand, due to the spatial separation of the charge carriers in ZnTe/CdSe nanocrystals, these particles may lend themselves to applications in photoconducting or photovoltaic devices. Furthermore, the synthetic approach presented here opens a versatile route to other type-II core/shell nanocrystals.

5.4 Preparation methods

A: Stock solution for shell growth

For shell growth using the SILAR method we used precursor solutions containing only metal oxides (CdO), elemental sulfur, and selenium and tellurium. The cadmium precursor solutions (0.1 M) were prepared by dissolving CdO (0.3204 g) in OA (6.18 g) and ODE (18.0 ml) at 240 °C. The sulfur precursor solution (0.1 M) was prepared by dissolving sulfur in ODE at 180 °C. The selenium and tellurium precursors solution (0.1 M) were prepared by dissolving Se and Te in TOP, respectively. All solutions were freshly prepared under N or Ar-atmosphere. The Cd solution was kept at about 80 °C while the sulfur, selenium and tellurium injection solution were kept at room temperature.

B: Synthesis of ZnTe core and ZnTe/CdSe, ZnTe/CdS and ZnTe/CdTe core/shell nanocrystals

Synthesis of ZnTe cores with ODA caps and preparation of core/shell nanocrystals: For a typical reaction, ODA (1 g) and ODE (3 g) were loaded into a reaction flask. The solution was heated to 280 °C under argon flow. A solution of tellurium and diethylzinc (1ml, molar ratio Te: Zn=1:1) in TOP was injected quickly

into the reaction flask. After the injection, the reaction temperature was set to 270 °C to grow nanocrystals. Finally, the solution was cooled down to room temperature and kept under argon. For growth of the CdSe shell, assuming that the reaction leading to the ZnTe cores was quantitative, the amount of Cd and Se precursors to be added for shell growth can be accurately calculated from the respective volumes of concentric spherical shells with a thickness of one hypothetical monolayer (about 0.305 nm). It was concluded that a period of 10 min between each layer was sufficient for the reactions to be completed, because the UV-Vis- and PL-spectra showed no further changes after this time period. After the reaction, the solution was cooled down to room temperature. For purification 5 ml of hexane were added and the un-reacted compounds and by-products were removed by successive methanol extraction until the methanol phase was clear. CdS and CdTe shells were grown under similar experimental conditions.

6. Synthesis of various CdSe architectures

6.1 Introduction

Semiconductor nanocrystals have emerged as an important class of materials because not only their sizes but also because their shapes play a crucial role in determining their electronic and optical properties.^[12, 175-178] In particular, non-spherical semiconductor nanocrystals are considered as ideal model systems for studying anisotropic optoelectronic effects such as polarized emission and highly directional charge transport.^[43] Potential technical applications include photovoltaic cells,^[40, 136] light-emitting-diodes,^[179, 180] logic gates,^[181, 182] and transistors.^[181, 182] Therefore, during the past few years much effort has been devoted to controlling the size and shape of these materials by various approaches. The vapor-liquid-solid (VLS) growth mechanism and its analogues have been successfully applied to create one-dimensional nanomaterials such as nanorods or nanowires in a liquid medium by the use of nanosized liquid or solid seeds. In this method, which was pioneered by the group of Lieber,^[52, 53, 183-186] the anisotropic crystal growth is promoted by using metal nanoparticles as a catalyst. The template-directed synthesis presents a straightforward route to anisotropic nanostructures. In this approach, the template simply serves as a scaffold in which different materials are generated in situ and shaped into a nanostructure with morphology complementary to that of the template.^[45, 49] The effective monomer model is the basis of another way of controlling shape evolution of semiconductor nanocrystals.^[88, 111, 113] Recently,^[187] a new theory of the oriented attachment mechanism has been proposed to explain the formation of complex nanostructures in which nanocrystals can join together with perfect crystallographic alignment. This mechanism has been successfully utilized for the synthesis of CdTe and ZnSe nanowires.

Following the growth mechanisms described above, syntheses in the aqueous or organic phase are used to prepare colloidal nanocrystals. In fact, the advantages of each strategy have to be carefully weighted against the drawbacks. For example, coprecipitation in an aqueous phase or hydrothermal/solvothermal synthesis can be successfully used to produce semiconductor nanocrystals with different shapes using reverse micelles as templates or surfactant controlled growth in a hot solution.^[188-191] The advantage of the latter method over other approaches is the simple manipulation and processing chemistry of ligand-coated nanocrystals. In comparison to other types

of nanocrystals such as CdS^[80] or CdTe,^[192] the shape evolution of colloidal CdSe nanocrystals has been widely studied. For example, the groups of Peng^[55, 111, 112] and Alivisatos^[54] have successfully synthesized CdSe nanocrystals with various morphologies, such as rods, arrows, pine trees, teardrops, wires, tetrapods and other hyper-branched structures.^[54, 193, 194] However, different morphologies so far could be only obtained in coordinating solvents (Trioctylphosphine oxide (TOPO) and Hexylphosphonic acid (HPA)) at high temperature. Therefore, there is still room for improvement by addressing issues such as the high synthetic cost (expensive alkylphosphonic acid and TOPO are used in the synthesis of CdSe nanorods), and the low yields for e.g. tetrapod nanocrystals.^[54]

During this thesis, “crystal phase control” was employed to grow anisotropic semiconductor nanocrystals with precise shape control. In previous approaches, in which anisotropic particles were grown from one material, the nucleation and the anisotropic crystal growth stages were not clearly separated, and thus the preferable crystal phase was difficult to control.^[114] Here, the “crystal phase control” approach was used to grow various CdSe architectures with a high yield (>90%) by using zinc blende ZnTe, ZnSe and ZnS nanocrystals as seeds. We found that wurtzite arms can be projected from a zinc blende core by controlling the injection method and reaction temperature. Importantly, some novel structures were obtained in this work for the first time. To the best of our knowledge, the use of pure II-VI nanocrystal seeds with zinc blende structure to aid the growth of CdSe architectures has not previously been demonstrated.

6.2 Results and discussion

In this work, the influence of the reaction conditions on the architectures of CdSe nanocrystals was investigated by changing three fundamental parameters: different materials with zinc blende structure, reaction temperature and injection methods. In previous studies, the influence of other synthetic conditions on the shape of CdSe nanoparticles^[55, 112, 114] has been reported. For example the ratio of the surfactants (HPA/TOPO), the volume of the initial injection solution and the time dependence of the monomer concentration were investigated.^[112] The present investigation intends to control the growth process of shape-controlled CdSe nanocrystals. We used different zinc blende materials as seeds to grow CdSe

architectures and varied the injection methods and temperature. The initial reaction volume was kept constant in all these experiments (2ml OAm, 2 ml ODE and 0.04 mmol zinc blende seeds). No size/shape sorting was performed for all the products obtained from the syntheses described below.

6.2.1 Spherical core/shell nanocrystals

6.2.1.1 Structural characterization

As has been shown in chapter 5, spherical core/shell nanocrystals (e.g. ZnTe/CdSe) can be obtained by using zinc blende ZnTe cores at 240°C. Other spherical core/shell nanocrystals such as ZnSe/CdSe can also be produced at 240°C. In the present context “spherical” means that in the end, after growth of many layers of CdSe shells, almost spherical core/shell particles are obtained. At lower coverage,

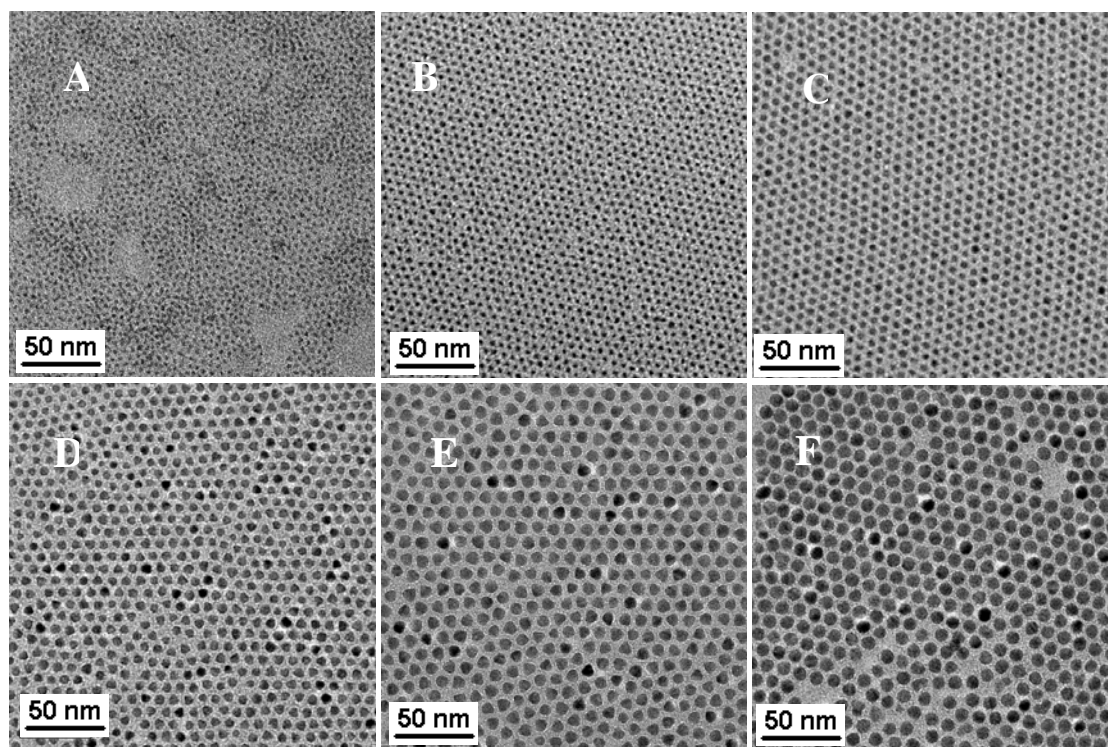


Figure 6.1 Wide-field TEM images of ZnSe core nanocrystals and corresponding ZnSe/CdSe core/shell nanocrystals with different shell thicknesses grown on the identical cores; (A): TEM image of 2.8 nm ZnSe core nanocrystals; (B)-(F) TEM images of ZnSe/CdSe core/shell nanocrystals with 1, 2, 4, 6 and 8 ML of CdSe, respectively (thickness of 1 ML CdSe = 0.7 nm in diameter)

however, the particle shape deviates from spherical. Figure 6.1 shows TEM images of 2.8 nm ZnSe core nanocrystals and five representative images of ZnSe/CdSe

core/shell nanocrystals with 1, 2, 4, 6 and 8 monolayers (MLs) of CdSe shells grown from the same batch of 2.8 nm ZnSe cores.^[195] The sizes of the core/shell nanocrystals shown in figure 6.1 increased with the addition of the CdSe precursors, which gives strong evidence for epitaxial growth of CdSe onto the ZnSe core and excludes independent homogeneous nucleation of CdSe. These results indicate that a high reaction temperature in the end is in favor of forming more spherical core/shell structure, which is consistent with the facts reported in chapter 5 and discussed above.

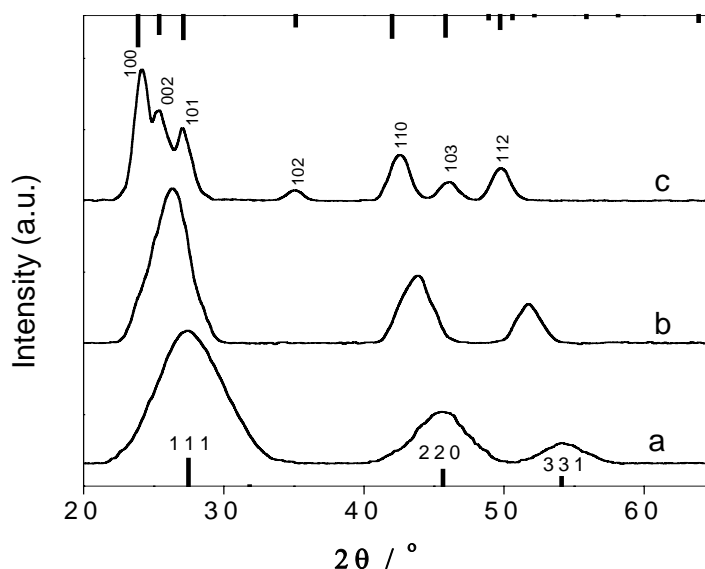


Figure 6.2 Powder XRD patterns of the plain ZnSe core nanocrystals with a diameter of 2.8 nm (a), and ZnSe/CdSe core/shell nanocrystals with CdSe shell thicknesses of 2 ML (b), and 6 ML (c). The line XRD spectra correspond to bulk zinc blende ZnSe (bottom) and bulk wurtzite CdSe (top), respectively. After reference [195]

In order to identify the crystal structure, powder X-ray diffraction (*p*-XRD) patterns for the ZnSe cores and for ZnSe/CdSe core/shell nanocrystals with increasing shell thickness are presented in figure 6.2. As reported in the literature,^[28] the ZnSe XRD pattern consists of the characteristic peaks of zinc blende ZnSe, which are broadened due to the finite crystal size. The *p*-XRD patterns of the ZnSe/CdSe core/shell nanocrystals shifted from a zinc blende ZnSe-like to a zinc blende CdSe-like, and further to a wurtzite CdSe-like pattern upon increase of the CdSe shell thickness. When a thin CdSe shell (< 4 ML) is grown onto the cubic ZnSe template, the general pattern of the cubic lattice is maintained in the core/shell structures, but the diffraction peaks shift to smaller angles consistent with the larger lattice constant for CdSe compared with ZnSe. In addition, the diffraction peaks get narrower. This

narrowing indicates that the crystalline domain is larger for the core/shell structure providing direct evidence for the epitaxial growth mode of the shell.^[147, 196] CdSe under these growth conditions preferentially forms the wurtzite (hexagonal) structure with increasing shell thickness. The diffraction pattern of the core/shell structure with 6 ML CdSe shell is almost the same as that of wurtzite CdSe nanocrystals of the same size. The dominance of the CdSe pattern in the XRD (Figure 6.2 (top)) for the thick shell nanocrystals is not too surprising given that the CdSe: ZnSe ratio is ~ 15:1 for these nanocrystals.

If ZnS nanocrystals were used as cores instead of ZnSe or ZnTe under the same experimental conditions, ZnS/CdSe spherical core/shell nanocrystals (not shown here) can also be obtained. It is found that the crystal structure changed from zinc blende to wurtzite with the growth of CdSe shells, which has been observed in all the comparable core/shell systems including ZnS/CdSe, ZnSe/CdSe and ZnTe/CdSe. Importantly, all the experiments indicate that high temperature is favorable for forming a spherical core/shell structure.

6.2.1.2 Optical properties

The optical properties of pure ZnTe seeds have been discussed in chapter 5. When ZnSe and ZnS cores are overgrown by CdSe, this results in a reverse type-I structure. Therefore, the optical properties of these nanocrystals mainly depend on the shape/size of the particles. Figure 6.3 shows the absorption (A) and photoluminescence (B) spectra of spherical ZnSe/CdSe core/shell structures.^[195] With increase of the shell thickness from 0.1 to 6 MLs, the corresponding PL peaks shift from 418 nm to 674 nm. The PL emission from these core/shell nanocrystals spans the whole visible spectrum from violet to red, which corresponds very much to pure CdSe nanocrystals.^[16] With growing CdSe shell, the quantum yields of the core/shell nanocrystals increase steadily from ~40% for the original core particles, reaching the highest value of ~85% after one full monolayer is formed and keeping this value until 3 MLs. If a shell with more than 3 ML is formed, the QY decreases gradually (the QY for 6 ML is ~25%). The lower QYs of the thicker shell ZnSe/CdSe nanocrystals may originate from the weaker quantum confinement effect due to the larger particle size. When the size of spherical ZnSe/CdSe core/shell nanocrystals is more than 10 nm, the QYs are below 1%.

For ZnS/CdSe core/shell nanocrystals, the spectra are similar to that of spherical ZnSe/CdSe core/shell nanocrystals because the spectra are generated from the CdSe shell. Therefore, they are not shown here.

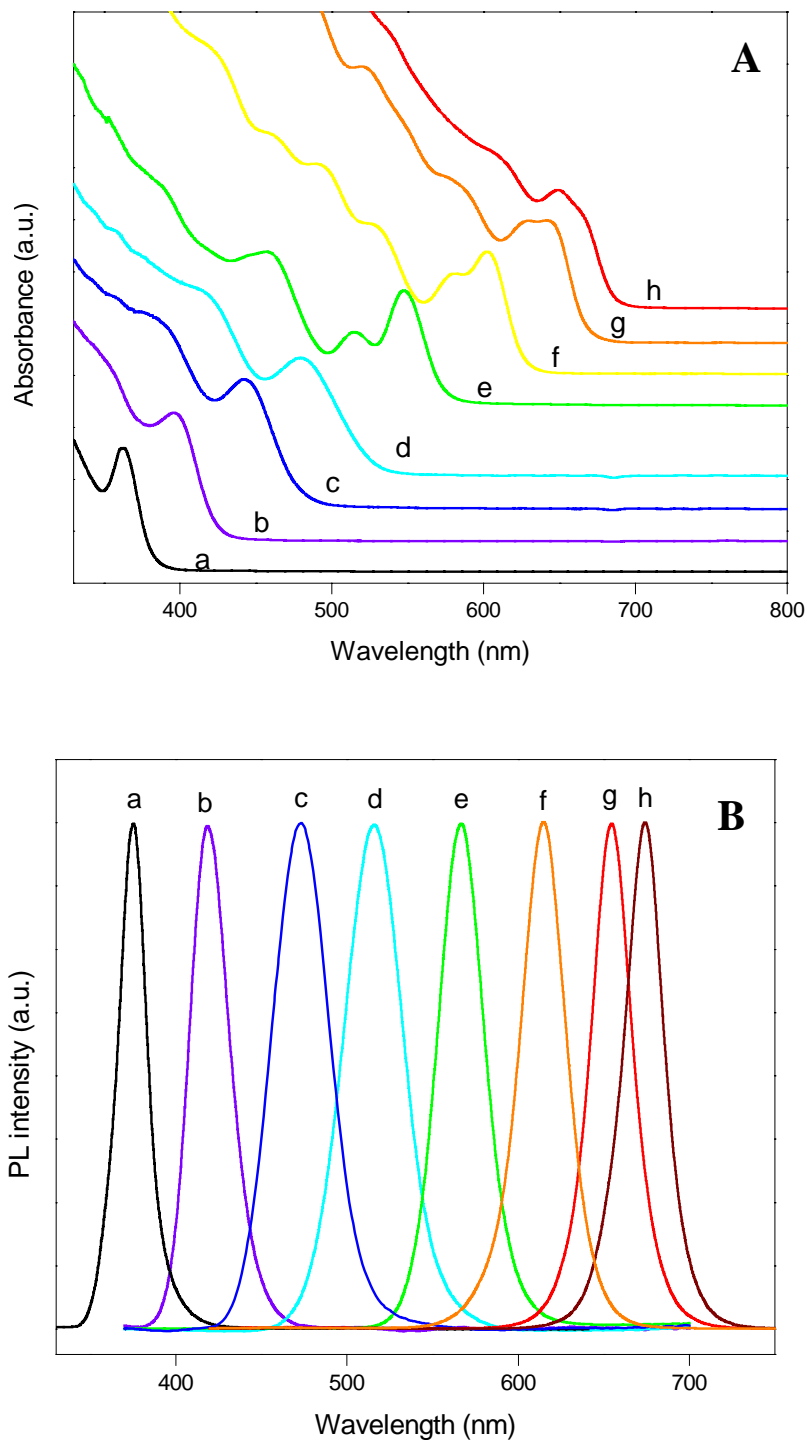


Figure 6.3 Absorption (A), and corresponding PL (B) spectra of ZnSe core nanocrystals (a) and ZnSe/CdSe core/shell nanocrystals with different number of monolayers of CdSe shell: **b**, 0.1; **c**, 0.2; **d**, 0.5; **e**, 1; **f**, 2; **g**, 4; **h**, 6. After reference [195]

6.2.2 Pyramidal nanocrystals

As described before, predominantly spherical core/shell structures were obtained during growth of CdSe architectures at 240 °C by using zinc blende seeds (ZnTe, ZnSe and ZnS). However, at 210°C it is found that pyramidal CdSe nanocrystals are formed after growth of 6 ML CdSe shells (Figure 6.4 C). For further growth of the CdSe shell by the SILAR method, the reaction temperature was increased to 230 °C. The shape of the pyramidal nanocrystals is kept with the addition of the precursors. Figure 6.4 presents the evolution of CdSe nanocrystals grown onto

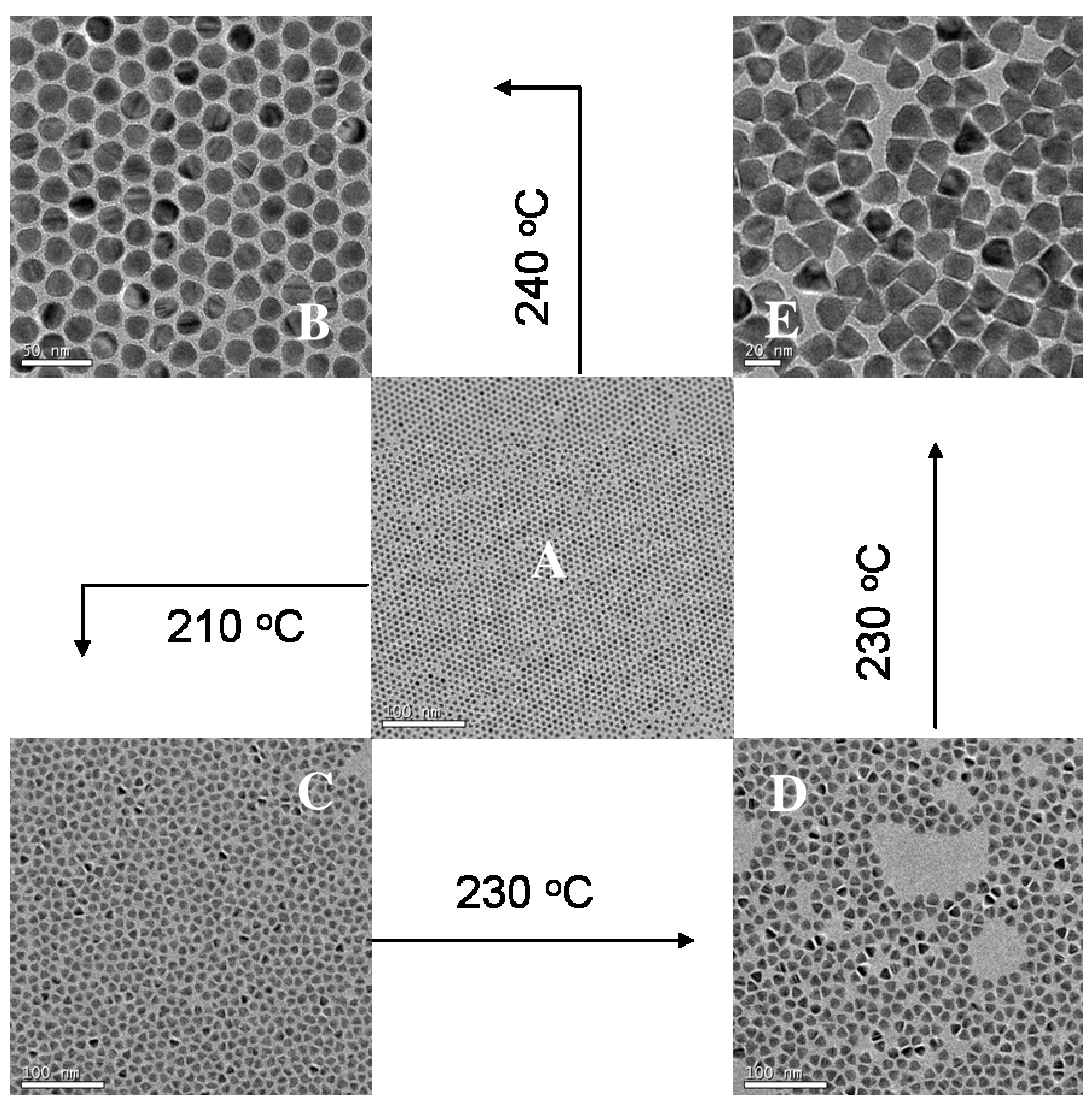


Figure 6.4 Shape evolution of ZnSe/CdSe nanocrystals under different growth conditions: From spherical ZnSe/CdSe nanocrystals with 2ML CdSe (A) to spherical ZnSe/CdSe nanocrystals with 20 ML CdSe shells at 240 °C (B), or to pyramidal nanocrystals with 6 ML CdSe shells at 210°C (C). (D) and (E)(scale is 20 nm): Pyramidal ZnSe/CdSe nanocrystals synthesized at 230 °C with 10 ML and 20 ML CdSe shells, respectively.

ZnSe seeds at different temperatures. On one hand, at 240°C the growth of CdSe shells results in spherical core/shell structures after a nominal shell thickness of 20 MLs is grown onto the ZnSe core (Figure 6.4 B). On the other hand, pyramidal nanocrystals are formed after about 6-8 ML at 210°C. The shape of the pyramidal nanocrystals is kept when the temperature is raised to 230°C and the injection solutions are added successively as shown in figures 6.4 (C-D). After further growth the shape deviates from pyramidal (Figure 6.4 E). Therefore, we assume that at high temperature the growth of isotropic nanocrystals is favored.

The images (Figure 6.4) show that the average size of nanocrystals can be tuned from 7 nm to 25 nm length of the pyramidal sides. Of course, the crystal structure of the pyramidal nanocrystals is wurtzite after the growth of 6 MLs, in analogy to that of the spherical core/shell structure described before. More detailed information will be shown in the next part. These results indicate that the temperature is crucial for the shape of nanocrystals. In case of ZnS seeds, similar results have been obtained under the same experimental conditions. (Not shown here)

Considering the optical properties of pyramidal ZnSe/CdSe or ZnS/CdSe core/shell nanocrystals, the absorption and photoluminescence spectra are almost the same as for spherical ZnSe/CdSe nanocrystals shown in figure 6.3.

6.2.3 Tetrapod nanocrystals

Recently, tetrapod nanocrystals have been observed for various II–VI semiconductors.^[114, 192, 197-203] A very prominent example are CdTe tetrapod nanocrystals.^[114] Tetrapodal CdSe nanocrystals were first reported by the group of Alivisatos.^[54] They employed crystal-phase control by utilizing zinc blend-wurtzite polytypism which occurs in these materials. Polytypism is a type of polymorphism where different polymorphs exist in different domains of the same crystal. It also is a common phenomenon in group II–VI and III–V semiconductors.^[149] The most basic branched polytypic crystal is a tetrapod that consists of a tetrahedral zinc blende core and four wurtzite arms. A tetrapod is formed if four wurtzite-phase arms grow out of four equivalent (111) surfaces of a zinc blende nanocrystal core. However, in the syntheses mentioned before, a low yield of tetrapod nanocrystals was obtained by an organometallic thermolysis route.^[54] A key parameter for achieving tetrapod growth is the energy difference between the wurtzite and the zinc blende structures. Therefore,

the growth of tetrapod nanocrystals is determined by the temperature range in which the formation of one structure is preferred during nucleation, and the formation of another structure is favored during growth. Special surfactants are used to change the kinetics and relative stability of the corresponding crystal faces. Organic stabilizers such as phosphonic acid are used to alter the crossover threshold, with higher phosphonic acid concentration favoring branching at relatively low concentrations of monomer and hence low growth rate. However, phase control and phase switching of CdSe is very difficult to achieve in a one-pot reaction, because of the small energy difference between the two phases (zinc blende and wurtzite).^[149]

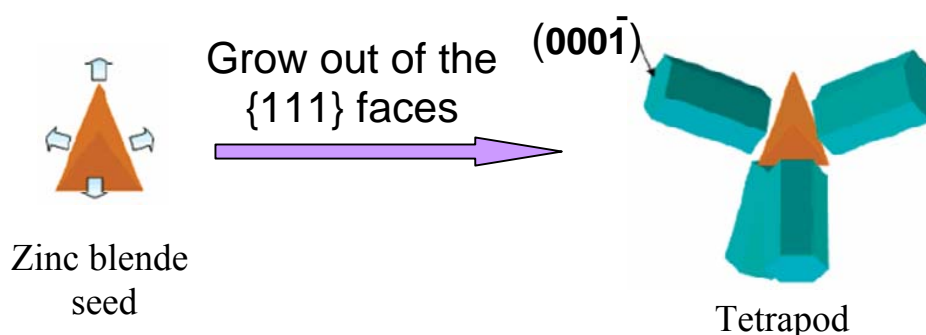


Figure 6.5 Schematic diagram of forming tetrapod shaped heterostructure nanocrystals.

In the following, we report the synthesis of CdSe tetrapods using a two step approach. As the zinc blende core, ZnTe nanocrystals were prepared according to the procedure described in chapter 5. When the ZnTe nanocrystals are overcoated with CdSe by alternate injections of Cd- and Se-precursors at a temperature of 240°C, core/shell structures with nearly spherical shape are formed with shell thicknesses up to 7 monolayers (MLs).^[204] When CdSe is grown onto the ZnTe template at $T = 215^\circ\text{C}$ in the presence of oleylamine ligands, a continuous transition from “spherical” ZnTe/CdSe core/shell particles over pyramidal to tetrapod-shaped heterostructures is observed. Figure 6.5 shows a schematic diagram of heterostructure formation. The synthetic route is as follows: ZnTe seeds with zinc blende structure were first formed in ODA/oleylamine as described in chapter 5. Then, the ZnTe nanocrystals were loaded into an ODE and oleylamine mixture, and heated to 215°C for the growth of CdSe arms by alternate addition of Cd and Se precursors (see Preparation methods).

6.2.3.1 Structural characterization

Figure 6.6 (B-F) display typical TEM images during different stages of the growth of the branched heterostructures. Figure 6.6 B shows spherical ZnTe/CdSe

core/shell nanocrystals with a nominal shell thickness of 2 MLs. Further injection of Cd- and Se-precursor solutions, whose amounts were adjusted to form a third ML, leads to particles with pyramidal shape. It appears that with increasing shell thickness the initial epitaxial shell growth is hindered for some lattice planes favoring the anisotropic crystal growth. When the spherical core/shell nanocrystals start to grow pyramid-like, the shape of the nanocrystals is maintained until the tetrapod shaped nanocrystals have reached the desired arm lengths (Figure 6.6 C-F). The TEM results clearly demonstrate that tetra-pods are obtained in which the length of the arms can be well controlled. Typically, the four arms of the tetrapods are equal in length within a few percent deviation with arm diameters around 6-7 nm, which remain almost constant during the arm growth. For several repeated syntheses of these CdSe tetrapod nanocrystals, it was observed that most of the anisotropic growth took place after the formation of the 3rd or 4th monolayer. In general, the length of the arms can reach up to 50 nm by controlling the number of injections. When the length of the arms is more than 50 nm, it is difficult to control the yield and the shape of the nanocrystals.

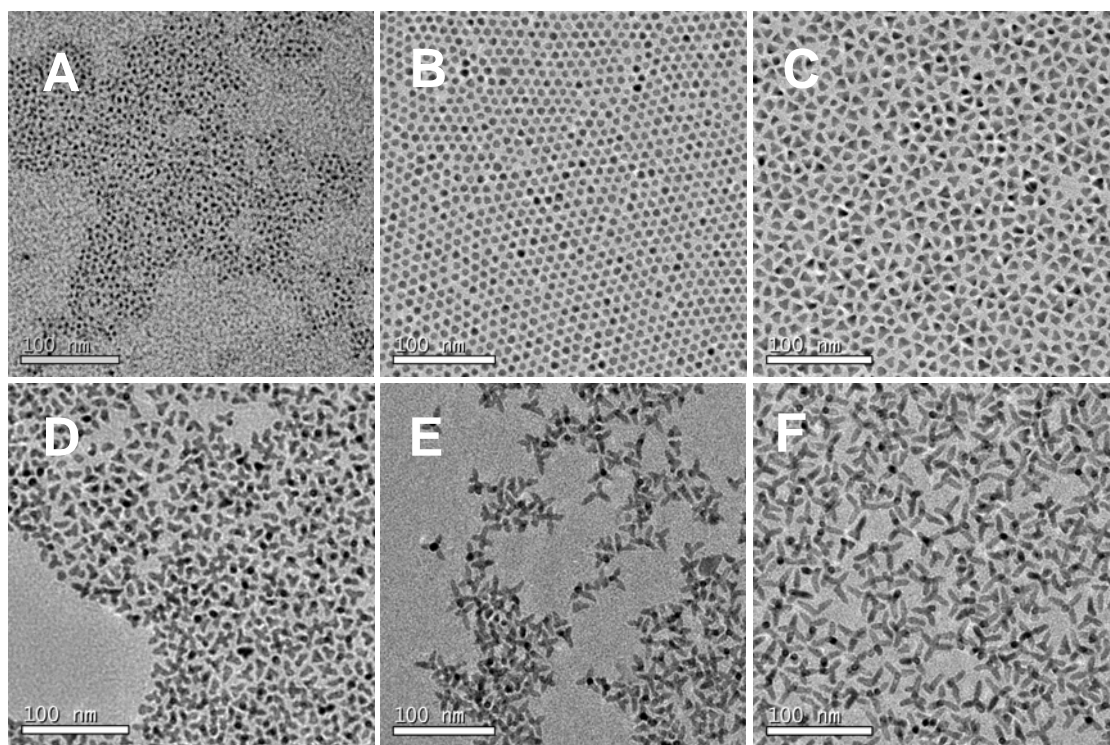


Figure 6.6 TEM images of ZnTe cores (A) and corresponding ZnTe/CdSe heterostructure nanocrystals portraying the transition from isotropic core/shell (B), over pyramidal (C), to tetrapod-shaped heterostructures with different arm lengths (D-F). Scale bar=100 nm.

For a more detailed structural characterization of the tetrapod shaped heterostructure nanocrystals and to support the above reasoning, high-resolution transmission electron microscopy (HRTEM) was employed. Figure 6.7 (left hand side) shows a HRTEM image of a single ZnTe/CdSe tetrapod, which exhibits uniform needle-shaped arms consisting of single-crystalline CdSe. The central CdSe arm (I), which fully covers the ZnTe core, is oriented with its c-axis parallel to the electron beam exposing the (0001) plane. The other three CdSe arms (II-IV) are equally oriented with respect to the substrate and exhibit the [-331] zone. The analysis of the reciprocal lattice peaks obtained from a two-dimensional Fourier transform of the HRTEM images (see Figure 6.7; I-IV) results in the hexagonal wurtzite lattice for all four CdSe arms. To further understand this structure, a simple calculation shows that the c axis as the long axis respectively the growth direction of the tetra-pod arms lies in an angle of approximately 70° to the [-331] zone. From this it can be inferred that the ZnTe core is situated above the support film. The orientation of the tetra-pod has been verified by tilt series in imaging mode.

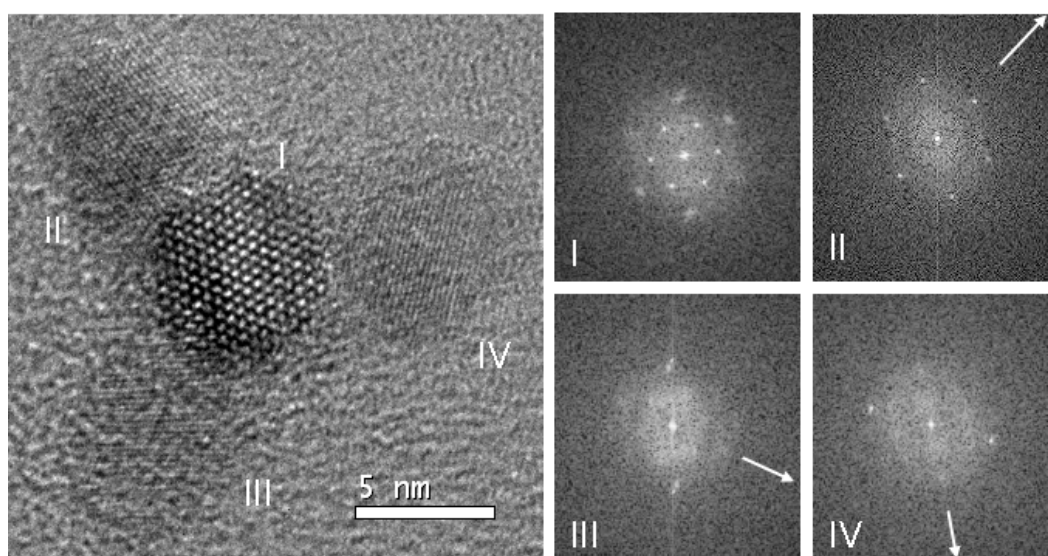


Figure 6.7 HRTEM image (left hand side) of a ZnTe/CdSe tetrapod and partial 2D FFT of the four CdSe arms (right hand side). Reciprocal lattice peaks for tetra-pod arm I are consistent with zone [001]: $(110); (-120); (-210) = 0.215 \text{ nm}$. Reciprocal lattice peaks for tetra-pod arms II-IV indicate zone [-331]: $(110) = 0.215 \text{ nm}$ (indicated by black lines in FFT) and $(103) = 0.198 \text{ nm}$.

To identify the local chemical composition of the tetrapod shaped nanocrystals, EDX was also applied. The EDX spectra shown in figure 6.8 were taken

in the centre of the particle (spot A) and at one of the branches (spot B). Spectrum A confirms the presence of Te (Zn is overlapped by Cu) in the core. The Cd and Se signals originate from the CdSe branch sitting on top of the core. Spectrum B shows a significantly reduced Te signal as expected for a pure CdSe branch where the remaining Te intensities are due to secondary x-rays. Unfortunately, we did not succeed to determine the thickness of the CdSe shell supposedly grown onto other than the {111} facets of the ZnTe core. Actually, from TEM (e.g. Figure 6.6) we only can deduce that the diameter of the central core is not larger than that of the arms. Nevertheless, all these results give strong evidence for tetrapod shaped heterostructures with a zinc blende core and wurtzite arms.

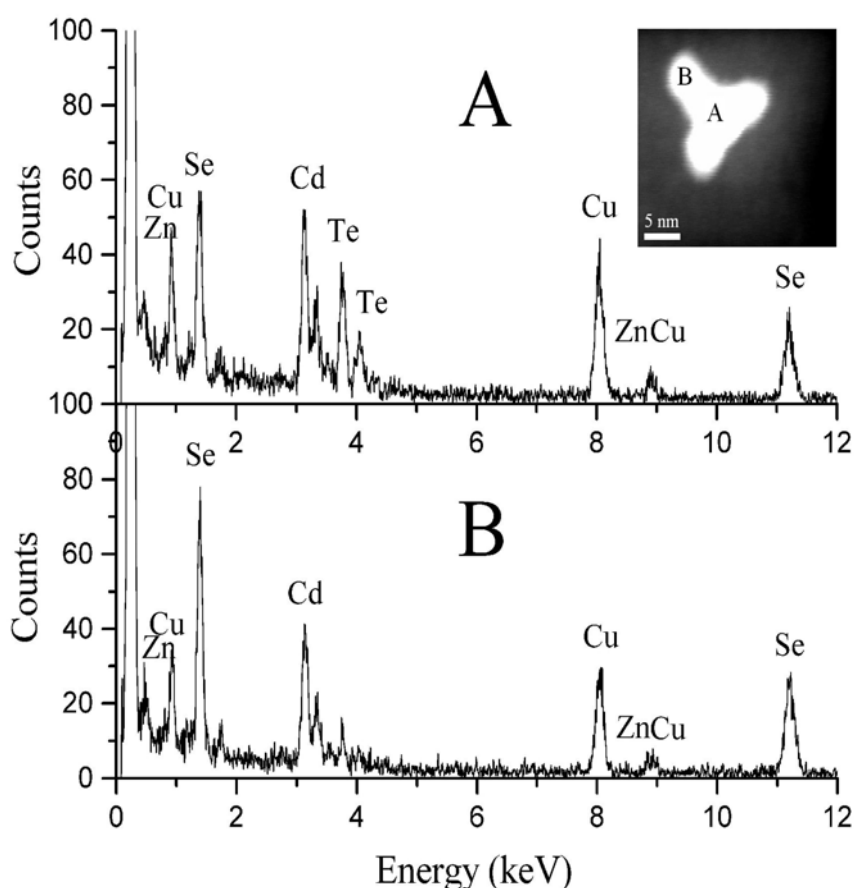


Figure 6.8 EDX data from a single ZnTe/CdSe tetrapod. The inset shows the HR-TEM image of the same tetrapod. (A): EDX spectrum from the middle CdSe tetrapod arm (A). (B): EDX spectrum from arm (B).

The tetrapod nanocrystals such as ZnTe/CdSe synthesized in this thesis show a higher degree of solubility compared with single CdSe rods of the same length and

diameter as the tetrapod arms. This behavior is in agreement with that of CdTe tetrapod nanocrystals reported in the literature. ^[114] A remarkable feature of the synthesis reported here is that the four arms of the tetrapod are equal in length within a few percent. The tetrapod shaped heterostructure nanocrystals (ZnTe/CdSe) can be obtained in yields as high as 90% without post-synthesis purification by selective precipitation. However, one pod nanocrystals sometimes can be seen. This structure might arise if the four facets of the zinc blende core are not identical due to crystal plane defects.

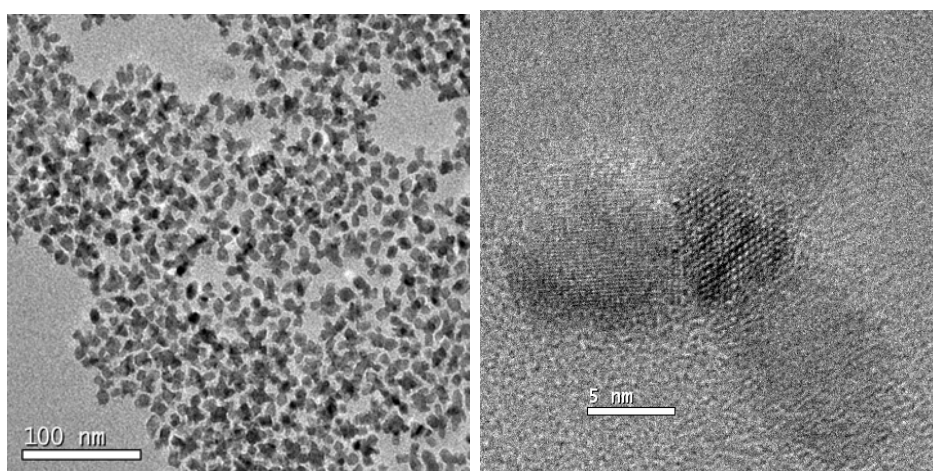


Figure 6.9 ZnTe/CdS Tetrapod nanocrystals (left). A HRTEM of a single tetrapod (right)

Besides ZnTe/CdSe we also have achieved to prepare ZnTe/CdS and ZnSe/CdSe (see chapter 6.2.3.2) tetrapod shaped nanocrystals as shown in figure 6.9, indicating that our design concept works successfully for the synthesis of different branched heterostructure nanocrystals. Structural characterization by HRTEM revealed that also in the case of ZnTe/CdS four CdS arms with a hexagonal wurtzite lattice are projected from a cubic zinc blende ZnTe core.

As already mentioned, the reaction conditions are important for the growth of the wurtzite arms. We have found that oleylamine plays a crucial role during the reaction, as it seems to increase both the growth rate in the (0001) facet and the overall growth rate during CdSe rod formation as reported similarly for HPA (hexaphosphonic acid). ^[42, 54, 112] While HPA requires the presence of another stabilizing ligand such as TOPO, oleylamine acts not only as the shape-controlling ligand but also as a stabilizing ligand, similar to hexadecylamine (HDA), as reported previously for the growth of CdS nanorod architectures. ^[205]

6.2.3.2 Tetrapod nanocrystals with different arm shapes

As shown above, different temperatures result in different CdSe architectures (spherical core/shell, pyramidal and tetrapodal particles) in the presence of zinc blende seeds such as ZnTe. In this chapter, it will be shown that different arm shapes of tetrapodal nanocrystals can also be obtained as shown in figure 6.10. Besides changing the reaction temperatures and the zinc blende seeds (ZnTe, ZnSe or ZnS), in the following studies also the injection method was varied. It should be noted that the yield of tetrapodal nanocrystals is different for different batches from the identical zinc blende seeds.

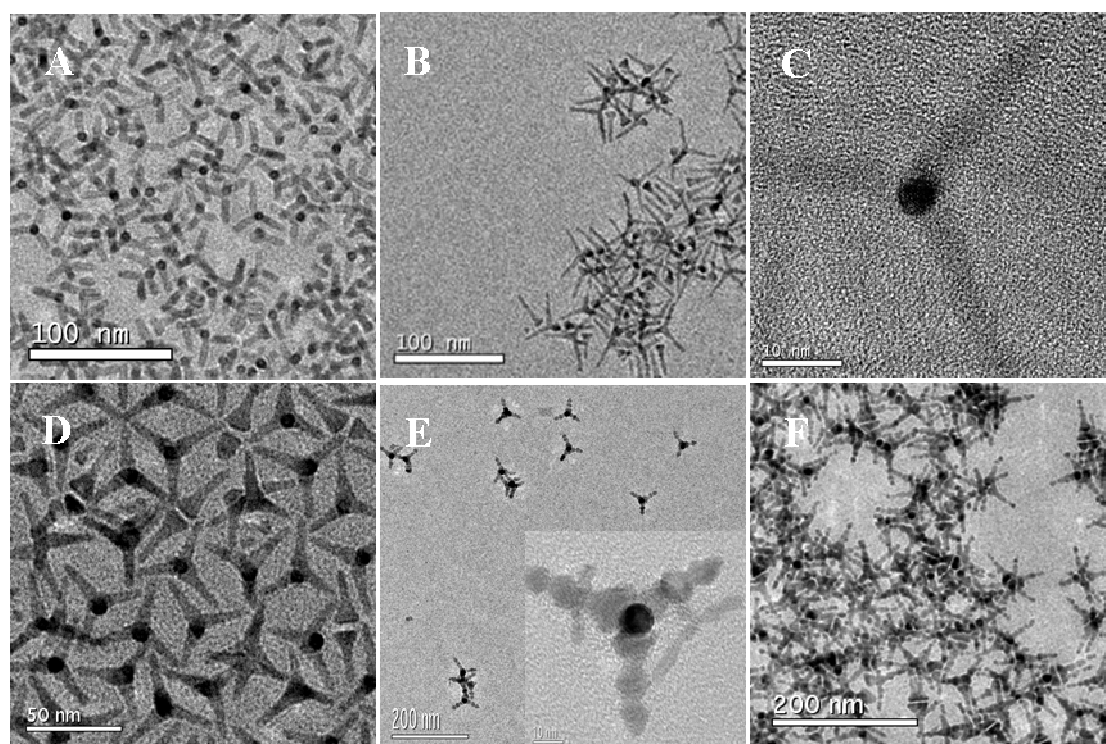


Figure 6.10 TEM image of CdSe tetrapod nanocrystals prepared at different temperatures and with different injection methods. (A) ZnTe cores, 215 °C and M SILAR method. (B) ZnSe cores, 215°C and M SILAR method. (C) A magnified part of a tetrapod from sample (B). (D) ZnSe cores, 215 °C and SILAR method. (E) ZnSe cores, 190 °C -230 °C, SILAR and M SILAR method .Inset is magnified part of a single tetrapod nanocrystal from sample (E). (F) ZnTe cores, 190 °C -230 °C, SILAR method and M SILAR method.

In figure 6.10 (A-D) it can be seen that tetrapodal nanocrystals with rod-shaped and nail-shaped arms can be obtained by using ZnTe or ZnSe seeds at 215°C. Furthermore, tetrapodal nanocrystals with arms of “chess-figure” structure as shown

in figure 6.10 E and F could be produced by changing the temperature and injection methods. (see Preparation methods)

It should be noted that in all cases shown in figure 6.10 the experimental conditions were changed after tetrapod shaped nanocrystals had been formed. Therefore, mainly the growth of the CdSe arms was influenced by a change of the experimental conditions. The tetrapod shaped nanocrystals shown in figures 6.10A and 6.10B were obtained under similar experimental condition (temperature, injection method). The difference is that the cores are not identical (A: (ZnTe) and B: (ZnSe). In general, the diameter of tetrapodal nanocrystals was determined by the time between Cd solution injection and Se solution injection. With an increase of this time period, the diameters of the arms slightly decreased. In case of image D, the shape of the arms (nail-like structure) is different from that shown in the images A and B due to different injection methods. In fact, it is difficult to exactly tune the diameter of the arms because it is influenced by different parameters such as reaction time, injection methods, temperature and nature of the cubic seeds. Usually arm diameters between 4.5 nm and 7 nm could be obtained for these systems. The length of arms could be extended up to 50 nm. If the precursor concentrations are getting too high, the tetrapodal nanocrystals will eventually precipitate out of the solution due to the formation of larger architectures with irregular shapes

For ZnS cores no formation of tetrapod-like structures was observed, even if different temperatures were used. For ZnSe cores, the yield of tetrapod nanocrystals was only about 20~40% under the best conditions. These results show that the nature of the cubic seeds is important for the growth of tetrapod nanocrystals. For comparison, the lattice parameters of cubic ZnTe, ZnSe and ZnS cores are 0.61 nm, 0.5668 nm and 0.542 nm respectively. Therefore, the lattice mismatch between the seeds and CdSe (0.605 nm) seems to be crucial during the growth of CdSe tetrapod architectures. According to these numbers, the lattice mismatch between ZnS and CdSe is over 10%. On the contrary, the lattice mismatch is very small (0.8%) between ZnTe and CdSe. This may be one reason why tetrapodal CdSe nanocrystals could not be prepared from cubic ZnS cores. In case of ZnSe cores, the lattice mismatch lies in between that of ZnS and ZnTe, which result in a low yield of tetrapod ZnSe/CdSe nanocrystals. Therefore, we assume that the lattice parameter may be an important factor for the growth of tetrapod shaped CdSe nanocrystals.

6.2.3.3 Optical properties

Figure 6.11 presents the optical absorption spectrum of the ZnTe/CdSe tetrapods. These nanocrystals exhibit a pronounced absorption band around 650 nm, which is attributed to the band-gap absorption of the CdSe arms of thickness around 7 nm.^[80] The absorption increases steeply towards higher energy, and a weak tail extending up to 900 nm is observed in the sub-band gap region. Such a long wavelength absorption tail appears to be a typical signature of type-II core/shell nanocrystals as discussed in chapter 5. Therefore, the absorption tail of the ZnTe/CdSe tetrapods is thought to result from the spatial separation of charge carriers between the ZnTe core and the CdSe arms and the concomitant decrease in wave function overlap. The same mechanism most probably is responsible for a complete lack of photoluminescence from the tetra-pods in our system. In this context one should remember that even spherical core/shell nanocrystals show extremely low quantum yields after the growth of more than three monolayers.

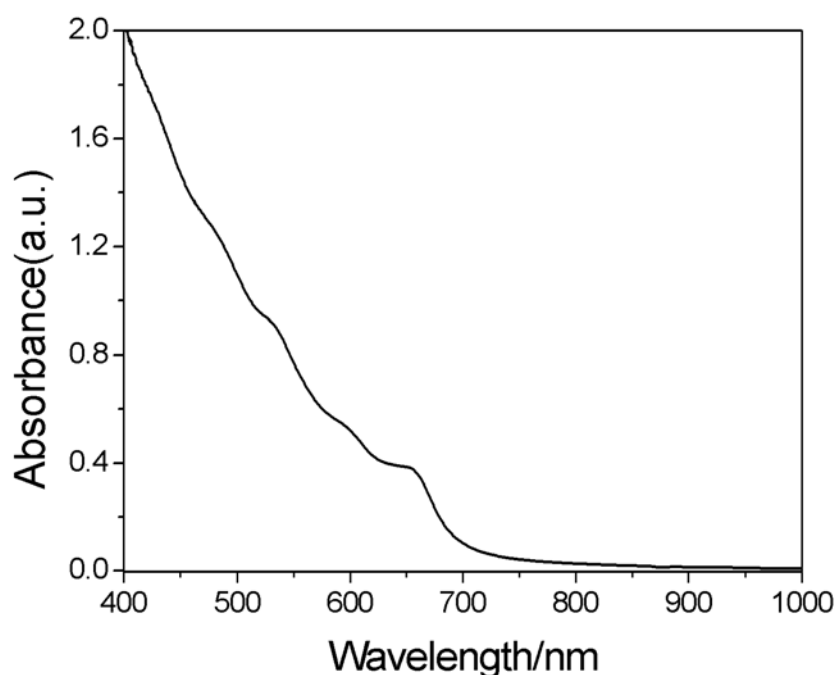


Figure 6.11 Absorption spectrum of a toluene solution of ZnTe/CdSe tetrapodal nanocrystals.

Considering the crystal structure and optical properties of ZnSe/CdSe tetrapodal nanocrystals, these are not only similar to those of ZnTe/CdSe tetrapodal, but also similar to those of nail shaped nanocrystal described below.

6.2.4 Nail-shaped nanocrystals

6.2.4.1 Structural characterization

As already mentioned before, nail-shaped CdSe nanocrystals could often be found when the synthesis of tetrapod CdSe nanocrystals was carried out at 215 °C. Figure 6.12 illustrates the shape evolution of nail-shaped CdSe nanocrystals grown at 190 °C with ZnS cores. It can be seen in figure 6.12 how the shape of ZnS/CdSe nanocrystals gradually changed from pyramidal to nail shape. The nail shape of the nanocrystals was well-developed, and the system morphology was maintained during the alternate injection of the Se and Cd solution following the SILAR method. The length of nail-shaped nanocrystals prepared under these conditions could be extended up to 120 nm with ~10% accuracy, while the average diameter could be varied from 4.5-7 nm by adjusting the time between successive injections of Cd and Se precursors during the growth of the nails. A remarkable feature is that the yield of the nanonails is almost 100% without post purification.

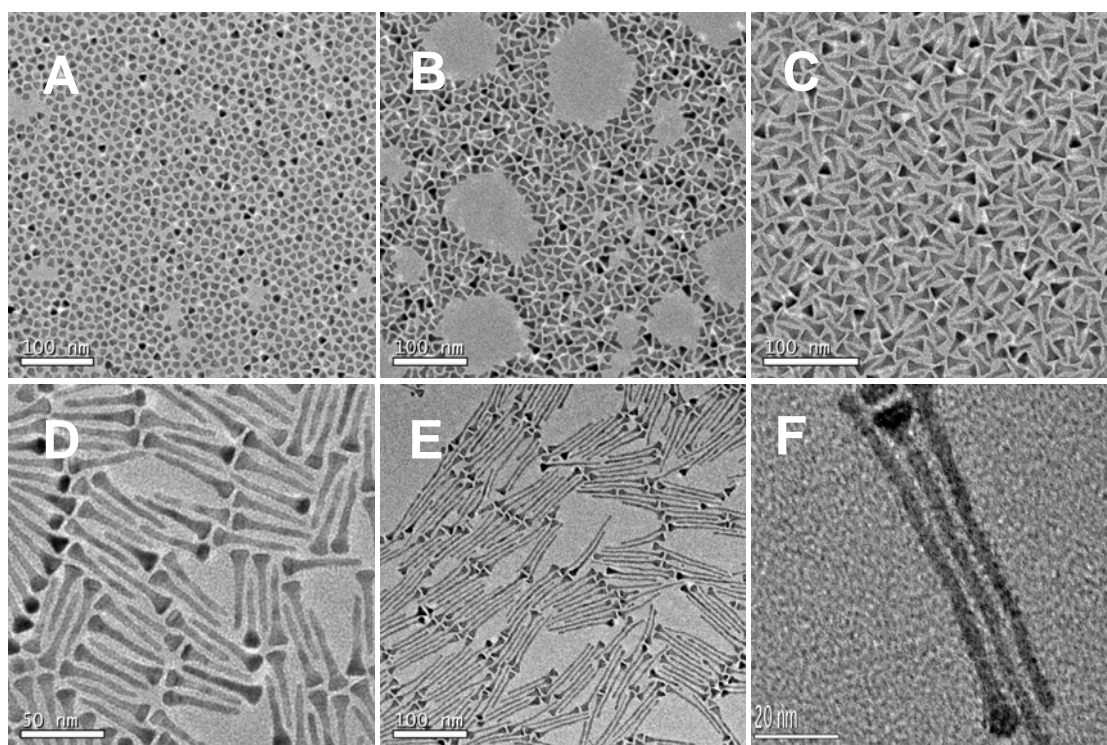


Figure 6.12 TEM images of ZnS/CdSe nanoparticles portraying the transition from pyramid ZnS/CdSe (A, B) to nail shape (C, D, E). (F) is a magnified part from (E) ($T=190$ °C).

To further investigate the structure of the nano-nails, figure 6.13 shows the HRTEM image of the head of a nanonail. Heads of ZnS/CdSe nanonails as a rule have

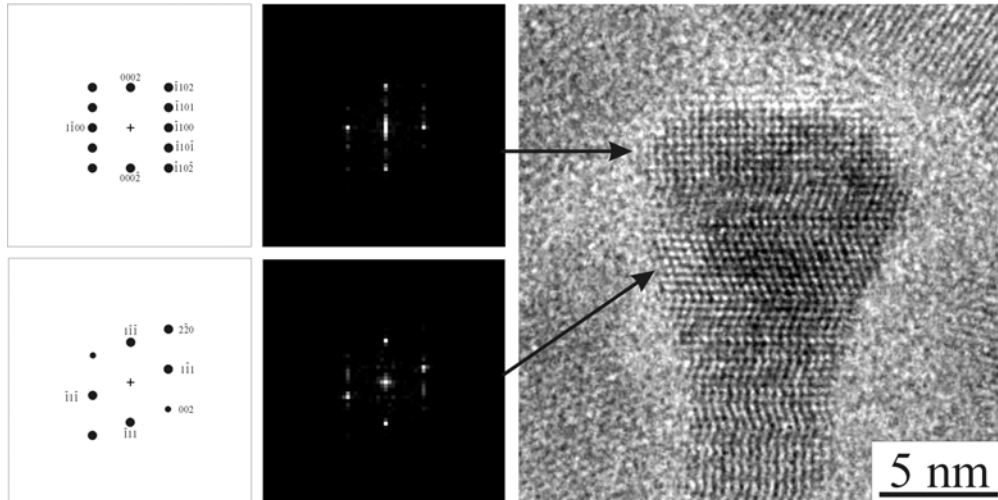


Figure 6.13 HRTEM image (right side) of a ZnS/CdSe nanonail and partial 2D FFT of the head of the nanocrystal (left side).

mixed hexagonal and faulted cubic structure, while the tails are of regular hexagonal wurtzite structure. Remarkably, the heads studied in this thesis show a similar pattern: the tips of the heads have approximately a 2.5 nm region with a defect-free hexagonal wurtzite structure. The hexagonal top is followed by an about 7 nm region with cubic zinc blende lattice structure. For the case shown a stacking fault is observed in this cubic region. At the bottom of the cubic region the regular hexagonal tail starts to grow. The FT image of the top part (see Figure 6.13) of the head confirms a hexagonal structure seen in $[11-20]$ direction oriented vertically to its $[0001]$ axis. The FT image of the cubic part of the head shows the pattern of an face centered cubic (fcc) structure viewed in $[1-10]$ direction with the $[111]$ vertical axis. Thus, the complete orientation relationship for the hexagonal close packed (hcp) and fcc structures is given by $[0001] \parallel [111]$ and $[11-20] \parallel [1-10]$.

The hexagonal nail tip has interplanar distances of 0.359 nm for the (0002) and 0.367 nm for the (1-100) reflection, respectively; these values agree well with the corresponding distances of hexagonal CdSe: 0.3505 nm and 0.372 nm, respectively. The cubic core shows distances of 0.367 nm for (111) and 0.317 nm for (002), which are slightly larger than what is expected for a relaxed ZnS crystal – 0.349 nm and 0.303 nm. The relaxed ZnS and CdSe lattices should have a rather high misfit of 12% at the $(111) \parallel (0001)$ interface. In our case we observe 5 % lattice expansion of the ZnS lattice, in other words a lattice parameter just between these of ZnS and CdSe. This is

to be expected since in this region we observe the diffraction from two matched lattices – the expanded lattice of ZnS and the contracted lattice of CdSe.

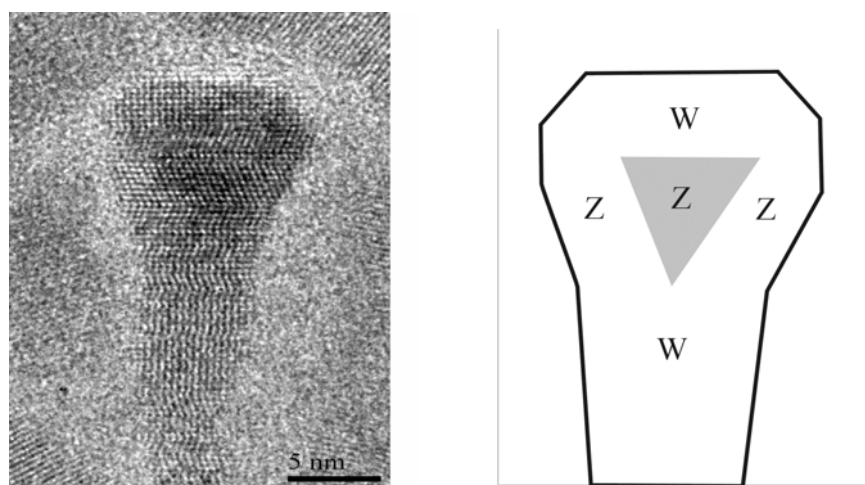


Figure 6.14 HRTEM image (left side: same as figure 6.13) of a ZnS/CdSe nanonail. The schematic structure of the nanonail is demonstrated on the right side. W: wurtzite structure. Z: zinc blende structure.

Figure 6.14 represents a schematic drawing of a ZnS nanocrystal buried in CdSe. The hexagonal tip of the head “freely” grows on the (111) plane of ZnS. Horizontally CdSe overgrows the core with the cubic structure, probably because of the perfect match of boundaries formed along the [111] tips of the encapsulated crystals compared to the complicated interface between two hexagonal structures. Here we may note that the hexagonal tip was probably formed first, and then the core was covered horizontally. The stacking fault seen in the cubic area should propagate through the whole construction, and probably existed already in the ZnS core. After the seed was completely covered and a suitable (111) facet was formed at the bottom, CdSe starts to grow in hexagonal structure.

It was already shown that different reaction temperatures and different cubic materials will lead to different shapes of CdSe nanocrystals prepared by SILAR. Now, the injection method is changed in a way that a mixture of the precursors (including Cd and Se) was added into the nanonail solution (length of nails ~ 100 nm) at 190 °C. Figure 6.15 shows the resulting nail-shaped CdSe nanocrystals. B is the magnified image of a single nanocrystal from the sample shown in A. Under these conditions, the growth of nanocrystals is difficult to control, resulting in CdSe architectures with

irregular shape. At the same time, the diameter of the nails is not the same from head to tail, probably due to the formation of spontaneous growth centers along the CdSe nails. Furthermore, the head of some nails is broken upon adding the precursors (Cd and Se).

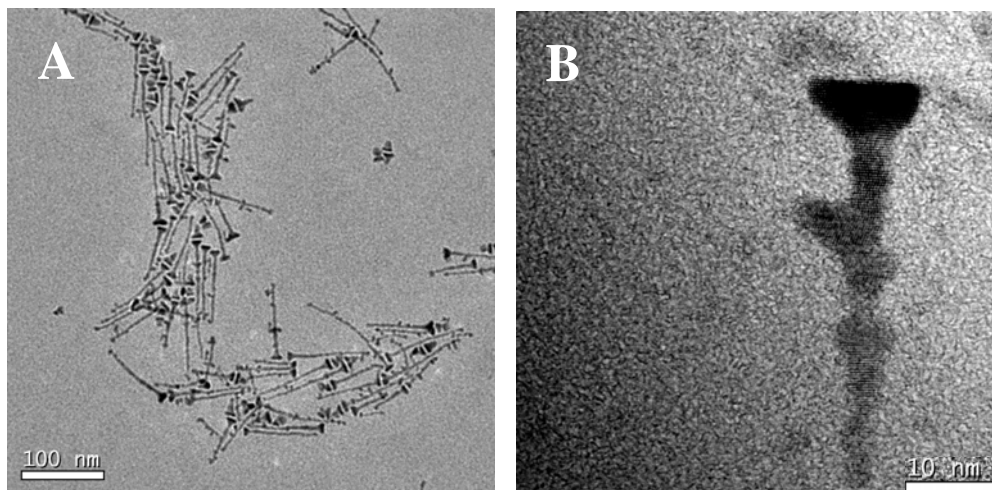


Figure 6.15 A: Branched nail shaped ZnS/CdSe nanocrystals. B: A magnified part of a single nanocrystal from the sample shown in image A

6.2.4.2 Optical properties

Figure 6.16 shows the absorption and photoluminescence spectra of nail-shaped ZnS/CdSe nanocrystals (see also Figure 6.12 E), which represent a reverse

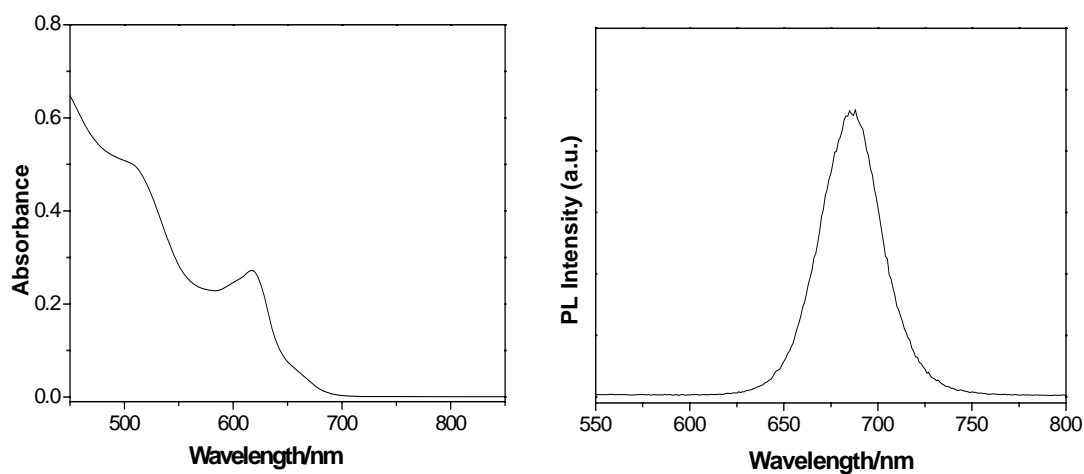


Figure 6.16 The absorption (left) and photoluminescence (right) spectra of nail-shaped ZnS/CdSe nanocrystals. (The sample: Figure 6.12 E)

type-I structure. It is found that the nail-shaped nanocrystals exhibit a pronounced absorption band around 610 nm, which is attributed to the band-gap absorption of the CdSe arms with diameter around 4.8 nm. In addition, a weak tail extending up to 700 nm is observed. The weak absorption tail is attributed to the absorption of the head of the nails, which leads to an emission at about 685 nm (QYs: $\sim 0.1\%$). This shows that the arms of the nails do not give rise to PL. The spectra (Figure 6.16) agree well with the nail structure, that is, the size of the head (about 10 nm) and the thickness of the arms (about 5 nm) as identified by TEM. (see Figures 6.12 E and F)

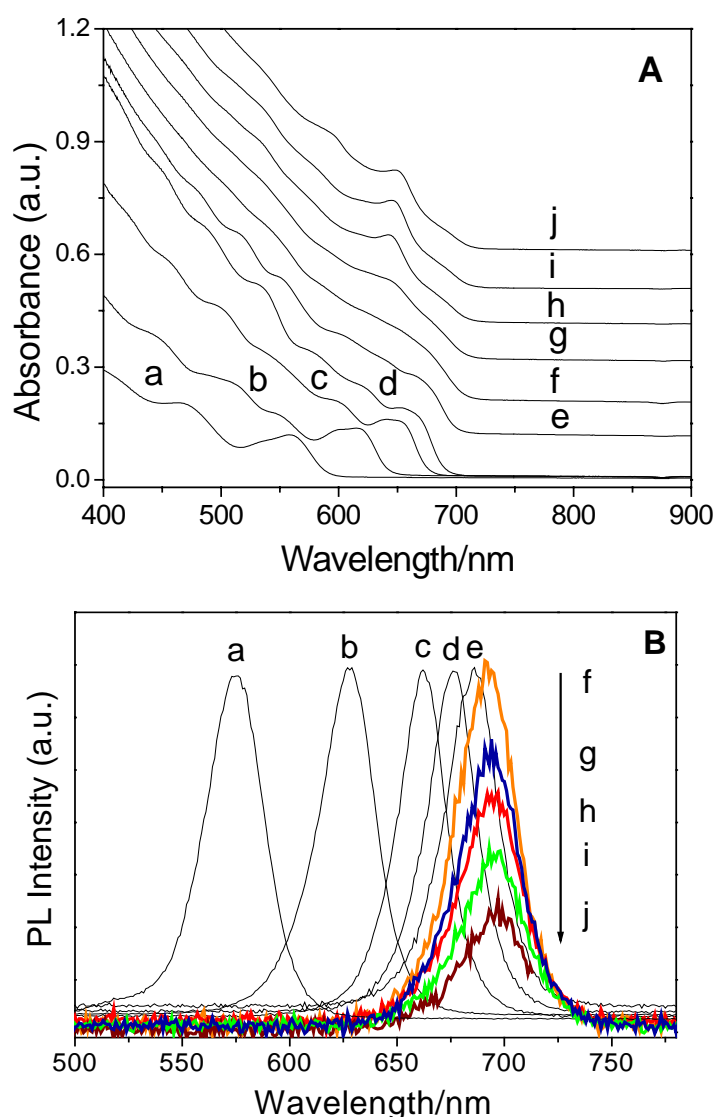


Figure 6.17: Evolution of the absorption and photoluminescence spectra during growth of nail-shaped CdSe nanocrystals by using cubic ZnSe seeds. The letters (a-j) in the absorption spectrum (A) corresponded to those in the PL spectra (B). The nominal number of monolayers of CdSe is: a, 1ML; b, 2MLs; c, 4MLs; d, 6MLs; e, 8MLs; f, 10MLs; g, 11MLs; h, 12MLs; i, 13MLs; j, 14MLs; k, 15MLs;

In the following, absorption and photoluminescence spectra of nail-shaped ZnSe/CdSe are discussed. These data are employed for monitoring the growth progress via the evolution of the absorption and photoluminescence spectra shown in figure 6.17. In fact, before the nail-shaped nanocrystals are formed (8 MLs), the absorption and photoluminescence spectra (Figure 6.17 (a-d)) are similar to those shown in figure 6.3 (e-h). With the formation of nail-shaped nanocrystals, the first absorption peak position (about 680 nm from e to j) remains almost unchanged with the addition of the precursors. In addition, the position of the emission stays almost constant with further growth of nail-shaped nanocrystals (Figure 6.17 B (e-j)). With increasing length of the nails, a “remarkable” absorption peak (~645 nm) was observed as shown in figure 6.17 A (g-j). On the contrary, the intensity of the first absorption peak (~680 nm) became weaker. This fact can be explained by the formation of long nail-shaped nanocrystals, and is also consistent with what was described in figure 6.16. The absorption peak at 645 nm is determined by the diameter of the nail-like arms, whereas the nail-heads of the nanocrystals give rise to the weak absorption tail around 670-680 nm. Obviously, the latter becomes weaker with increasing particle size, which probably is caused by the large amount of CdSe accumulated at the nail-head. Finally, those spectroscopic measurements have been complemented by TEM measurements (not shown here) which corroborate the formation of long nail-shaped nanoparticles.

In general, according to the literature^[206, 207] CdSe nanorods only show weak emission. In the present case, the arms of the nail-like nanocrystals resemble rod-like nanocrystals. The emission (690 nm) shown in figure 6.17 B is attributed to the head of the nanonails, corresponding to the absorption tail at ~670 nm. In fact, if the arms would show emission, the PL peak position should be at ~665 nm because the first absorption peak position of the arms is at ~645 nm. However, the nanonails only show an emission at 690 nm as shown figure 6.17 B. Therefore it is assumed that the arms show no detectable emission corresponding to the case of nail-shaped ZnS/CdSe nanocrystals.

Considering the photoluminescence QY of nanonails, an extremely low QY (~0.05%) was obtained for the nail-shaped ZnS/CdSe nanocrystals (see Figure 6.12 E). To follow the QY of nail-shaped nanocrystals during arm growth, the values obtained for ZnSe/CdSe are shown in figure 6.18. Before nail-growth, the behaviour

is consistent with that of spherical core/shell or pyramidal ZnSe/CdSe structures described before. However, we found that the QY of nail-shaped nanocrystals decreased greatly with the growth of CdSe arms. At present, no suitable explanation can be given.

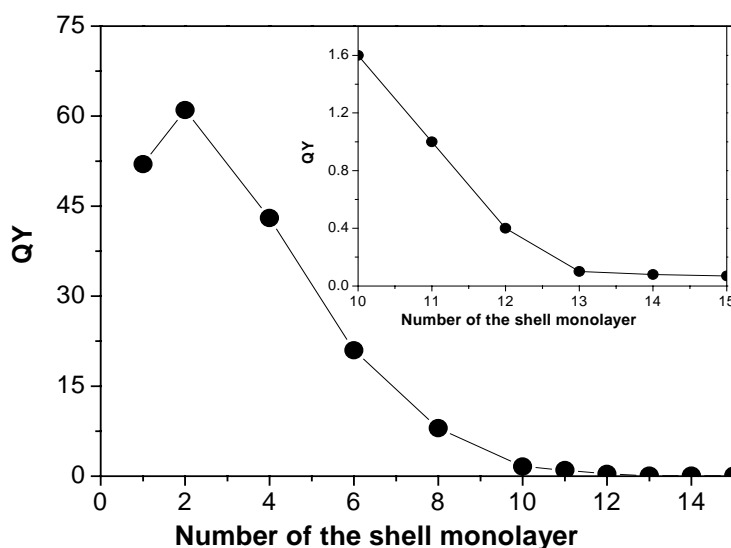


Figure 6.18 Evolution of QY of ZnSe/CdSe nanocrystals versus the nominal number of CdSe shells

6.2.5 “Chess- figure” shaped nanocrystals

In previous reports, the formation of CdSe nanocrystals with a variety of elongated shapes has been explored in detail, ^[54, 112] especially with respect to the effects of the concentration of monomers and ligands. As mentioned above, nail shaped and tetrapod shaped CdSe nanocrystals with different arm shapes have been prepared at 190 °C or 215 °C, respectively, from ZnS or ZnSe or ZnTe cores. By combining the effects of temperature and injection method, chess-shaped CdSe nanocrystals were obtained for the first time.

Figure 6.19 shows “chess-figure” shaped CdSe nanocrystals prepared from ZnSe/CdSe pyramidal nanocrystals synthesized as described in section 6.2.2 (see figure 6.4 C). We have shown above that when the temperature is set to 230 °C, large pyramid-shaped CdSe nanocrystal will be obtained (see figure 6.4 E). On the other hand, growth at 190 °C using the SILAR method resulted in nail-shaped nanocrystals as shown in figure 6.12. This is consistent with the results reported in figure 6.19 B. It can be seen that the larger nail shaped CdSe nanocrystals can be obtained if the temperature is set to 230 °C combined with the SILAR method (from Figure 6.19 B to

Figure 6.19 D). The width of the head and the shape of the nail arms can be tuned by varying the reaction temperature and the injection method. Accordingly, when going from figure 6.19 B to figure 6.19 C, reaction temperatures of 225 °C and 190 °C respectively, were used successively and the amounts of the subsequent injection

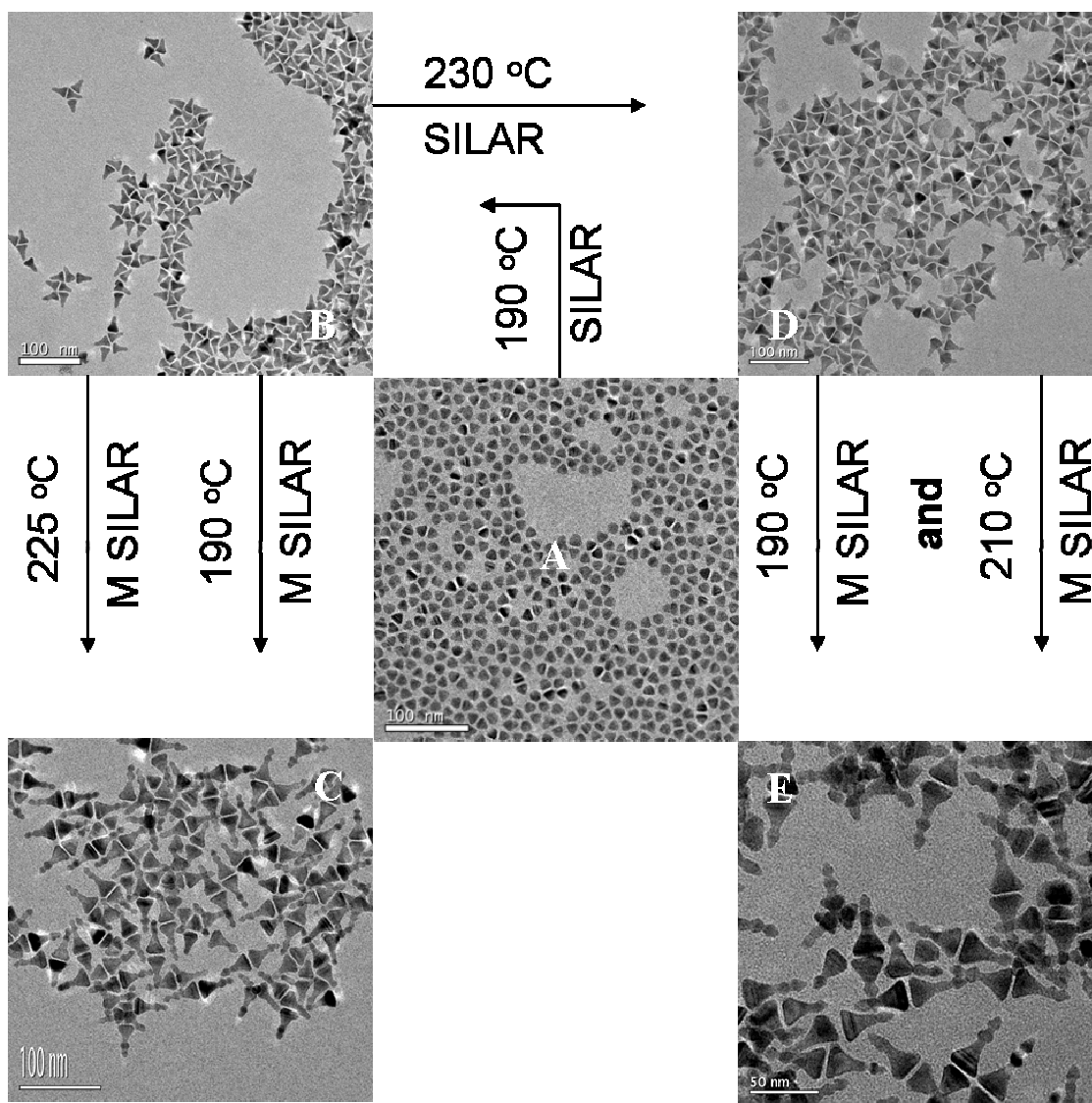


Figure 6.19 Formation of “chess-figure” shaped ZnSe/CdSe nanocrystals. Starting from pyramidal nanocrystals (A), nail-shaped nanocrystals (B) and (D), and chess-shaped nanocrystals (E) and (F) can be obtained by various synthetic routes. Crucial parameters are temperature and choice of injection methods. (1 and 2 is sequence of synthetic procedures)

solutions (modified SILAR or M SILAR) was kept constant (see preparation methods). This procedure leads to nanocrystals with chess-like structure. Similar “chess-figure” shaped nanocrystals are shown in figure 6.19 E, also prepared from nanonails (Figure 6.19 D) by the M SILAR method and a sequence of two different

temperatures (210 °C and 190°C). In fact, tetrapodal ZnSe/CdSe and ZnTe/CdSe nanocrystals with “chess-figure” shaped arms have also been obtained by means of this procedure. These experimental results indicate that novel and complex CdSe architectures can be produced by adjusting the injection method and the reaction temperature.

Figure 6.20 shows the UV absorption and PL spectra of the “chess-figure” shaped ZnSe/CdSe nanocrystals shown in figure 6.19 C. A broad absorption tail at a ~ 700 nm is observed. In fact, this spectrum is similar to that of nail-shaped nanocrystals shown in figure 6.17 (A). However, the size of the heads is about 20 nm, and the width of the arms is about 9 nm as determined by TEM. The “chess-figure” shaped nanocrystals completely lack PL, which for the sample shown in figure 6.19 C could originate from the weaker quantum confinement effect due to the large nanocrystal size (> 10 nm). Therefore, we assume that the broad absorption peak is attributed to band gap absorption of both heads and arms.

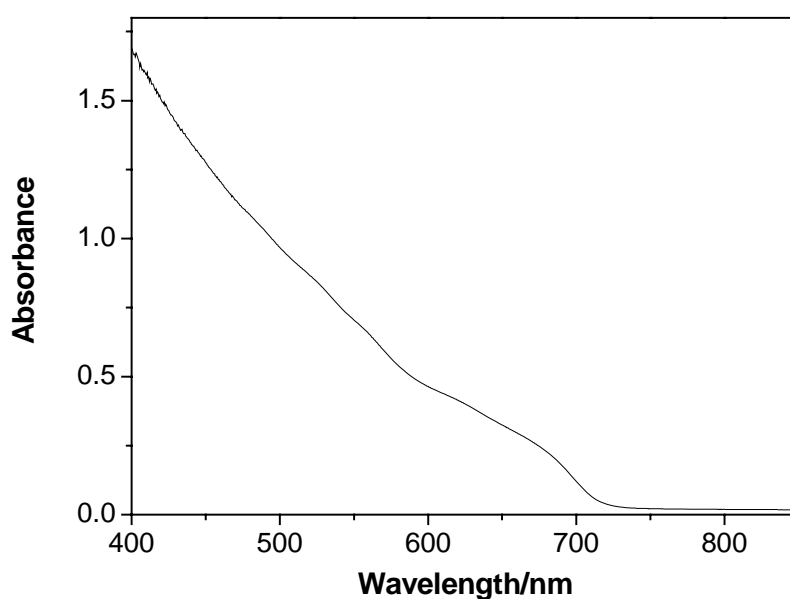


Figure 6.20 The absorption spectrum of “chess-figure” shaped ZnSe/CdSe nanocrystals. The sample is the same as that in figure 6.19 C

6.2.6 “Y” shaped nanocrystals

Figure 6.21 shows the evolution of CdSe architectures while adding drop by drop of a mixed injection solution (Cd and Se precursors) into a solution of cubic ZnSe seeds at 215 °C. The “Y” shaped CdSe nanocrystals shown in figure 6.16 B

were observed at least 20 min after addition of the precursors, although other shapes, such as rod, bi-pod, tri-pod tetra-pod and nail-like, were observed at the initial stages.

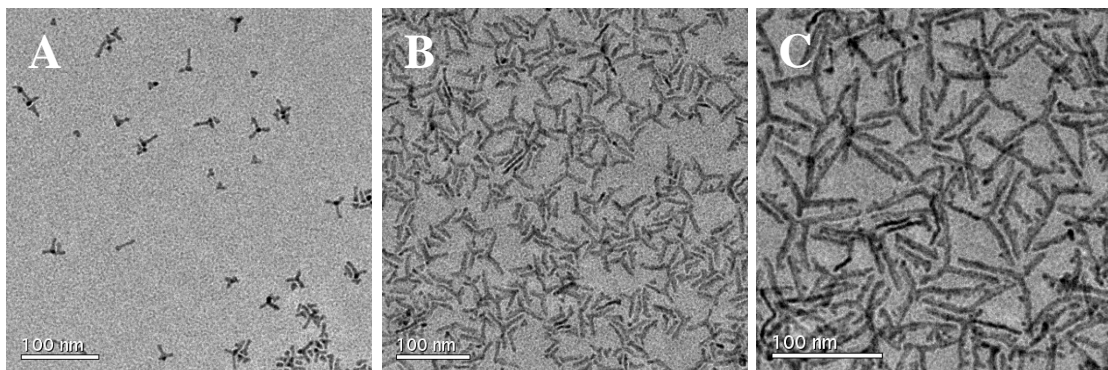


Figure 6.21 Shape evolution of ZnSe/CdSe nanocrystals by adding a mixture of precursors (Cd and Se) into a solution of cubic ZnSe seeds at 215 °C.

With growth of the nanocrystals, the morphology varied from Y-like to dot modified “Y” shaped structures shown in figure 6.21 C. Figure 6.22 is a HRTEM image of a single nanocrystal from the sample shown in figure 6.21 C. It reveals for all parts of the tripod nanocrystal that is viewed in the [11-20] direction which proves that it has a “flat” morphology.

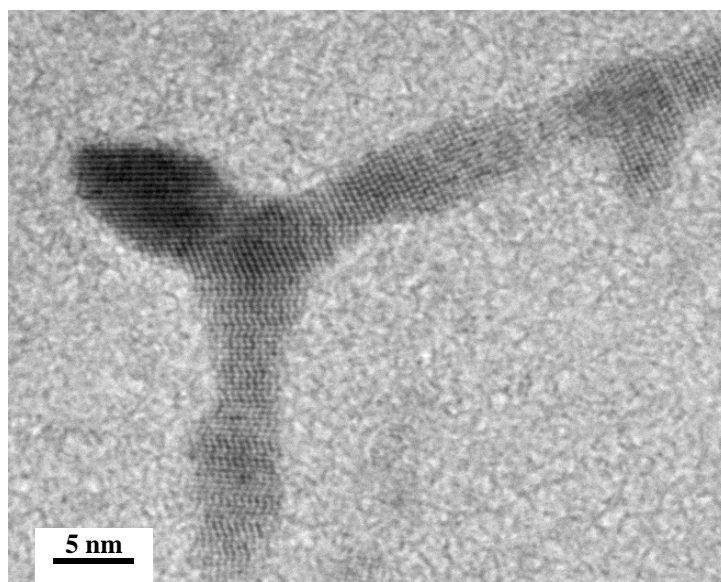


Figure 6.22 HRTEM image of a “Y-figure” shaped ZnSe/CdSe nanocrystal

Figure 6.23 shows the absorption and photoluminescence spectra of “Y” shaped CdSe nanocrystals. The first absorption peak is at about 625 nm, which is attributed to the band-gap absorption of the CdSe arms with diameter around 5.4 nm.

However, the size of the center and arms is almost identical which has been identified by the TEM measurement (see Figure 6.22). In addition, before the formation of “Y” shaped nanocrystals (see figure 6.21 A), the spectra (not shown here) are already similar to those in figure 6.23. Therefore, we assume that the PL spectrum is generated from the core/shell structure of the center. The QY of “Y” shaped ZnSe/CdSe amount to ~2-5%.

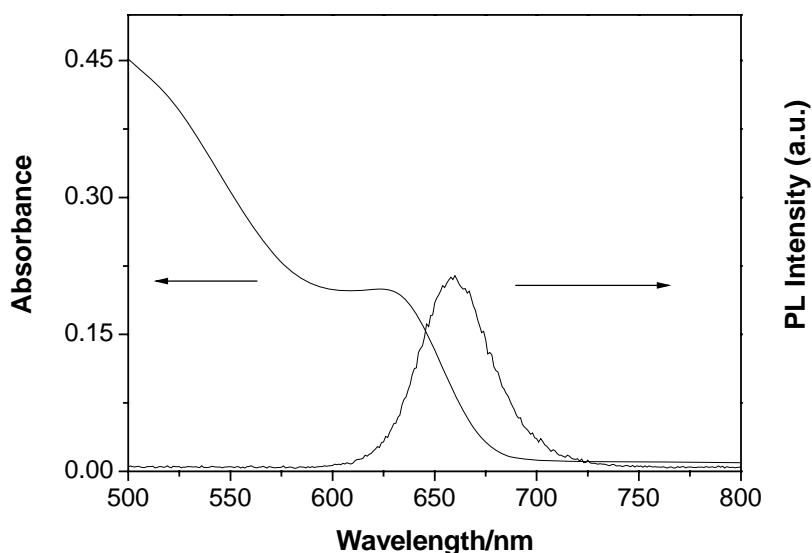


Figure 6.23 Absorption and photoluminescence spectra of “Y” shaped ZnSe/CdSe nanocrystals. The spectra were taken from the sample the TEM image of which is shown in figure 6.21 C.

It should be noted that the preparation of “Y”-shaped nanocrystals could not be well controlled. If different cubic seeds (ZnS and ZnTe) were used and mixed precursor solutions were added into the reaction mixture, a low yield of “Y” shaped CdSe nanocrystals was obtained (see Table 6.1). These results indicate that the injection method chosen for these experiments (addition of a mixture of precursors) does not offer the same level of control as SILAR and M-SILAR.

6.3 Conclusion

In this chapter, the controlled synthesis of colloidal CdSe nanocrystals in a variety of morphologies (spherical core/shell, pyramid, tetra-pod, nanonail, “chess-figure” shape and “Y” shaped nanocrystals) has been realized starting with zinc blende seeds from ZnS, ZnSe or ZnTe. Controlling the injection method and the reaction temperature allows for tuning the nanocrystal shape. Table 6.1 summaries the

different growth conditions (cubic seed, temperature and injection methods) for the CdSe architectures. These experiments provide novel information how to control the shape of nanocrystals grown from different cubic seeds. Much more experiments are

Cubic seed	Lattice parameter	CdSe architecture	Yield /(%)	Temperature/ °C	Injection method
ZnS	0.542 nm: Lattice mismatch with CdSe: ~11%	spherical	100	245	SILAR
		Pyramid	100	210 and 230	SILAR
		Nail	100	190	SILAR
		Tetrapod	-	-	-
		Chess	100	190 and 225	SILAR and MSILAR
		Y shape	40	220	Mixture of precursors
ZnSe	0.567 nm: Lattice mismatch with CdSe: ~7.4%	spherical	100	240	SILAR
		Pyramid	100	210 and 230	SILAR
		Nail	100	190	SILAR
		Tetrapod	20~40	215	SILAR or MSILAR
		Chess	100	190 and 225	SILAR and MSILAR
		Y shape	100	215	Mixture of precursors
ZnTe	0.610 nm: Lattice mismatch with CdSe: 0.8%	spherical	100	240	SILAR
		Pyramid	90	215 and 230	SILAR
		Nail	90	190	SILAR
		Tetrapod	70~90	215	SILAR or MSILAR
		Chess	80~90	190 and 230	SILAR and MSILAR
		Y shape	70	220	Mixture of precursors

Table 6.1 Overview of various CdSe architectures grown out of cubic seed of ZnS, ZnSe or ZnTe. The table specifies approximate reaction yields, temperatures and injection methods

needed to arrive at an understanding of the growth mechanism(s) involved. Nevertheless, it is believed that the concept of alternate injection (SILAR and M-SILAR) of precursor solutions at intermediate temperatures in the presence of suitable coordinating ligands allows us to precisely control the formation of anisotropic nanoparticles.

6.4 Preparation methods

6.4.1 Synthesis of zinc blende core nanocrystals:

A) ZnTe seeds: The detailed synthesis of cubic ZnTe nanocrystals is reported elsewhere.^[204] For a typical reaction, oleylamine (1 g) and ODE (3 g) were loaded into a reaction flask. The solution was heated to 280 °C under argon. A solution of tellurium and diethylzinc (1ml, molar ratio Te: Zn=1:1) in TOP was injected quickly into the reaction flask. After the injection, the reaction temperature was set to 270 °C to grow nanocrystals for 3 minutes. Finally, the solution was cooled down to room temperature for the growth of the CdSe architectures.

B) ZnSe seeds: The cubic ZnSe nanoparticles were prepared using a synthetic route reported earlier.^[28] Typically, 5.0 g of oleylamine was heated to 310 °C under Ar. At this temperature, a solution of 0.3 mmol Se in 2.0 ml of trioctylphosphine (TOP) was added to the flask. After the temperature was readjusted to 310 °C, 0.3 mmol ZnEt₂ in 1.0 ml of TOP was swiftly injected into the reaction vessel. The reaction mixture was stirred at 300 °C for 10 min., and then cooled down to room temperature. The reaction solution was diluted to 25.0 ml by adding octadecene (ODE) at ~70 °C. This approach results in ZnSe nanocrystals with an average size of around 3.0 nm in diameter.

C) ZnS seeds: Zinc blende ZnS nanocrystals were prepared according to a procedure described in the literature.^[208] In a typical reaction, Zinc stearate (0.1264 g, 0.4 mmol) and a certain amount of tetracosan and ODE were loaded in a 25 mL three-neck flask. The mixture (4 g in total) was heated to 340 °C under Ar flow. A solution of sulfur (0.0064 g, 0.1 mmol) in 1 g ODE was swiftly injected into this hot solution, and the reaction mixture was cooled to 300 °C for growth of the ZnS nanocrystals for about 5 min. The obtained ZnS nanocrystals are about 3.2 nm in diameter.

6.4.2 Synthesis of CdSe architectures using different cubic cores

6.4.2.1 Injection procedures

A) Injection solutions: The Cd precursor solution (0.1 M) was prepared by dissolving CdO (0.3204 g) in oleic acid (4.18 g) and ODE (20.0 ml) at 240 °C under argon. The Cd precursor solutions were kept at about 80°C and then used at elevated temperatures for growth of the CdSe architectures. The Se solution (0.1 M) was prepared by dissolving the Se powder in TOP/ODE (v/v=1:9) at room temperature. For each injection, a calculated amount of a given injection solution was taken with a syringe using a standard air-free procedure.

B) Three injection methods: Three different injection methods were used to investigate their effect on the growth of CdSe nanocrystals from identical cores:

1) In the first method, the injection solution was added into the reaction solution according to the SILAR method. The volume of the injection solution was calculated as described in literature.^[165]

2) The second method, a modified SILAR method (M-SILAR), means that the same amount of Se or Cd precursors were injected alternately into a reaction solution after the formation of pyramid CdSe nanocrystals.

3) In the third method, the injection solutions of Se and Cd precursors were mixed together, and then this mixture was added into the reaction solution drop by drop.

C) Calculation of injected amounts: CdSe nanocrystals were grown from cubic cores in general. For the first method (SILAR method), the amount of the injection solution for each injection step was estimated from the respective volumes of hypothetical concentric spherical shells with a thickness of one monolayer. For the second method (M-SILAR), the amount of injection solution was calculated by using the first method (SILAR) until pyramidal nanocrystals were formed. Then, the volume of the injections was kept constant until the end of the experiments.

6.4.2.2 Synthesis of spherical CdSe nanocrystals

Preparation of the spherical nanocrystals using the SILAR technique: A typical SILAR synthesis was performed as follows: 2 ml ODE, 0.04 mmol ZnSe seeds and 2 ml OAm were loaded into a 50 ml reaction vessel, heated to 100 °C under

vacuum for 1 hour. Subsequently, the solution was heated to 240 °C under Ar. Cd and Se were added to the solution by alternating injections. For the first, second and third injection, 0.24 ml, 0.30 ml and 0.38 ml, respectively, of 0.1M Cd and Se precursor solutions were used. For subsequent injection solutions, their amounts were calculated by SILAR method. It is found that a period of 10~15 min between each addition was sufficient for the reaction to be completed. Finally, the solution was cooled down to room temperature.

6.4.2.3 Synthesis of pyramidal CdSe nanocrystals

A typical synthesis of pyramidal CdSe nanocrystals was performed as follows: 2 ml ODE, 0.04 mmol ZnSe seeds and 2 ml OAm were loaded into a 50 ml reaction vessel, heated to 100 °C under vacuum for 1 hour. Subsequently, the solution was heated to 210 °C under Ar. 0.1 M Cd and Se were added to the solution by alternating injections. For the first, second, third, fourth, fifth and sixth injection, 0.24 ml, 0.30 ml, 0.38 ml, 0.48 ml, 0.6 ml and 0.75 ml respectively, of 0.1M Cd and Se precursor solutions were used. When the shape of CdSe was pyramid-like after the sixth injection, the reaction temperature was heated to 230 °C for further growth of CdSe nanocrystals. Then, the amount of sequent injection solution was still calculated by SILAR method. For example, the seventh injection, 0.93 ml of 0.1M Cd and Se precursor solutions were used. Finally, the solution was cooled down to room temperature.

6.4.2.4. Synthesis of tetrapod CdSe nanocrystals with rod shaped arms

All reaction steps were performed using standard air-free techniques. For a typical reaction, 2 ml of oleylamine and 2 ml of ODE were added to a three-neck flask containing the pre-prepared ZnTe or ZnSe cores (0.02 mmol), and heated to 215 °C under argon. Cd and Se were added to the solution by alternating injections. For the first, second and third injection 0.12 ml, 0.18 ml and 0.25 ml, respectively, of 0.1M Cd and Se precursor solutions were used. After the third injection the amount of solution added in further injections (0.35 ml, 0.1M Cd and Se solutions) was kept constant. During arm growth, tetra-pod nanocrystals were taken from the reaction mixture for TEM measurements. We found that a period of 10~15 min between each addition was sufficient for the reaction to be completed, because the TEM images

showed no further changes for the arm lengths. Finally, the solution was cooled down to room temperature.

6.4.2.5 Synthesis of tetrapod CdSe nanocrystals with nail shaped arms

For a typical reaction, 2 ml of OAm and 2 ml of ODE were added to a three-neck flask containing the pre-prepared ZnTe or ZnSe cores (0.04 mmol), and heated to 215 °C under argon. Cd and Se were added to the solution by alternating injections. For the injection solution, the amount of injections is dependent on the calculation based on the assuming a spherical ZnSe/CdSe core/shell structure as described in section 6.2.4.2. It should be noted that not only tetrapods but also nails were found.

6.4.2.6 Synthesis of nail-shaped CdSe nanocrystals using ZnS, ZnSe or ZnTe nanocrystals.

For a typical synthesis of nail-shaped CdSe nanocrystals, 2 ml OAm and 2 ml ODE were added to a three-neck flask containing the pre-prepared ZnSe, ZnS or ZnTe cores (0.04 mmol) and heated to 190 °C under argon. Cd and Se were added to the solution by alternating injections. For the first, second and third injection 0.28 ml, 0.38 ml and 0.5 ml, respectively, of 0.1M Cd and Se precursor solutions were used. When the shape of CdSe was pyramid-like, the amount of the solution added in further injections was kept constant (M-SILAR) and nail-shaped CdSe nanocrystals with identical length and diameter were obtained. If the amount of injections was calculated assuming an isotropic core/shell structure (SILAR), the diameter of the nails is varying from head to tail.

6.2.4.7 Synthesis of “chess-figure” shaped CdSe nanocrystals using ZnSe or ZnTe seeds.

For the typical synthesis of “chess-figure” shaped CdSe nanocrystals, 2 ml OAm and 2 ml ODE were added to a three-neck flask containing the pre-prepared ZnSe or ZnTe cores (0.04 mmol) and heated to 215 °C under argon. 0.1M Cd and Se were added to the solution by alternating injections. When the particle became pyramidal-shaped (~ 6-7 MLs), the reaction temperature was set to 190 °C for grow of nail-shaped nanocrystals. The amount of injections is dependent on the calculation based on an isotropic ZnTe/CdSe core/shell structure (SILAR method). After formation of nail-shaped CdSe nanocrystals with addition of two injection solutions (0.1 M Cd and Se respectively), the amount of solutions added in further injections

was kept constant (M-SILAR method). Then the solution was heated again to 225 °C for further growth of CdSe nanocrystals by SILAR method. After addition of Cd and Se precursors (~ 2 MLs), the solution was set again to 190 °C for the subsequent growth of “chess-figure” shaped CdSe nanocrystals. The chess-shaped CdSe nanocrystals will be obtained eventually by injecting the next Cd/Se precursors.

6.4.2.8 Synthesis of “Y” shaped CdSe nanocrystals

A typical synthesis of the “Y” shaped CdSe nanocrystals was performed as follows: 2 ml ODE, 0.02 mmol ZnSe seeds and 2 ml OAm were loaded into a 50 ml reaction vessel, heated to 100 °C under vacuum for 1 hour. Subsequently, the solution was heated to 215 °C under Ar. A mixture of precursors (0.1 M Cd and Se) was added into the reaction mixture (2ml ODE, 2ml oleylamine and 0.04 mM ZnSe) drop by drop (about 1 drop in every 2-3 s) by syringe. Finally, the solution was cooled down to room temperature.

7. Organic surface modification of nanocrystals

7.1 Introduction

Colloidal nanocrystals in solution are a metastable species in comparison to the corresponding bulk crystals/solids and therefore have to be kinetically stabilized. The most common method to keep them stable is attaching a monolayer of organic molecules to the atoms on the surface of the nanocrystals. These organic molecules are often called surfactants, capping groups or ligands. In addition to the protection function, this monolayer of ligands on the surface of a nanocrystal provides the necessary chemical processibility which strongly depends on the terminal groups of the ligands pointing to the outside environment. Here, the stability of the ligands on the surface of the nanocrystals is the key concern, which ultimately determines the stability of the entire nanocrystal/ligand complex.

After having established reliable synthetic techniques, for instance the synthesis of high quality CdSe nanocrystals, much work is devoted to particle surface modification for specific purposes.^[21, 209] For example, CdSe nanocrystals can be used as donors in energy transfer systems^[64, 210, 211] and also as labels in biology.^[59] The main modification work nowadays is focused on making nanocrystals water soluble,^[212-214] because of a lack of stable water-soluble quantum dots with optical properties comparable to their hydrophobic analogue. (see also Chapter 2: Table 2.1).

There are two main approaches to obtain water-soluble nanocrystals: 1) nucleation of nanocrystals inside stabilizing micelles in an aqueous phase^[116] and 2) via an exchange of initially hydrophobic ligands by hydrophilic ones.^[13] Water-soluble nanocrystals which are obtained by the first route have a large size polydispersity and poor fluorescence quality. Therefore, in this work the second route was explored: the CdSe, CdSe/ZnS, CdSe/CdS and CdSe/CdS/Zn_{0.5}Cd_{0.5}S/ZnS nanocrystals (see Chapter 4) were originally coated by a layer of hydrophobic capping molecules (TOPO, ODA/OA), which supported solubility of the nanocrystals in hydrocarbon organic solvents (toluene, hexane, chloroform etc). The exchange of the capping molecules with hydrophilic ligands results in solubility of the nanocrystals in water.

Practically, there are different ways to exchange the ligand shell of hydrophobic nanocrystals. A most simple method for ligand exchange is the phase transfer of the nanocrystals from organic solvent to water. This phase transfer is

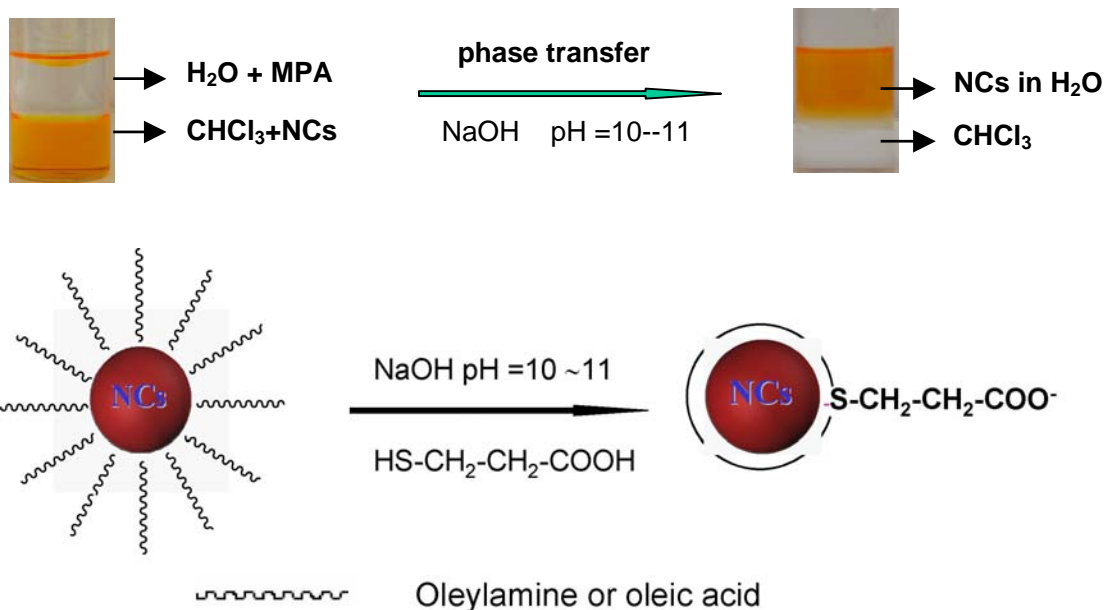
realized by mixing the organic solution of the nanocrystals with an aqueous solution containing an excess of hydrophilic ligands. The procedure requires mild conditions: room temperature, and short reaction time. Moreover, it gives higher chemical yields and the quality of the water-soluble nanocrystals is better compared to the previously introduced method (nanocrystals prepared inside micelles). In the case of amphiphilic ligand molecules, which are soluble in the organic phase as well as in water, it is also possible to mix the nanocrystals and the ligands in the organic phase and add pure water for the extraction of the nanocrystal/hydrophilic ligand complexes. In practice, most of these water soluble nanocrystals are not stable, especially towards photochemical and photooxidative degradation.

The topic of this chapter is the surface modification of nanocrystals by different organic molecules to obtain surface functionalized nanocrystals. For the realization of these structures several ligands were employed: hydrophobic ones such as calixarenes, and hydrophilic ones as for example cyclodextrins. In addition, a water soluble nanocrystal system was obtained by aminoethanethiol (AET) and mercaptopropionic acid (MPA), respectively. Detailed results will be discussed in the following.

7.2 Transfer into the aqueous phase by various ligands

7.2.1 Mercaptopropionic acid (MPA)

In order to investigate the influence of molecular surface modification on the PL-QY for different core/shell particles, we performed ligand exchange experiments as described above. In particular, we measured the PL of amino covered core/shell particles in organic solution, and compared it to the PL after ligand exchange with MPA and transfer to the aqueous phase, as explained in the experimental section. We picked mercapto propionic acid (MPA), because the ligand exchange leads to a change of the surface polarity from hydrophobic to hydrophilic as shown in scheme 7.1. Hence the particles, which were initially soluble in chloroform, become water soluble and the ligand exchange could be followed by the progress of the phase transfer. Table 7.1 shows the PL-QYs before and after phase transfer. We found that the MPA coating of the pure CdSe cores leads to a nearly complete quenching of the PL, consistent with earlier observations.^[143] In contrast, the PL of the core/shell nanocrystals was only partially quenched after ligand exchange by MPA.



Scheme 7.1. Synthetic approach towards hydrophilic nanocrystals by phase transfer of hydrophobic precursors.

As seen in table 7.1, the decrease of the PL-QYs depends on the particular core/shell structure of the nanocrystals. We found that the PL is decreasing to a stronger degree for particles with a CdS-shell. This is most likely due to the smaller band offset for the CdSe/CdS material combination (see Figure 4.2 in chapter 4), which leads to a higher probability for the charge carriers to be found at the particle surface.

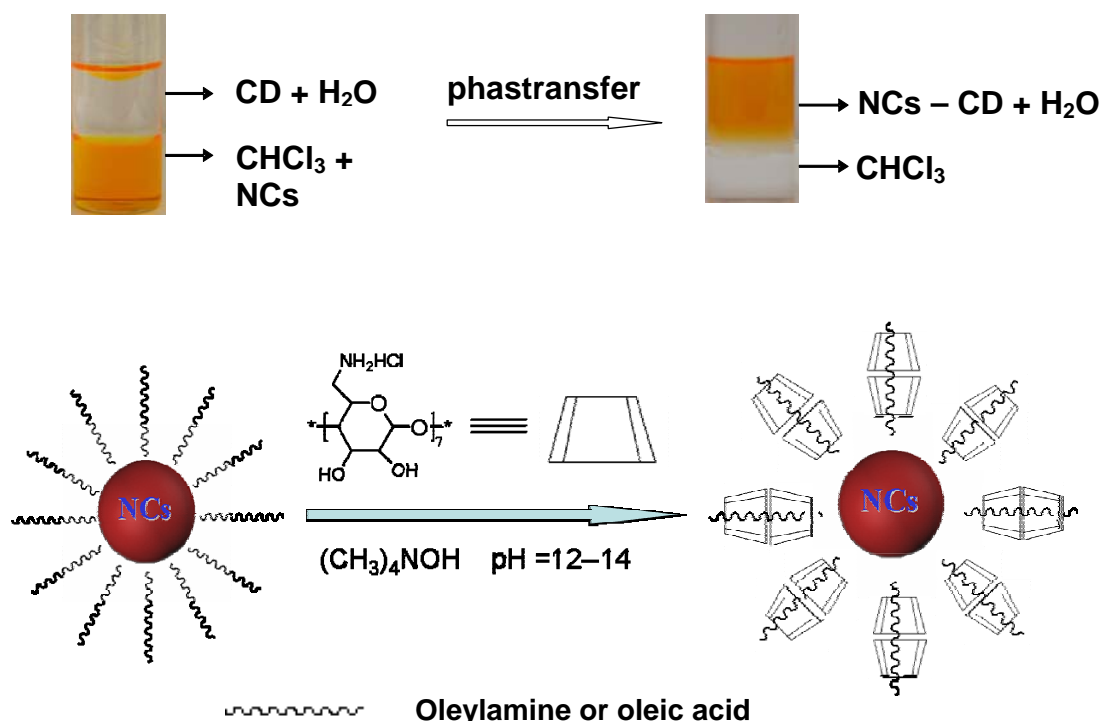
Ligand/solvent	QY in %			
	CdSe	CdSe/CdS	CdSe/ZnS	CdSe/CdS/ZnCdS/ZnS
ODA/chloroform	30	50	40	70
MPA/water	<< 1	10	20	50

Table 7.1 Photoluminescence quantum yields of core and core/shell nanocrystals covered with ODA/oleic acid in chloroform compared to the MPA covered particles in water

While the decrease of the PL-QY is similar for the CdSe/ZnS- and multi-shell CdSe/CdS/Zn_{0.5}Cd_{0.5}S/ZnS-nanocrystals, the absolute QY of the MPA-coated multi-shell particles is still of the order of 50%, due to the higher initial QY of those particles.

7.2.2 Peramino- β -cyclodextrin (CD)

Following the results described above, solely multi-shell nanocrystals were employed for phase transfer studies in this chapter. These nanocrystals, which originally carry oleic acid or oleylamine ligands and therefore are stable in organic solvents, can be transferred into aqueous solution by the simple phase transfer method described above using an aqueous solution of amino-functionalized cyclodextrin (CD).^[215, 216] The CD was provided by the group of Professor Wenz (Organische Makromolekulare Chemie der Universität des Saarlandes). Our synthetic approach, as well as a model how the hydrophilic ligand molecules attach to the hydrophobic nanocrystals, is summarized in scheme 7.2.



Scheme 7.2.: Synthetic approach towards hydrophilic nanocrystals by phase transfer of hydrophobic precursors.

7.2.2.1 Structure and size of water-soluble multi-shell nanocrystals

In order to identify the complex structure of oleic acid/oleylamine and β -CD as sketched in scheme 7.2, H^1 -NMR spectra were used. Figure 7.2.1 illustrates the H^1 -NMR of peramino β -cyclodextrin (d), and of the multi-shell nanocrystals before (c) and (e) after phase transfer. The sharp peaks at the corresponding positions of ligands (Figure 7.2.1 (a, b)) and peramino β -cyclodextrin in figure 7.2.1(d) imply that ligands and peramino β -cyclodextrin both are still on the surface of water soluble multi-shell nanocrystals (see Figure 7.2.1 (e)). It should be noted that it is difficult to determine the species of hydrophobic ligands (oleic acid or oleylamine) from H^1 -NMR spectra due to the similarity of their signals (Figure 7.2.1 (a) and Figure 7.2.1 (b)). Therefore, we assume that the original ligands including oleic acid and oleylamine are not or only partially replaced by peramino β -cyclodextrin (CD) molecules during phase transfer (see Figure 7.2.1 (d) and Figure 7.2.1 (e)). This result is also consistent with the results reported in the literature. ^[217]

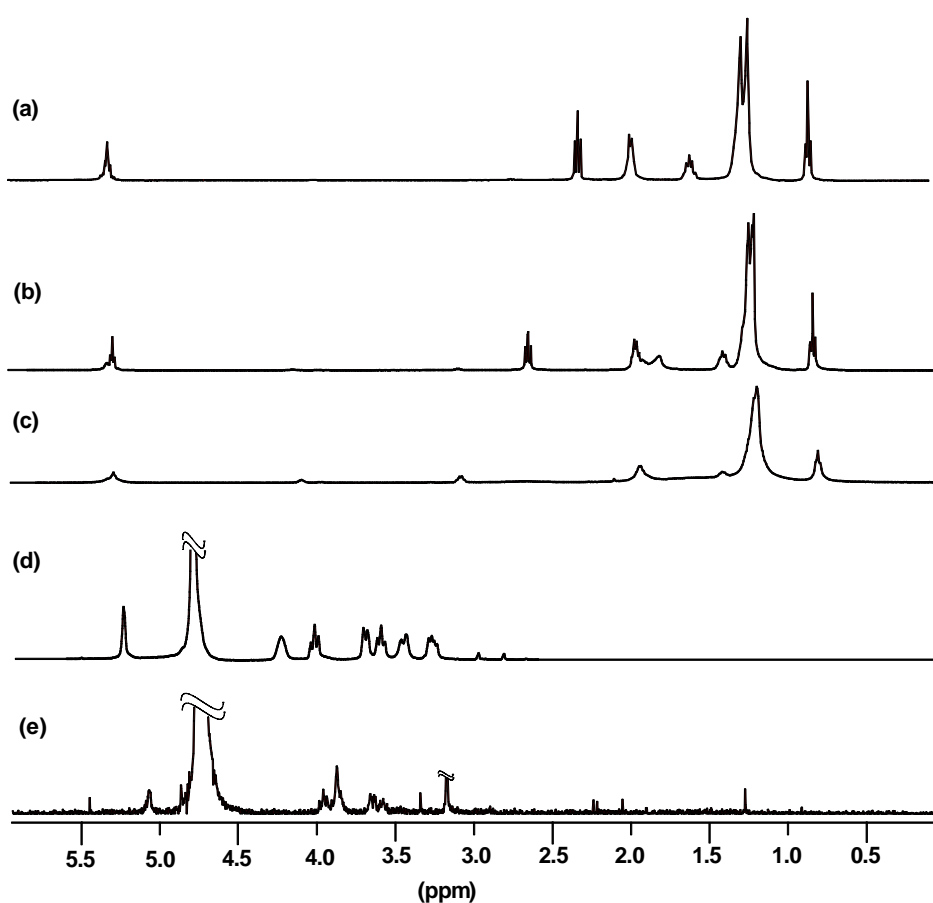


Figure 7.2.1 H^1 NMR of (a) oleic acid, (b) oleylamine (c) multi-shell CdSe nanocrystals, (d) peramino β -cyclodextrin and (e) CdSe-peramino β -cyclodextrin complex.

We assume that the CD molecules are wrapped around the hydrocarbon chains still bound to the multi-shell nanocrystal surface. This topological model is supported by the estimated number of CD molecules per nanocrystal as shown in table 7.2.

	Amount NCs	Amount CD	Before phase transfer: Ratio of CD/NCs	After phase transfer: Ratio of CD/NCs
1	$1 \cdot 10^{-8}$ mol	$2.2 \cdot 10^{-6}$ mol	220:1	108:1
2	$1 \cdot 10^{-8}$ mol	$1.2 \cdot 10^{-6}$ mol	120:1	102:1
3	$1 \cdot 10^{-8}$ mol	$0.7 \cdot 10^{-6}$ mol	70:1	100:1

Table 7.2: Average number of CD molecules per nanocrystal for 3 different phase transfer conditions (that is, various concentrations of CD in the aqueous phase)

The values given in the table have been determined by fluorescence spectroscopy using the enhancement of the fluorescence emission of the fluorescent dye 2-(p-Toluidino)-6-naphthalenesulfonic acid potassium salt (TNS) in presence of CD (see Figure 7.2.2): after precipitation of the multi-shell nanocrystals with methanol, the supernatant fluid was added to a standard solution of the fluorescent dye TNS, which due to complexation with cyclodextrin shows a strong enhancement of its fluorescence emission, which is proportional to the concentration of cyclodextrin. ^[218, 219] For calibration, aqueous solutions containing only cyclodextrin at various concentrations were added to the TNS-standard, and the resulting fluorescence intensities were recorded in dependence of CD concentration. By this procedure, the amount of CD not attached to the nanocrystals could be determined, leading directly to the corresponding number of CD molecules attached, on average, onto a single nanocrystal. Interestingly, the number of CD molecules per nanocrystal given in table 7.2 is comparatively large and independent of the CD concentration of the aqueous phase before phase transfer. Taking into account the surface area of the nanocrystals and the size of a single CD molecule - using the diameter of the pure nanocrystal of 6 nm, and the diameter of the β -cyclodextrin-molecule of 1.5 nm, ^[220] we obtain a

number of 62 cyclodextrin molecules for a closed monolayer around the nanocrystal. The amount of CD molecules per nanocrystal determined from our experiments rather corresponds to a bilayer than to a closed monolayer, and the assumed structure of our hydrophilic nanocrystals is sketched in figure 7.2.3.

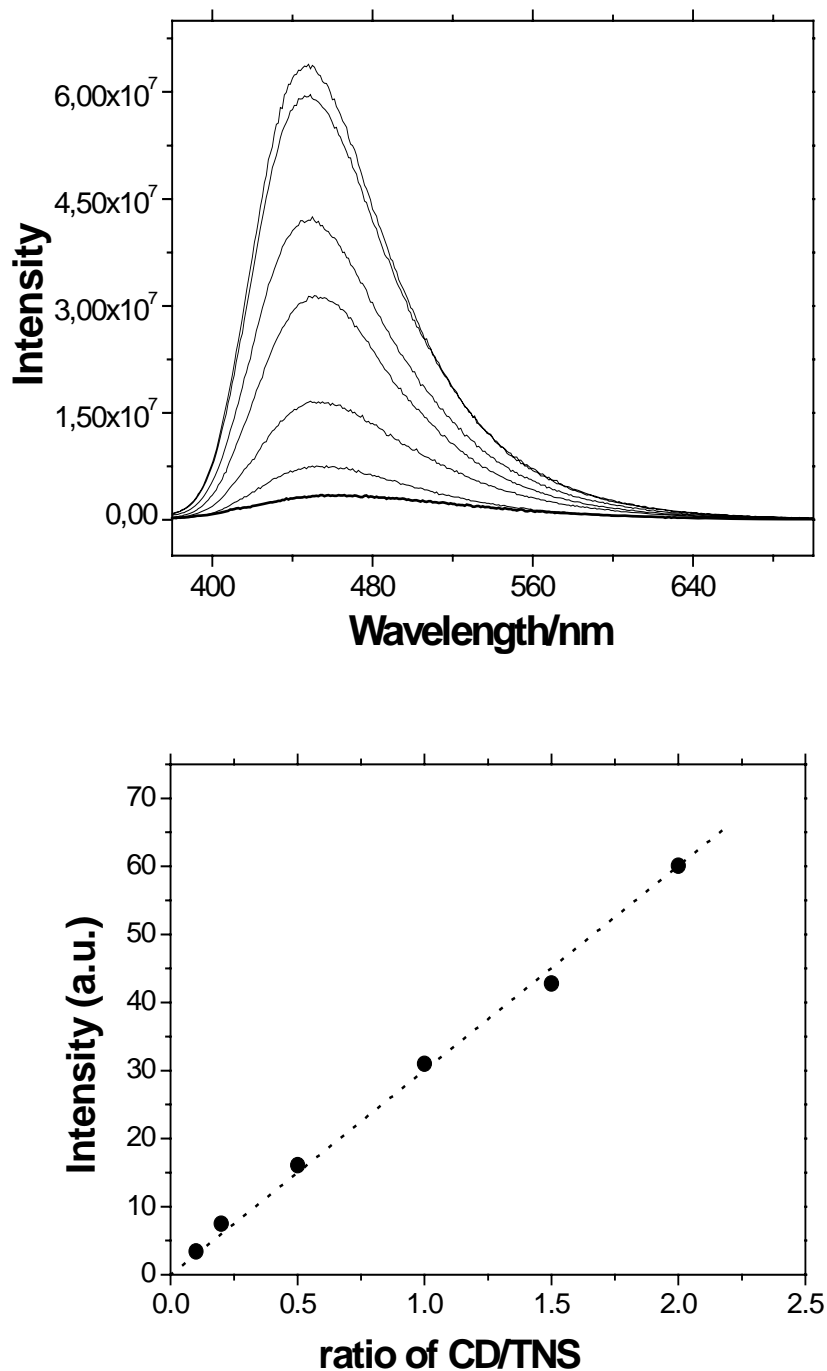


Figure 7.2.2: Fluorescence emission spectra of CD-TNS-complexes at various CD concentrations (top), and corresponding calibration curve used to determine the unknown amount of CD in the supernatant fluid after phase transfer of the nanocrystals (bottom).

Here, it should be noted that the complexation of hydrocarbon chains by cyclodextrin molecules as suggested here (Figure 7.2.3) has also been reported elsewhere. ^[217, 221] Therefore, to our opinion the scenario depicted in the figure 7.2.3 seems not only to agree with our experimental data, but also is agreement with other investigation.

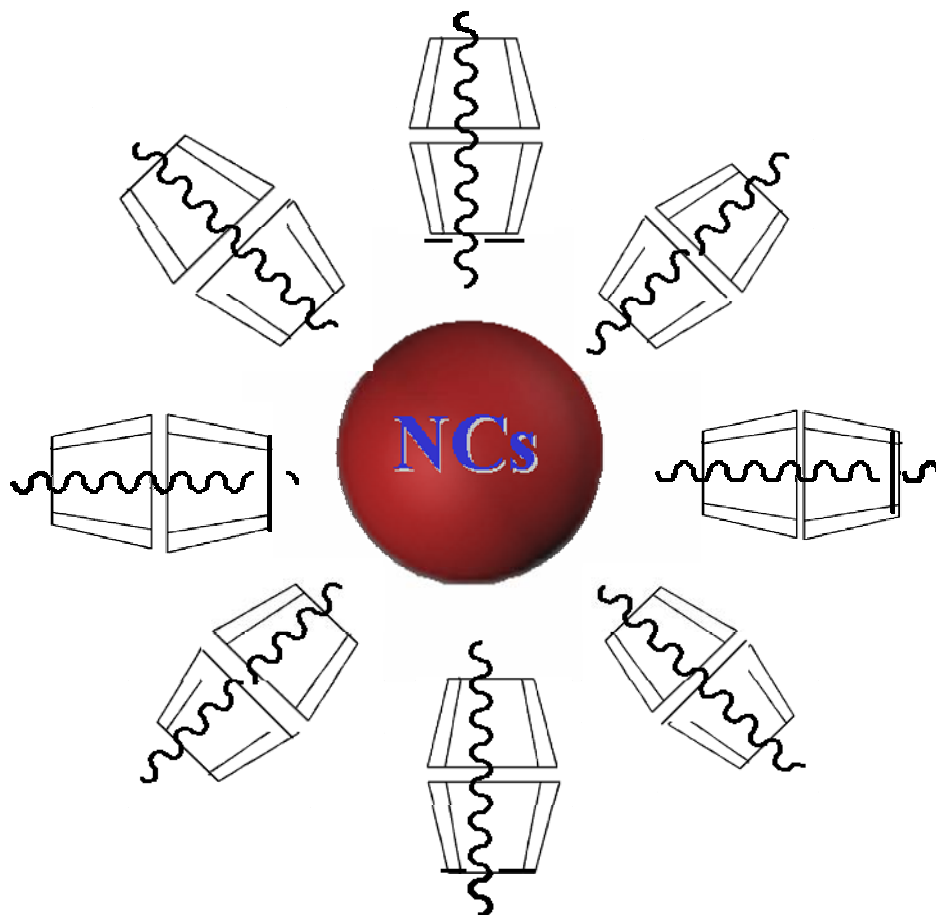


Figure 7.2.3: Scheme of the arrangement of ligand molecules (β -cyclodextrins) around a multi-shell nanocrystal, leading to hydrophilic nanoparticles

Importantly, the water-soluble nanocrystals, although carrying CD molecules at their surface, in contrast to pure CD solutions show no enhancement of fluorescence intensity if mixed with a TNS solution (see absorption peak at 400-500 nm in figure 7.2.4). This indicates that the CD molecules attached to the nanocrystals seem no longer to be capable of complexing host molecules like TNS, and therefore also confirms our assumption that the CD molecules are complexing the hydrocarbon chains of the oleyl amine/oleic acid ligands still remaining on the nanocrystal surface.

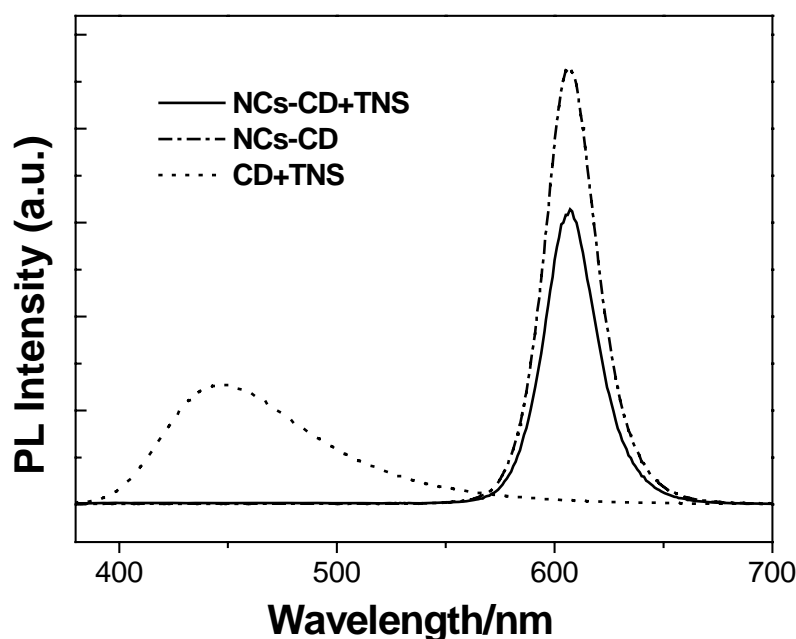


Figure 7.2.4: Fluorescence emission spectra of water-soluble nanocrystals, showing no enhanced fluorescence of TNS, in contrast to pure CD. Excitation wavelength was 370 nm in all cases.

Since the CD molecules seem not to completely replace the oleylamine/oleic acid ligands at the nanocrystal surface as originally intended by us, but rather to complex the hydrocarbon chains, one might conclude that the amino groups of the CD molecules are not important for the ligand exchange. However, ordinary CD molecules without amino functions led to a turbid aqueous phase under identical phase transfer conditions (see experimental part). This indicates the formation of larger nanocrystal aggregates than obtained in case of phase transfer using peramino CD, in which case a clear aqueous solution was obtained. In addition, the nanocrystals stabilized with ordinary CD were not stable but precipitated from aqueous solution within several days.

Next, let us consider the average size of the nanocrystals in organic and in aqueous solution, as determined by dynamic light scattering and visualized by TEM: the nanocrystals in chloroform are single particles of radius about 3.7 nm and, according to a DLS 2nd cumulant analysis as well as the single exponential decay of the time-intensity autocorrelation function (see Figure 7.2.5), are extremely monodisperse. On the other hand, the aqueous nanocrystals obtained after phase transfer

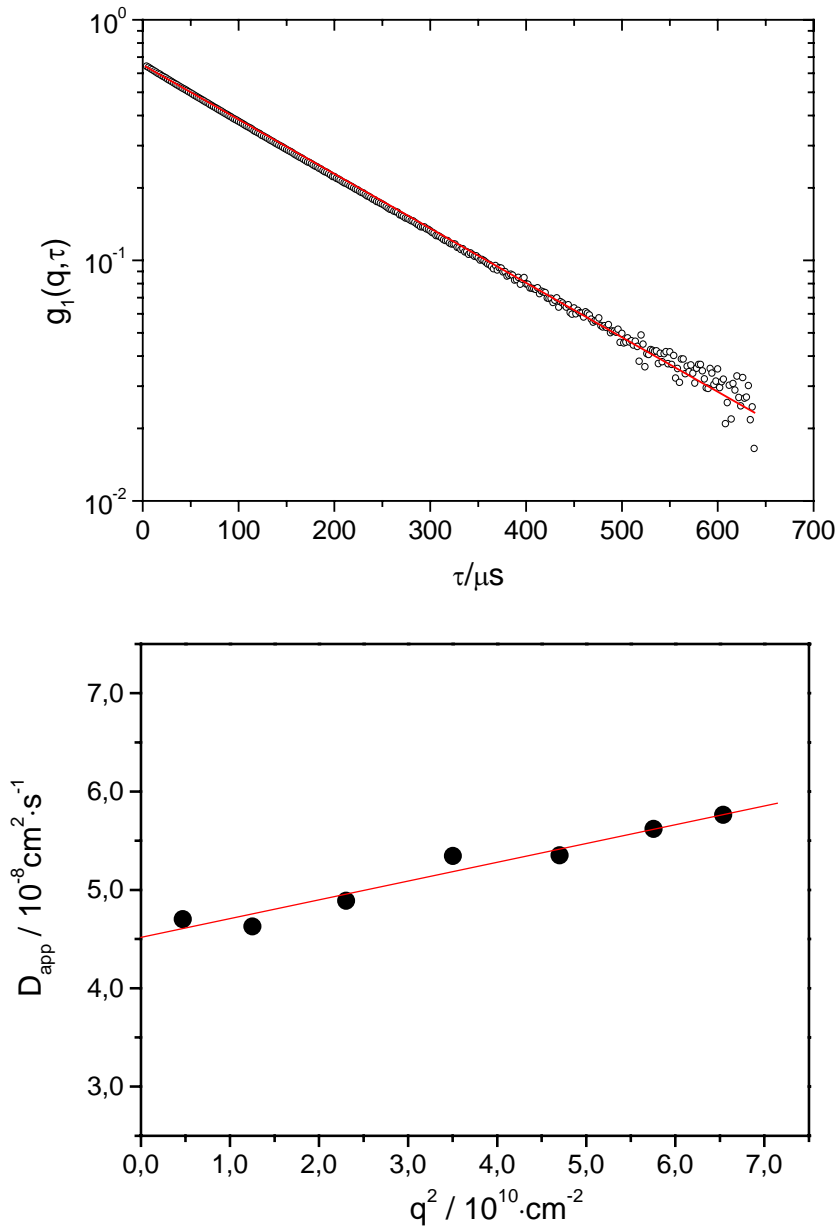


Figure 7.2.5: Single exponentially decaying time intensity autocorrelation function for hydrophobic nanocrystals in chloroform, measured by dynamic light scattering (DLS) at scattering angle 30° (top). Dependence of apparent selfdiffusion coefficient on scattering vector q^2 as measured by DLS of hydrophilic nanocrystals in water at $\text{pH} = 14$, showing the large size polydispersity (bottom).

exhibit a comparatively large average radius of about 45 nm, and a considerable size polydispersity much larger than 30%. The latter has been estimated from a biexponential fit to the time-intensity autocorrelation function as well as the dependence of the average self-diffusion coefficient (and, correspondingly, hydrodynamic particle radius) on scattering angle, as also shown in figure 7.2.5: here,

we should mention that the average size of the water-soluble nanocrystals increased, according to dynamic light scattering, from about 45 nm at pH = 14 to more than 80 nm at pH = 7, showing that particle clusters tend to grow and the aqueous nanocrystal solution becomes less stable with decreasing pH. At pH < 6, finally, the particles start to form even larger aggregates and precipitate within several hours.

Our light scattering results show that, as reported already by Pellegrino et al.^[127], after phase transfer into aqueous solution the nanocrystals form a considerable amount of small aggregates even at higher pH-values. Importantly, according to repeated light scattering measurements the aqueous nanocrystal dispersion at given pH = 12 showed no further growth of aggregates but remained stable for several months. This indicates that the aggregates are formed directly during the phase transfer step. Careful optimization of the phase transfer conditions, using for instance dialysis and/or ultrasonication, therefore might suppress the formation of aggregates and lead to an aqueous solution of single hydrophilic nanocrystals. This is supported also by another system of hydrophilic nanocrystals prepared in our group: using lipoic acid as a hydrophilic exchange ligand for the hydrophobic ligand (oleic acid or oleyl amine), an aqueous solution of nanocrystals of average size 45 nm as determined by dynamic light scattering had been obtained, showing that the aggregate formation seems to be a general phenomenon independent of the ligand molecules or mechanism of ligand exchange, but depending mainly on the experimental protocol of the phase transfer procedure itself. The quantum yield of these lipoic acid stabilized particles was much lower than that of the CD system. Also, the nanoparticles stabilized with lipoic acid exhibited a lower stability and precipitated from aqueous solution within several days if oxygen is present and the sample is kept at daylight.

Finally, we have visualized the structure of our hydrophobic and hydrophilic nanocrystals by transmission electron microscopy. TEM pictures obtained from nanocrystal solutions after solvent evaporation shown in figure 7.2.6 also support the formation of small clusters of nanoparticles after phase transfer into the aqueous phase. The aqueous solution used to prepare the sample shown in figure 7.2.6 was a highly dilute solution, in which case upon drying single isolated particles in the TEM images are to be expected. We believe that the small aggregates seen in the figure correspond to aggregates formed during the phase transfer step. In case of the

hydrophobic sample, on the other hand, evaporation of the solvent chloroform lead to the formation of large 2D-superlattice, whereas in solution nanocrystals are present as single spherical nanoparticles as proven by light scattering (see above).

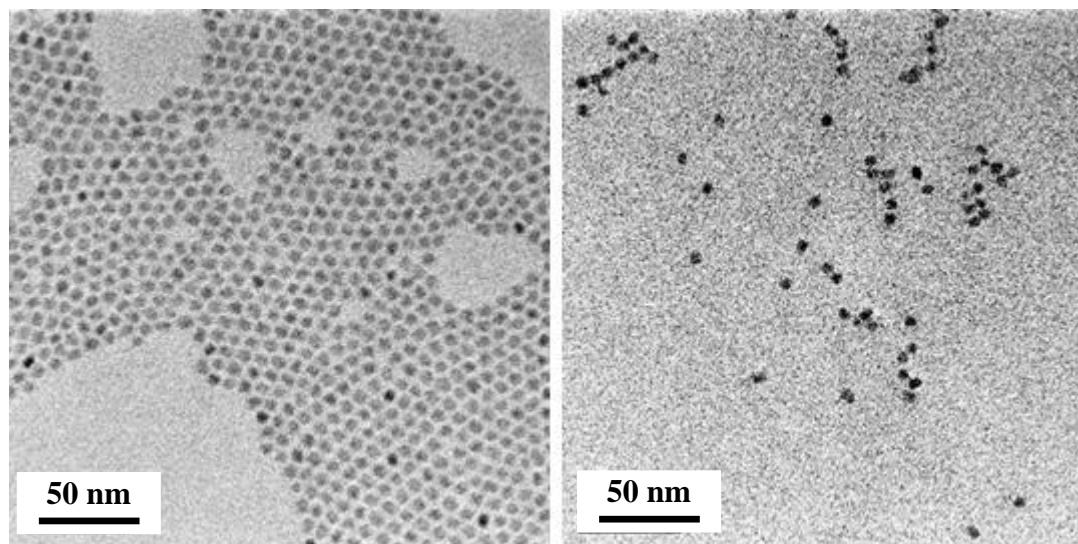


Figure 7.2.6: TEM image of hydrophobic nanocrystals cast from CHCl_3 -solution (left), and image of hydrophilic nanocrystals cast from aqueous solution at pH 14 (right).

7.2.2.2 Optical properties of water-soluble multi-shell nanocrystals

A) Effects of irradiation and environment on quantum yield:

Immediately after phase transfer into water at pH = 14, our nanocrystals already show a remarkable high quantum yield > 40% as determined by direct comparison with a fluorescent standard dye. After exposure of the aqueous nanocrystal solution, stored under an oxygen gas atmosphere after bubbling for 5 minutes with oxygen, to room light for several days, the quantum yield reaches an astonishing 75% (see Figure 7.2.7). To explore which parameters cause this strong enhancement of photoluminescence, we have investigated the influence of various conditions on the quantum yield of our hydrophilic quantum dots in more detail. In all cases, the respective gas atmosphere has been adjusted by 5 minutes bubbling of the aqueous solution with the pure gas and then sealing the sample, before irradiation with strong UV-light or room light respectively. For UV-irradiation, we used an HBO-50 ultraviolet lamp as in our previous photooxidation experiments of hydrophobic multi-shell nanocrystals (see chapter 4).^[165] Alternatively, samples were

exposed to daylight by leaving them within a sealed but uncovered glass vial on the lab bench for several days.

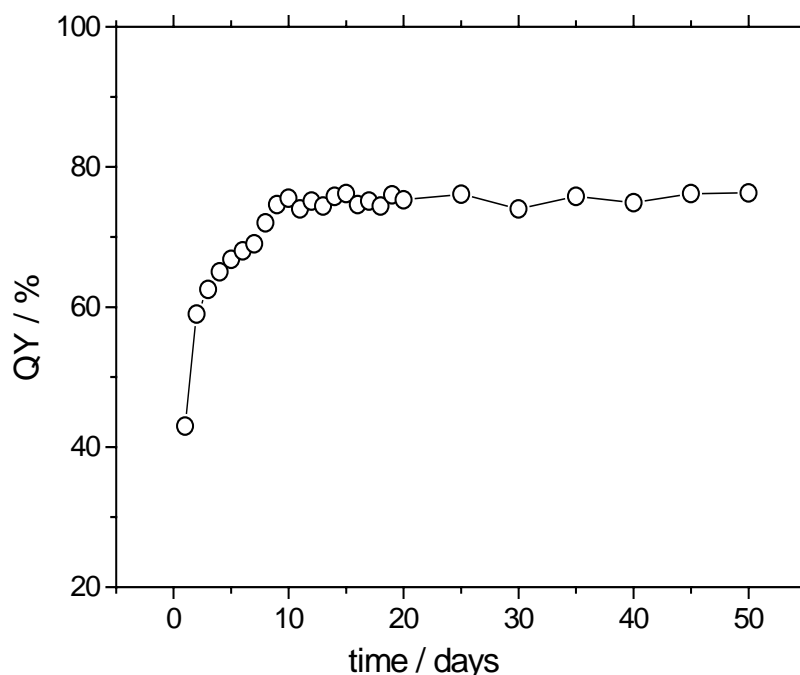


Figure 7.2.7: Quantum yield versus exposure time for an aqueous nanocrystal solution at $pH = 14$ under oxygen atmosphere exposed to daylight

(i) Irradiation with UV-light

Figure 7.2.8 shows the influence of continuous irradiation with strong UV-light on the photoluminescence of hydrophilic nanoparticles in aqueous solution, stored under argon and under oxygen atmosphere, respectively. For comparison, our previous photooxidation studies on hydrophobic multi-shell nanocrystals in chloroform^[165] have also been included. Unexpectedly, hydrophilic particles under an atmosphere of the inert gas argon showed the strongest decrease in photoluminescence at UV-irradiation, whereas the QY of hydrophilic nanoparticles stored under oxygen nearly remains unchanged after UV-irradiation for 20 hours. The hydrophilic particles, therefore, show no degradation due to photooxidation but rather a passivation in case oxygen is present during UV-irradiation. Also, it should be noted that the decrease in photoluminescence for the aqueous system stored under argon is much stronger than in case of the photooxidation of the hydrophobic system.

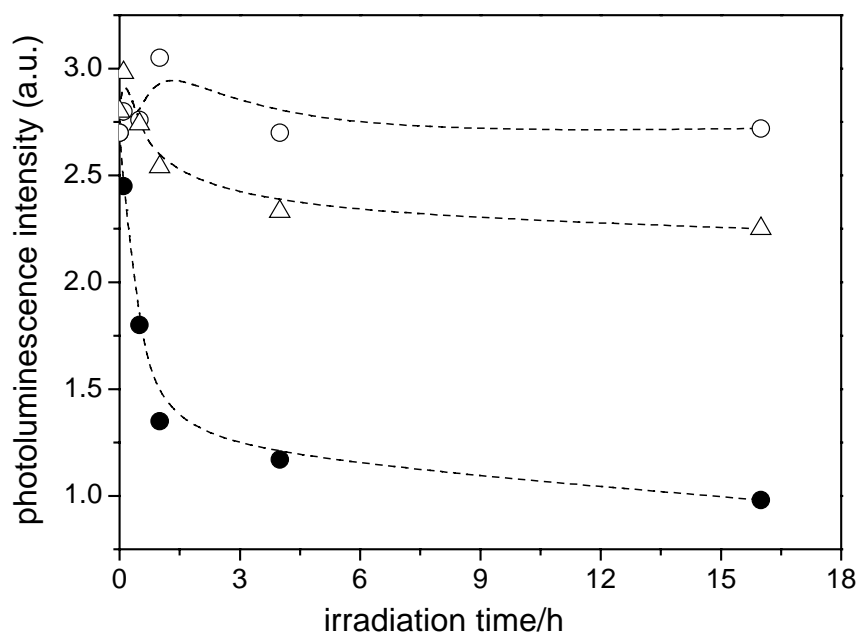


Figure 7.2.8: Influence of continued UV-irradiation on photoluminescence for aqueous solutions ($pH = 14$) of nanocrystals under oxygen (open circles) and argon atmosphere (filled circles), and for chloroform solutions under oxygen (open triangles, from ref.^[165], see also figure 4.14). Dashed lines are guides to the eye.

Finally, we should mention that for the aqueous system stored under argon, if UV-irradiation is stopped after 1 hour and the sample kept in the dark, the photoluminescence fully recovers within several hours. Longer UV-irradiation, however, led to irreversible destruction of the nanocrystals also shown by a pronounced broadening of the photoluminescence emission peak.

(ii) Exposure to room light

If the samples are exposed to daylight, in contrast to the UV-irradiation results the photoluminescence is not decreasing but increasing, as shown in figure 7.2.9. Again, oxygen seems to play an important role, since the effect is much more pronounced in case of an oxygen atmosphere compared to an argon atmosphere. For the latter, the effect of photoactivation found after daylight exposure for 2-3 days nearly decays completely at longer exposure. In conclusion, we interpret this effect as a combination of the photoactivation process well-known for nanocrystals comparable to our system ^[160, 222], and a passivation or protection of the nanocrystals from

photodegradation in aqueous environment at high pH values in the presence of oxygen.

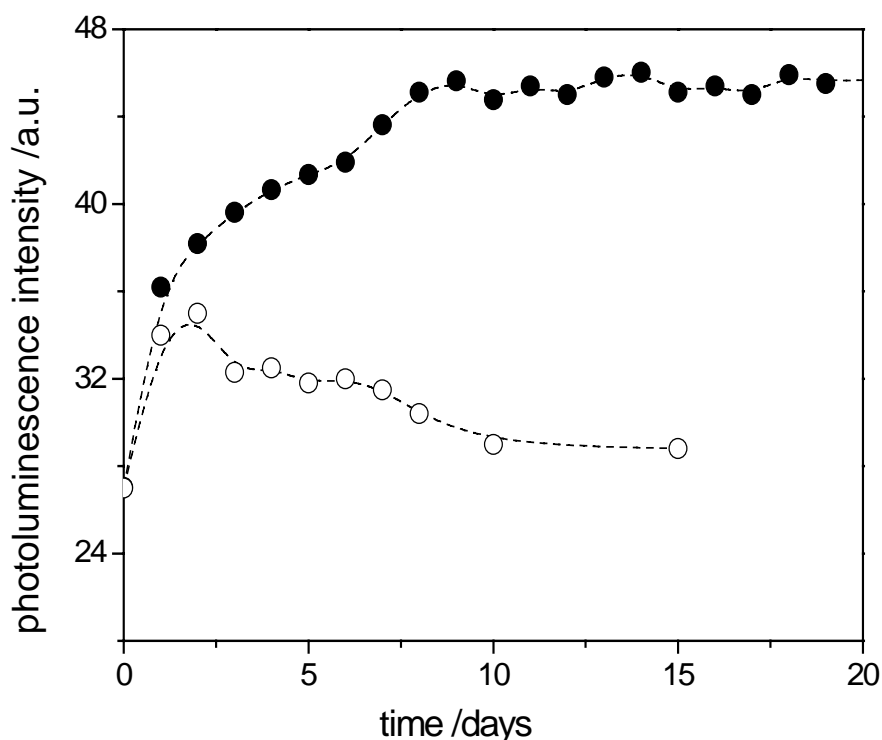


Figure 7.2.9: Influence of continued exposure to daylight on photoluminescence of aqueous solutions of nanocrystals at pH = 14 under oxygen (filled circles) and argon atmospheres (open circles). Dashed lines are guides to the eye only.

B) Quantum yield and pH

After changing the pH of the aqueous solution containing our photoactivated nanocrystals by adding acetic acid, the quantum yield drops dramatically from 75 % (see Figure 7.2.6) to less than 10 %. This dependence of quantum yield on pH is shown in figure 7.2.10. At present, we have no suitable explanation for this unusual behaviour of our aqueous nanocrystal system. We suspect the amino groups of the cyclodextrin molecules may play an important role, since phase transfer using ordinary cyclodextrin molecules leads to an aqueous system with much lower stability. Another possibility is a change of the surface charge, which is an important factor determining the quantum yield of the nanocrystals. This effect has been reported in the literature.^[120]

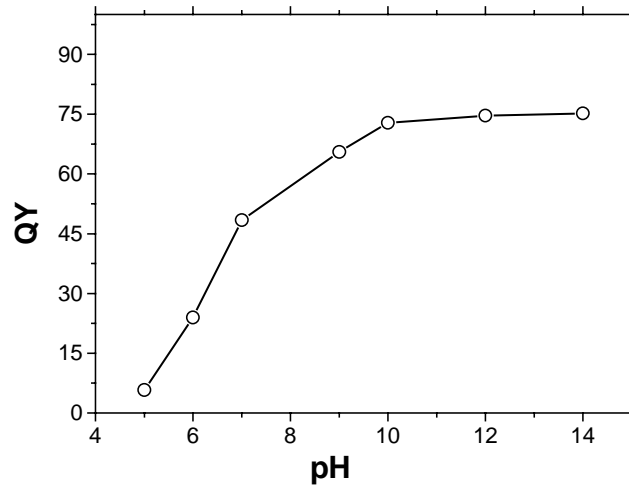


Figure 7.2.10: Variation of the quantum yield with the pH of an aqueous nanocrystal solution

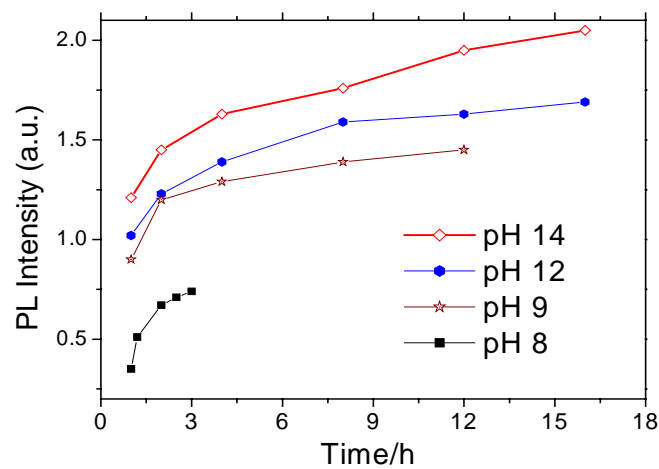
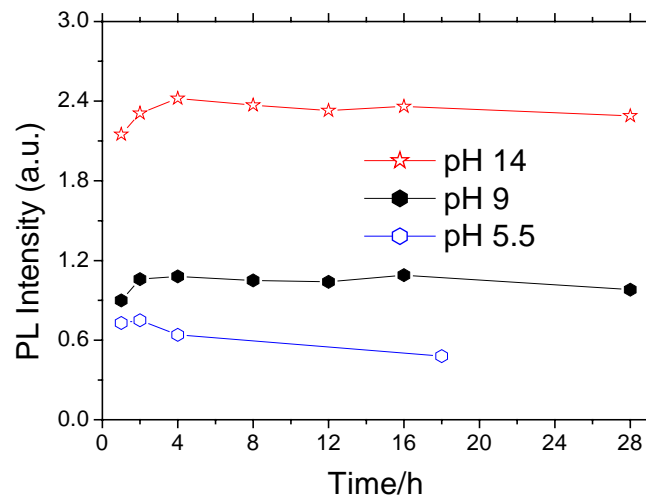


Figure 7.2.11 Variation of the quantum yield of the aqueous nanocrystal solutions at different pH values for samples stored under the dark (top) and at room light (bottom).

For comparison, we have investigated the influence of light on the quantum yield of our hydrophilic nanocrystals at different pH values in more detail. In all cases, samples were put under room light or stored in the dark, respectively. The gas atmosphere of the sample solutions was simply air (see Figure 7.2.11). Likewise, these experimental results indicate that the quantum yield of our new hydrophilic nanocrystals can be improved if the sample is kept at room light. On the other hand, the quantum efficiency remains constant for samples stored in the dark. Importantly, the quantum yields of low pH samples are still lower than those of high pH samples under the same experimental conditions (daylight or dark).

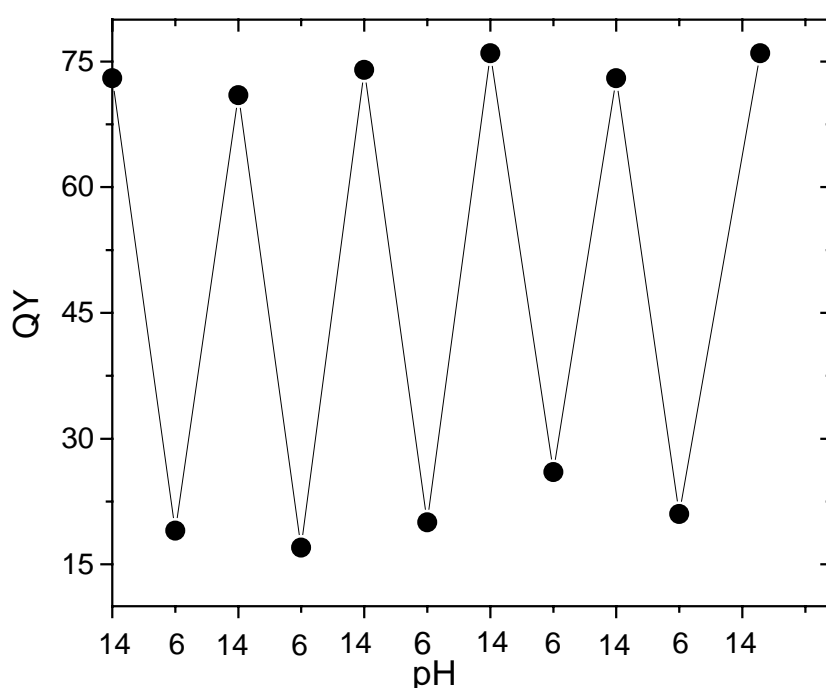


Figure 7.2.12: Reversible recovery of the quantum yield upon repeatedly changing the pH of the aqueous nanocrystal solution (by subsequent dilution) between pH = 6 and pH = 14

Interestingly and importantly, this dependence of quantum yield on pH is perfectly reversible, as shown in figure 7.2.12. Also, the structure of the nanocrystals, that is the average size of the aggregates and size polydispersity in solution, does not change after several pH cycles, as verified by TEM and dynamic light scattering. Here, it should be noted that whereas our aqueous nanocrystals at pH > 12 are stable for many months as already mentioned before, at pH < 10 the aqueous solution is stable for several days only, and at pH < 6 the nanocrystals precipitate rapidly within a few hours. The strong and reproducible dependence of quantum yield on pH makes our new system a nice sensor to measure the pH of an aqueous environment.

7.2.2.3 Conclusion

A new system of water soluble quantum dots based on peramino β -cyclodextrin has been presented. The nanocrystals have a high fluorescence quantum yield and are stable in aqueous solution for several months. The fact that the quantum yield strongly varies with the pH of the aqueous solution makes our new particles a nice sensor system. At present, our nanocrystals still tend to form small aggregates after phase transfer from organic to aqueous solution, a problem which has been encountered by other research groups before. However, these very small aggregates of size < 100 nm seem to have no negative influence on either the excellent optical properties nor on the high solution stability of our new hydrophilic nanocrystals.

In recent experiments, it was tried to reproduce the results presented before using different batches of peramino β -cyclodextrin. However, the yield of the CD-nanocrystal complex is low ($\sim 10\%$). In addition, the CD-nanocrystal complexes usually showed strong aggregation, rendering them insoluble in water. This means that the system is very sensitive to the quality of peramino β -cyclodextrin.

7.2.3 Aminoethanethiol (AET)

7.2.3.1 Transfer into the aqueous phase

As mentioned above, colloidal nanocrystals have unique optical and spectroscopic properties that possess several inherent advantages over organic dyes and can offer a compelling alternative to traditional fluorophores in several fluorescence-based assay applications, such as Förster resonance energy transfer (FRET). The broad absorption spectra of nanocrystals should allow flexibility in choosing the desired excitation wavelength in FRET studies. Importantly, nanocrystals have photoluminescence quantum yields comparable to those of organic dyes.

Here, we will describe the synthesis of water soluble multi-shell nanocrystals which were prepared as described in chapter 4. Because of the synthesis, the particles are initially covered with oleic acid/oleylamine and therefore are soluble in chloroform. These particles can be transferred from chloroform into water phase via attachment of aminoethanethiol (AET) as shown in figure 7.2.13. The thiols replace the ligands (oleic acid/oleylamine) of the multi-shell nanocrystals at the nanocrystal surface and the protonated positively charged amino functions provide the solubility of the nanocrystals in water.

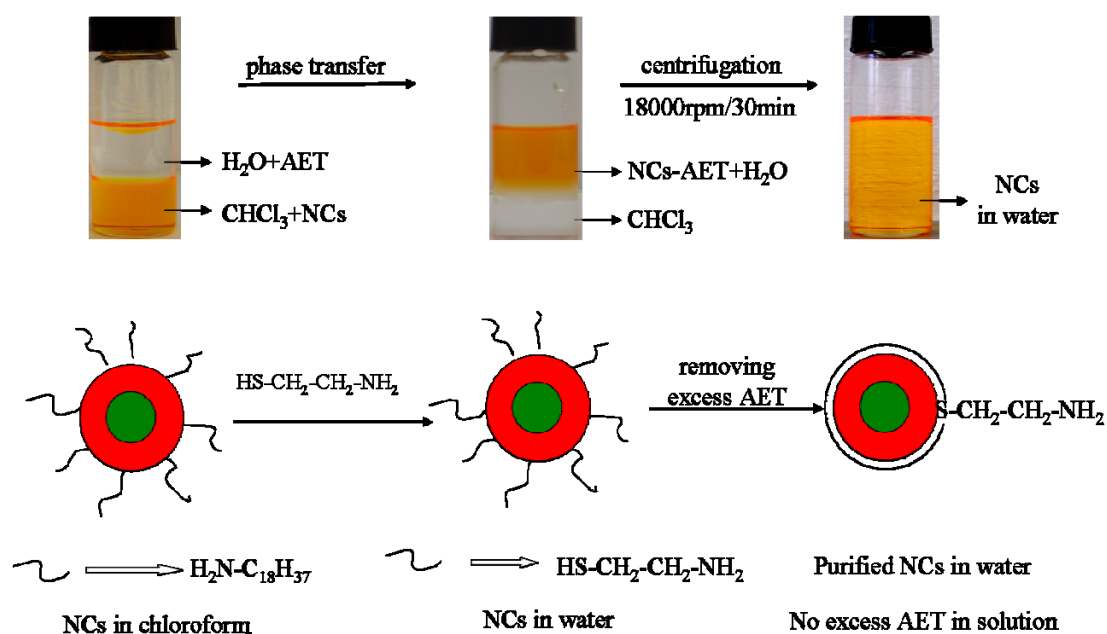


Figure 7.2.13 Synthetic approach towards AET functionalized nanocrystals by phase transfer of hydrophobic precursor nanocrystals.

7.2.3.2 Coupling to Cy5-dye molecules

In this section, we will describe the preparation of a FRET complex using nanocrystals as donors and organic dye molecules as acceptors. A cyanine dye (Cy5) serves as the energy acceptor after the formation of a nanocrystal-dye complex. In figure 7.2.14, it is seen that the surface of the nanocrystals after the ligand exchange carries a reactive amino group. Therefore, Cy5 molecules used as FRET acceptors and functionalized by succinimide could be attached to the surface of the nanocrystals by amide bonds as shown in figure 7.2.14. (see preparation method section)

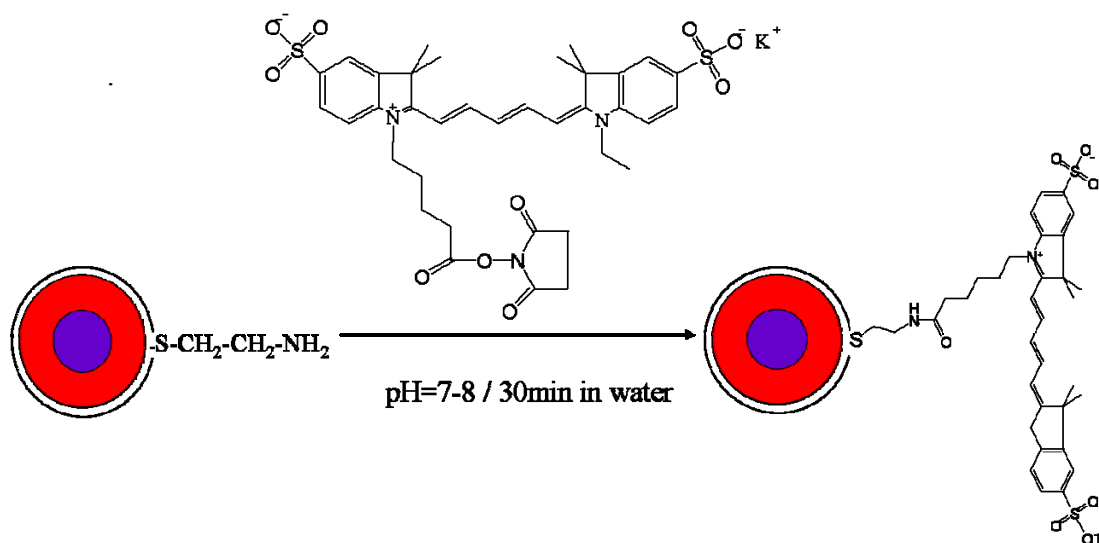


Figure 7.2.14 Schematic preparation of the nanocrystal-dye complex

A very important characteristic of a donor-acceptor pair is its Förster radius. [223] The Förster radius R_0 is the distance between the donor and the acceptor at which the rate of the nonradiative energy transfer rate is equal to the radiative rate of the donor. For a single donor and acceptor separated by a fixed distance the Förster radius is given by [224]

$$R_0^6 = \frac{9000(\ln 10)\kappa^2 Q_D}{128\pi^5 N_a n^4} \int_0^{\infty} F_D(\lambda) \varepsilon_A(\lambda) \lambda^4 d\lambda \quad (7.1)$$

where Q_D is the fluorescence quantum yield of the donor alone, N_a is the Avogadro number, n is the refractive index of the medium, $F_D(\lambda)$ is the normalized fluorescence intensity of the donor, and $\varepsilon_A(\lambda)$ is the extinction coefficient of the acceptor. [

$F_D(\lambda)\epsilon_A(\lambda) \lambda^4 d \lambda$ is the overlap integral, which expresses the degree of the spectral overlap between the donor emission and the acceptor absorption. The Förster mechanism of energy transfer requires a non-zero orientation factor $\kappa \neq 0$ and a significant overlap of the acceptor absorption spectrum with the donor's fluorescence spectrum. For real systems, consisting of many donor-acceptor pairs in which case molecular orientations are randomized by rotational diffusion prior to the energy transfer, the orientation factor is assumed as $\kappa^2 = 2/3$.

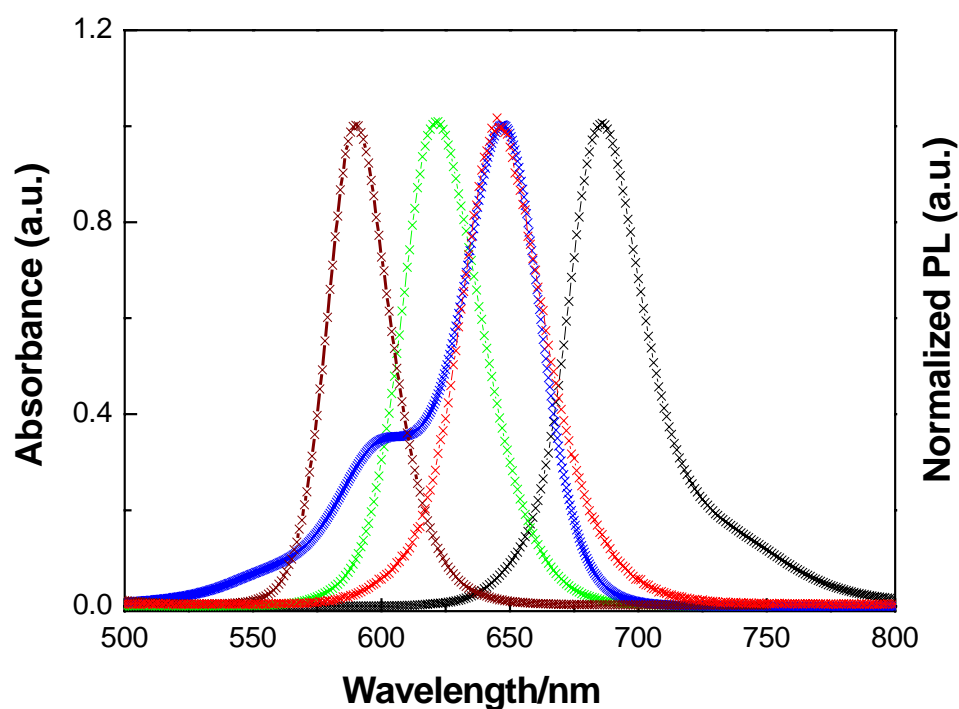


Figure 7.2.15 Normalized absorption (blue) and emission spectra (black) of Cy5 and photoemission spectra of the three multi-shell nanocrystal solutions. Dark purple: Nanocrystals with PL maximum at 590 nm. Green: Nanocrystals with PL maximum at 622 nm. Red: Nanocrystals with PL maximum at 645 nm.

Figure 7.2.15 shows the absorption spectrum of the Cy5 dye and the emission spectra of three nanocrystal solutions (spectra are normalized). Table 7.3 shows the calculated overlap integrals and Förster distances (R_0) for different nanocrystal-dye pairs using equation 7.1 and the experimental values for Q_D , and a value of $2/3$ for κ^2 . In fact, it is difficult to define the accurate molecular distance from the core to center of the dye molecule due to the flexible chain between nanocrystal and dye, although the Förster distances (R_0) of these systems can be obtained as shown in table 7.3

Table 7.3 Overlap integrals, quantum yields, and calculated Förster distances for nanocrystal-Cy5 pairs

Donor-acceptor pair	Overlap integral. $\times 10^{15} \text{J/Lmol}^{-1} \text{cm}^{-1} \text{nm}^4$	Quantum yield Q_D	Förster distance $R_0(\text{Å})$
590-Cy5	7.05	0.3	59
622-Cy5	12.6	0.4	63
645-Cy5	27.4	0.2	67

Figure 7.2.16 (A-C) shows the photoluminescence spectra of the nanocrystal donor-Cy5 dye acceptor complex for different dye-nanocrystal ratios for each of the three nanocrystal samples used. It should be noted that the photoluminescence signal was obtained in the mixed solutions (nanocrystal solution and dye solution). We have found that these nanocrystal-dye complexes are not stable. On one hand, the Cy5 dye itself will decompose after 1 day. On the other hand, the complexes will precipitate out of aqueous solution after 1 hour. Therefore, the spectra (Figure 7.2.16) were measured immediately after adding the dye into nanocrystal solutions (10 min.). We found that the PL intensity from both nanocrystals and dye was varying with time (not shown here). Therefore, we assume that the solubility of the nanocrystal-dye complexes is low. The experiments in which the complexes were precipitated and redispersed indicate that these complexes could not be dissolved in other solvents such as methanol, water, DMF, THF, DMSO and ethanol.

Based on the problems described above, it is difficult to calculate the exact energy transfer efficiency of these systems due to the instability of the complexes. Therefore, the energy transfer efficiency of these systems was not shown in this thesis. However, it can be seen that the energy transfer from the donor (nanocrystal) to the acceptor (Cy5) took place. A progressive quenching of the nanocrystal emission and a systematic enhancement of the Cy5 emission was observed as the average number of dyes surrounding the nanocrystals increased from 10 to 60. In addition, we found that the variation of relative PL intensities with dye concentration for the three sets of nanocrystal-dye complexes using nanocrystals of different size as shown in figure 7.2.16 was not identical due to different values of overlap between donors and acceptors. This indicates a different energy transfer efficiency of these systems.

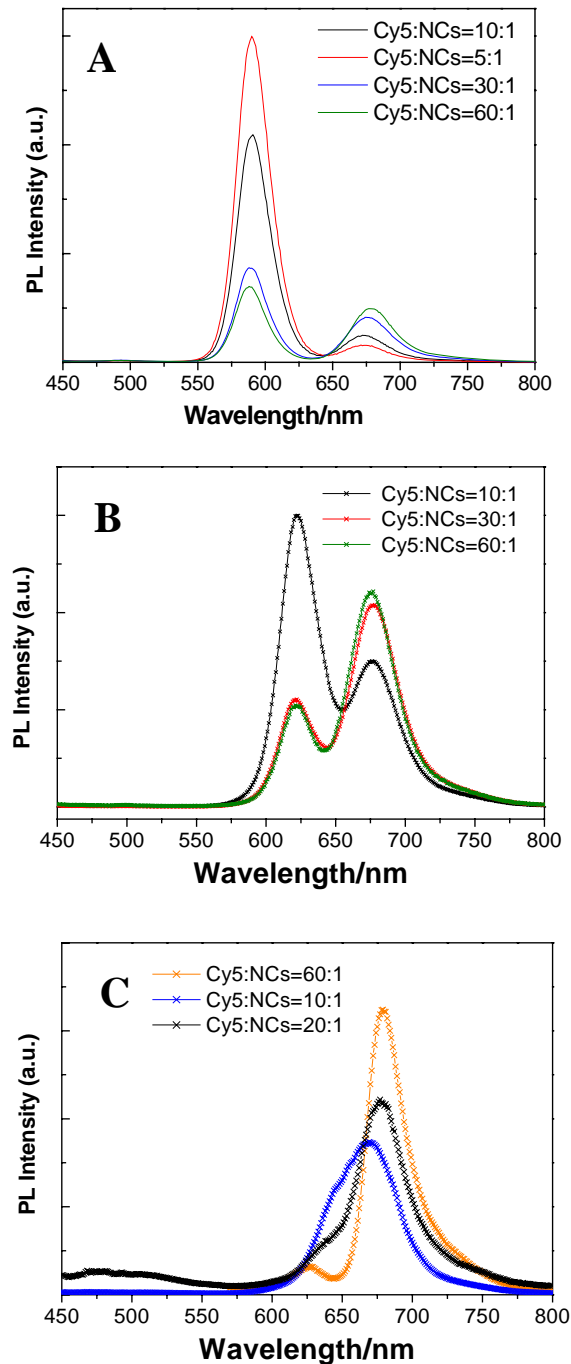


Figure 7.2.16 Evolution of the photoluminescence spectra for the nanocrystal-Cy5 complex for different ratios of Cy5: nanocrystals. (A): nanocrystals with PL maximum at 590 nm. (B): nanocrystals with PL maximum at 622 nm. (C): nanocrystals PL maximum at 645 nm.

The FRET efficiency can be measured experimentally and is commonly defined as: $E = 1 - F_{DA}/F_D$, where F_{DA} is the integrated fluorescence intensity of the donor in the presence of the acceptor and F_D is the integrated fluorescence intensity of the donor alone. In fact, for the calculation of the energy transfer efficiency, an

accurate value of the ratio of the nanocrystal and the dye is a prerequisite. Some additional parameters also have to be determined for the calculation of the energy transfer efficiency, such as the stability of the donor-acceptor pair and the photoluminescence life time.

7.3 Calixarene functionalized nanocrystals

7.3.1 Calixarene with four amine groups (Calix-(NH₂)₄)

In collaboration with the group of Dr. Böhmer (Abteilung für Lehramtskandidaten der Chemie der Johannes-Gutenberg-Universität Mainz), the synthesis of calixarenes suitable for nanocrystal surface modification was performed. Calixarenes were chosen since they should open the possibility to be further functionalized and therefore to serve as anchors for the nanocrystal surface as well as other functionalities (for instance dye markers).

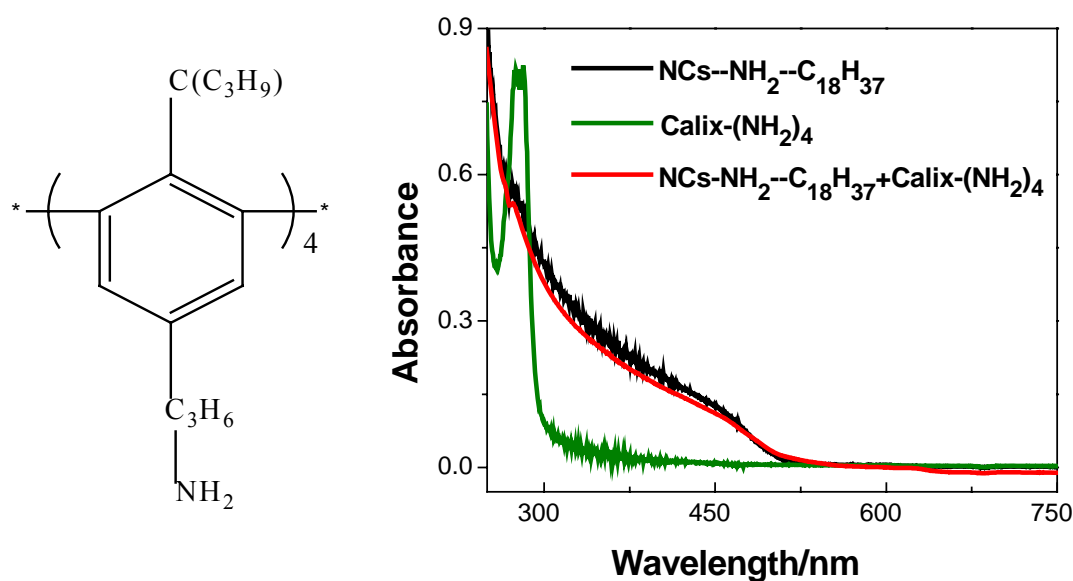


Figure 7.3.1 (left): Structure of a calixarene with four amino groups. (right): Absorption spectra of multi-shell nanocrystals (black), calixarene (green) and the complex after purification of the solution mixture (red).

In case of the hydrophobic calixarene with four amino groups (Calix-(NH₂)₄) shown in Figure 7.3.1 (left), we hoped that we could get a CdSe-Calix-(NH₂)₄ complex by ligand exchange in chloroform. In order to make the Calix-(NH₂)₄ replace the octadecylamine (ODA)/oleic acid ligands, several mixed solutions of Calix-(NH₂)₄ and nanocrystals were stirred at various temperatures from room temperature

to 120 °C for 2 hours. Then the sample was cooled to room temperature, purified by precipitation in methanol or acetone, and re-dispersed into chloroform. Figure 7.3.1 (right) shows the absorption spectra of nanocrystals, Calix-(NH₂)₄ and the purified sample obtained from the mixed solution. A pronounced absorption peak (~270 nm) was observed in case of the pure Calix-(NH₂)₄. However, the sample obtained from the mixed solution after purification did not show the absorption peak of Calix-(NH₂)₄. This experimental result indicates that Calix-(NH₂)₄ did not replace the ODA/oleic acid ligands

Then, we adopted another method as follows: As was shown before, organic ligands such as TOPO or ODA/oleic acid can be replaced by ligands containing a thiol group. Therefore, first MPA was used to replace the ODA/oleic acid ligands, and transfer the nanocrystals into water. Thus a carboxyl group is introduced at the surface of the nanocrystals. Then the complex of nanocrystal-Calix-(NH₂)₄ can be obtained by adding the hydrophobic Calix-(NH₂)₄ into the aqueous nanocrystal solution (phase transfer from chloroform to water), leading to the formation of a peptide bond between MPA and Calix-(NH₂)₄ using the 1-(3-Dimethylaminopropyl)-3-ethylcarbodiimide (EDC).

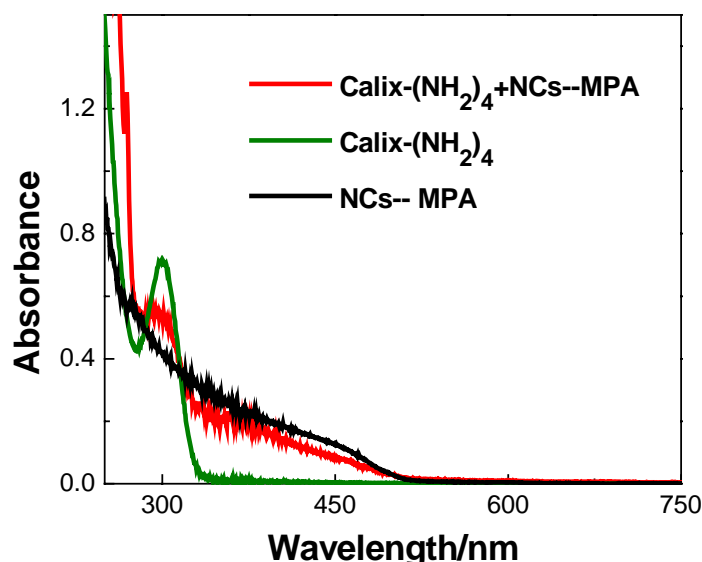


Figure 7.3.2 Absorption spectra of multi-shell nanocrystals in water (black line), calixarene in chloroform (green line) and the complex in chloroform after the purification of solution mixture (red line).

In fact, the successful formation of the desired nanocrystal-Calix-(NH₂)₄ complex using this new approach can be identified, because the water soluble MPA-

nanocrystals could be transferred into organic phase, for example chloroform. The ligand exchange in addition has been verified by UV-Visible spectroscopy as shown in figure 7.3.2: the absorption peak of calixarene was also observed in the purified mixed solutions (red line). Finally, we measured the QY of the complex. We found that this QY with 30% of the original value (nanocrystals in chloroform) is much lower than that of pure nanocrystals in water (QY: 30%) or chloroform (pure nanocrystals: 52%).

7.3.2 Calixarene with four thiol groups (Calix-(SH)₄)

Since it is known that thiols can attach quite strongly onto the surface of nanocrystals, a new calixarene with four thiol groups (Calix-(SH)₄) has been prepared in Dr. Böhmer's group. Both nanocrystals and Calix-(SH)₄ are hydrophobic. Therefore, the ligand exchange reaction was done in one phase similar to that of the nanocrystal-Calix-(NH)₄ system discussed (Figure 7.3.1) before.

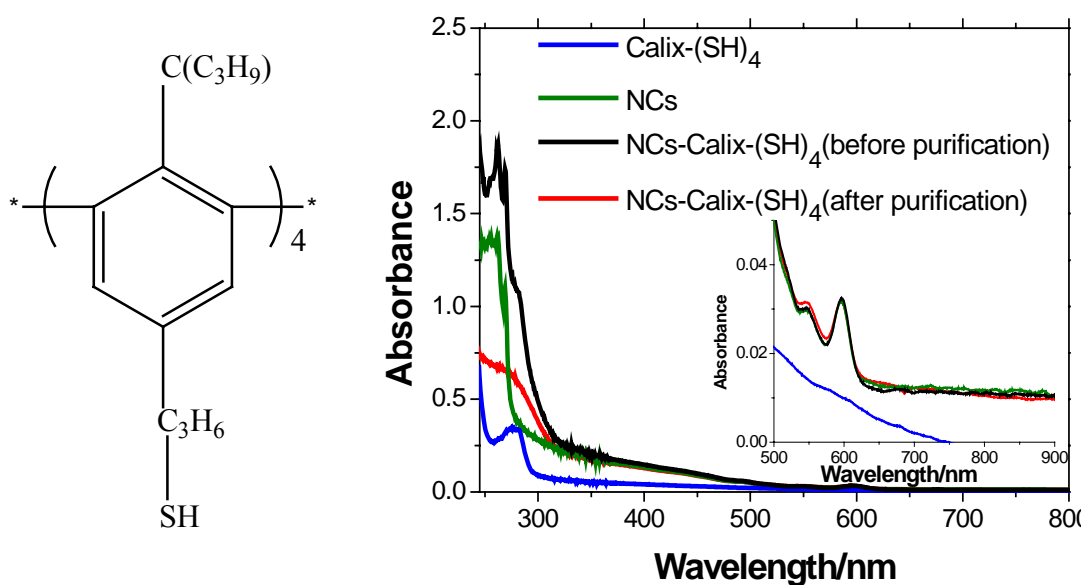


Figure 7.3.3 (left): Structure of a calixarene with four thiol groups (Calix-(SH)₄). (right): Absorption spectra of multi-shell nanocrystals (green line), Calix-(SH)₄ (blue line) and the mixture of nanocrystals and Calix-(SH)₄ before (black line) and after (red line) the purification of the mixed solution.

In order to make the Calix-(SH)₄ replace the ODA/oleic acid ligands, the solution mixture of Calix-(SH)₄ and nanocrystals was stirred at room temperature for 5 hours. Then the solution was purified by precipitation in acetone, and re-dispersed into chloroform. By comparison of the absorption spectra from Calix-(SH)₄, nanocrystals and mixed solutions before and after purification (Figure 7.3.3), it can be

found that the nanocrystal-Calix-(SH)₄ complex after purification shows the absorption peak (~270nm) of Calix-(SH)₄. This means that Calix-(SH)₄ has attached onto the surface of the nanocrystals. The inset in figure 7.3.3 is the magnification of the spectra from 500 nm to 800 nm.

The QY of the complex is lower than that of the original pure multi-shell nanocrystals. Figure 7.3.4 shows the quantum yield versus time for a chloroform solution of the nanocrystal-Calix-(SH)₄ complex exposed to daylight under air. It can be seen that the quantum yield reaches a value of 30% after one month. To explore this phenomenon, the sample was purified again by precipitation with acetone. Then the precipitate was re-dispersed into chloroform. Surprisingly, it is found that no absorption peak of Calix-(SH)₄ was observed in the UV spectra from purified samples exposed to daylight for 25 days. This indicates that the Calix-(SH)₄ ligands have decomposed after irradiation under day light, and this is why the QY of the nanocrystals increased under daylight exposure.

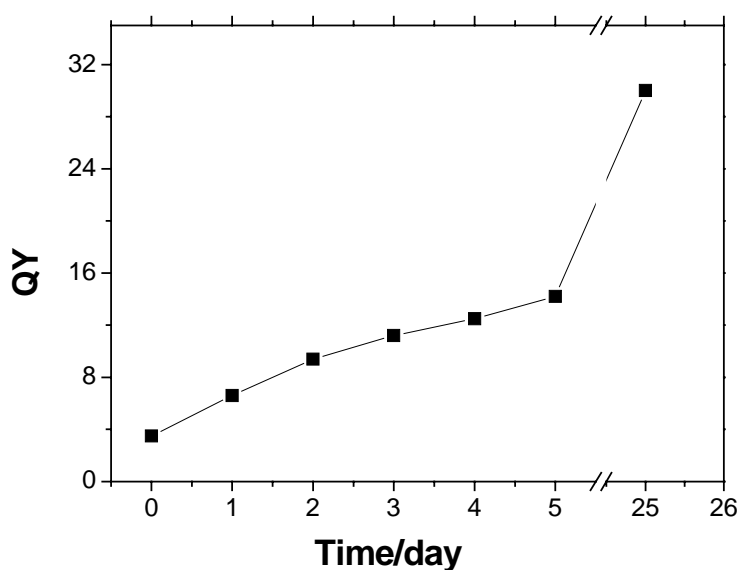


Figure 7.3.4. Quantum yield versus time for nanocrystal-Calix-(SH)₄ complexes in chloroform exposed to daylight

In this section, a new system of hydrophobic nanocrystals based on Calix-(SH)₄ and (Calix-(NH₂)₄) has been presented. These complexes of nanocrystal-calixarene showed a low quantum yield, and the complex of nanocrystal-Calix-(SH)₄ is not stable if exposed to daylight. Nevertheless, we hope that this complex could be used for further applications: for example, the complex can be used as donor in a FRET

system since the distance between the nanocrystal and the acceptor dye can be well controlled by means of the structure of calixarene.

7.4 Preparation Methods

A) Cyclodextrin

Peramino- β -cyclodextrin has been prepared as described in detail elsewhere [215, 216]. This compound is dissolved in an aqueous solution of tetramethyl ammonium hydroxide adjusted to pH 12-14. The solution is mixed with a chloroform solution of oleic acid/oleylamine coated hydrophobic multi-shell nanocrystals. Successful phase transfer is verified by the fact that the original orange color of the organic phase totally disappears, and instead the aqueous phase is becoming colored (orange). Typically, 2 ml of the chloroform nanocrystal solution (concentration: 5×10^{-6} mol L⁻¹) and 2 ml of the aqueous solution of peramino β -cyclodextrin (0.35×10^{-4} mol L⁻¹ - 112×10^{-4} mol L⁻¹, pH adjusted to pH = 12~14 by the addition of (CH₃)₄NOH)) were mixed together in a small glass vessel (15 ml). This mixture was vigorously stirred with magnetic stirrer at room temperature for at least 5 hours. After successful phase transfer, the water soluble nanocrystals were purified as following: 0.5 ml methanol was added to the aqueous solution after the pH had been adjusted to pH = 8 by adding acetic acid. Next, the solution was centrifuged, and the resulting precipitate was redispersed in water at pH = 12~14.

B) Mercaptopropionic acid (MPA)

The MPA-coated multi-shell nanocrystals were synthesized by a phase transfer method [225] in the following manner. The oleylamine/oleic acid-coated nanocrystals were dissolved in about 2 ml of chloroform to give a solution with concentration corresponding to an optical density ~ 0.1 and added under vigorous stirring to the same volume of a water solution containing MPA. The amount of MPA (0.03 ml) was adjusted to be roughly 150% of the total Cd- or Zn-atoms on the particle surface. After 2 hours, the NCs transferred into the water phase but the solution was not optically clear at pH \approx 5-7, possibly due to inter particle hydrogen bonding between the carboxyl-functions of the ligands. To remove excess MPA from the supernatant solution, the particles were separated by centrifugation and

decantation. Redispersion of the particles into water at pH=10.8 yielded a clear solution

C) Aminoethanethiol (AET)

AET-coated multi-shell nanocrystals were synthesized also by the phase transfer method. The oleic acid/ODA-coated multi-shell nanocrystals were dissolved in about 2 ml of chloroform at high concentration ($OD \approx 0.2$) and added to the same volume of an aqueous solution of aminoethanethiol under vigorous stirring. An excess amount of aminoethanethiol was used directly in the reaction. After 2 hours, the nanocrystals were transferred into the water phase yielding a clear solution. This means that aminoethanethiol has attached to the surface of the nanocrystals. Nanocrystals in water were precipitated by adding excess methanol and centrifuged at 18000RPM. Finally, nanocrystals were re-dispersed into water. By this procedure, the excess aminoethanethiol molecules could be removed from solution. The surface of these nanocrystals contains $-NH_2$ groups which can be utilized for further reaction.

D) Nanocrystal-Cy5 complex

The concentration of multi-shell nanocrystals can be calculated by their UV spectra and extinction coefficient. For one nanocrystal, its surface area can be calculated according to the diameter of particles from TEM images. For a 7 nm nanocrystal, therefore, at most 50 Cy5 molecules can attach to the surface. Of course, the actual amount of Cy5 molecules depends also on the concentration of the nanocrystals. Typically, 0.1 ml DMSO (Cy5 concentration: $2 \times 10^{-4} \text{ ML}^{-1}$) was added into the solution of nanocrystals (2ml water: concentration of nanocrystals: $1 \times 10^{-6} \text{ ML}^{-1}$) immediately before the measurement of the PL spectra of the nanocrystal-dye complex (ratio of nanocrystal and dye=1:10). To form the nanocrystal-dye complex, the pH value of the nanocrystal solution was adjusted to 8.5 by adding KOH.

E) Calix-(NH₂)₄-multi-shell nanocrystals complex

The MPA-coated multi-shell nanocrystals were synthesized by a phase transfer method as described above. The surface of these nanocrystals contains $-COOH$ groups, which can be utilized for further reaction with $-NH_2$ groups in presence of EDC. Typically, 2 ml of the chloroform Calix-(NH₂)₄ solution (concentration: $1 \times 10^{-3} \text{ mol L}^{-1}$) and 2 ml of the aqueous solution of MPA coated multi-shell nanocrystals

($\sim 1 \times 10^{-5}$ mol L⁻¹) were mixed together in a small glass vessel. Then ~ 1 mg EDC was added into the water phase. This mixture was vigorously stirred at room temperature for at least 2 hours. Successful phase transfer is verified by the fact that the original orange color of the water phase totally disappears, and instead the organic phase is becoming colored (orange). To remove excess Calix-(NH₂)₄ from the supernatant solution, the nanocrystals were separated by centrifugation and decantation. Redispersion of the particles into chloroform yielded a clear solution.

F) Calix-(SH)₄-multi-shell nanocrystals complex

Calix-(SH)₄-coated multi-shell nanocrystals were synthesized as follows: typically, 10 mg Calix-(SH)₄ was added into 2 ml of chloroform nanocrystal solution (concentration: $\sim 5 \times 10^{-5}$ mol L⁻¹). Then the solution was vigorously stirred at room temperature for 10 hours. To remove excess Calix-(SH)₄, the solution was purified by addition of acetone and the resulting precipitate was redispersed in chloroform.

8 Summary

A synthetic procedure for the production of type-I core/shell nanocrystals with “sandwich” alloyed shells based on the principle of crystal lattice matching has been described in this thesis. A detailed comparative study of core/shell nanocrystals has been presented, in which the surface of CdSe cores was passivated by the shell materials ZnS and CdS or a combination of these materials. While the shell material ZnS leads to a suitable electronic passivation due to the large band offsets with respect to CdSe, the CdSe/ZnS core shell particles are irregular in shape and the fluorescence quantum yield decreases for large shell thicknesses due to lattice imperfections. The shell material CdS on the other hand can grow in an almost epitaxial manner due to the small lattice mismatch, but the electronic passivation is less effective because of relatively small band offsets. To overcome these problems, we have used the SILAR technique to gradually change the shell composition in radial direction from CdS to ZnS. In this way the lattice strain can relax in radial direction and the particles show a high crystallinity. At the same time the band offsets are quite high and the particles are well electronically passivated. These results show that the passivation-shell of semiconductor nanocrystals can be engineered in a defined way leading to particles with high crystallinity, well defined electronic structures and distinct chemical surface properties.

In another set of experiments colloidal type-II core/shell nanocrystals have been synthesized in a one-pot process by alternate addition of precursors (CdO, S, Se or Te) into the crude reaction solution of ZnTe cores. The core/shell particles showed a narrow size distribution, and PL QYs of up to 30 % have been obtained. The importance of a thin shell for achieving high QYs in a type-II structure has been clearly demonstrated. The emission of the particles can be widely tuned from the visible into the near-infrared region (550 nm- 900 nm) by increasing the thickness of the shell materials and by variation of the size ratio of core and shell. In comparison to other NIR emitters like organic dye molecules, the PL QYs of the type-II core/shell particles can reach higher values. In addition, due to the spatial separation of the charge carriers in type-II ZnTe/CdSe nanocrystals, these particles may lend themselves to applications in photoconducting or photovoltaic devices. Furthermore, the synthetic approach presented here opens a versatile route to other type-II core/shell nanocrystals.

Starting from cubic zinc blende seeds with composition ZnE (E = S, Se, Te) a novel synthetic route for growing a variety of complex heterostructures (pyramidal, nail-shaped, tetrapodal, “chess-figure”-shaped) has been realized. In many instances these ZnE/CdSe heterostructures can be obtained with high yield and in uniform shape without the need for further size- and shape -sorting. For the case of ZnTe/CdSe tetrapods a high resolution TEM/EDX investigation has unambiguously shown that four CdSe arms in the hexagonal wurtzite modification are projected from the cubic ZnTe core. It has been found that besides the choice of the cubic seed, the temperature and the injection method of Cd and Se precursors are crucial inputs for determining the actual heterostructure shape. Although the growth of these novel architectures can be precisely controlled, a fundamental understanding of the growth mechanism(s) is still lacking.

In the last part of this thesis solubilisation and ligand exchange protocols have been developed and tested. Along these lines water soluble multi-shell nanocrystals have been obtained by exchanging hydrophobic surface ligands by peramino β -cyclodextrin. The corresponding nanoparticles have a high fluorescence quantum yield which is strongly pH dependent, and are stable in aqueous solution for several months. At present, these hydrophilic nanocrystals still tend to form small aggregates after phase transfer from organic to aqueous solution. Besides inducing ligand exchange through phase transfer, it was also attempted to replace the surface ligands in the organic phase. For this purpose calixarenes containing four thiol groups at the rim have been used. Although these multidentate ligands can replace the original ligands, the resulting complexes are not stable and have a low quantum yield. Nevertheless, such systems could be used for defined FRET couples, since the distance between the nanocrystal and an acceptor dye can be well controlled by the calixarene.

Reference

1. Bawendi, M.G., Steigerwald, M. L., Brus, L. E. , *Annu. Rev. Phys. Chem.*, 1990. **41**: p. 477.
2. Henglein, A., *Chem Rev.*, 1989. **89**: p. 1861.
3. Steigerwald, M.L., Brus, L. E., *Acc. Chem. Res.*, 1990. **23**: p. 183.
4. Weller, H., *Angew. Chem., Int. Ed. Engl.* , 1993. **32**: p. 41.
5. Weller, H., *Adv. Mater.*, 1993. **5**: p. 88.
6. Hagfeldt, A., Grätzel, M. , *Chem. Rev.* , 1995. **95**: p. 45.
7. Fendler, J.H., Meldrum, F. C. , *Adv. Mater.*, 1995. **7**: p. 607.
8. Alivisatos, A.P., *J. Phys. Chem.*, 1996. **100**: p. 13226.
9. Yoffe, A.D., *Adv. Phys.* , 2001. **50**: p. 1.
10. Lee, C.J., Banin, U., Herhold, A. B., Alivisatos, A. P., *Abstr Pap Am Chem S*, 2000. **219**: p. U273.
11. Brus, L., *J. Phys. Chem.*, 1986. **90**: p. 2555.
12. Alivisatos, A.P., *Science*, 1996. **271**: p. 933.
13. Aldana, J., Wang, Y., Peng, X. , *J. Am. Chem. Soc.* 2001, 2001. **123**: p. 8844.
14. Empedocles, S.A., Neuhauser, R., Shimizu, K., Bawendi, M. G., *Adv. Mater.*, 1999. **11**: p. 1243.
15. Heath, J.R., *Acc. Chem. Res.* , 1999. **32**: p. 389.
16. Murray, C.B., Kagan, C. R., Bawendi, M. G. , *Annu. ReV. Mater. Sci.* , 2000. **30**: p. 545.
17. Klimov, V.I., Mikhailovsky, A. A., Xu, S., Malko, A., Hollingsworth, J. A., Leatherdale, C. A., Eisler, H. J., Bawendi, M. G., *Science* 2000. **290**: p. 314.
18. Chan, W.C., Maxwell, D. J., Gao, X., Bailey, R. E., Han, M., Nie, S., *Curr. Opin. Biotechnol.* , 2002. **13**: p. 40.
19. Chan, W.C.W., Nie, S. , *Science* 1998. **281**: p. 2016.
20. Han, M., Gao, X., Su, J. Z., Nie, S. , *Nat. Biotechnol.* , 2001. **19**: p. 631.
21. Bruchez, M., Moronne, M., Gin, P., Weiss, S., Alivisatos, A. P., *Science*, 1998. **281**: p. 2013.
22. Taton, T.A., Mirkin, C. A., Lesinger, R. L. , *Science* 2000. **289**: p. 1757.
23. Finlayson, C.E., Russell, D. M., Ramsdale, C. M., Ginger, D. S., Silva, and G. C., N. C. , *Adv. Funct. Mater.*, 2002. **12**: p. 537.

24. Kazes, M., Lewis, D. Y., Ebenstein, Y., Mokari, T., Banin, U. , *Adv. Mater.*, 2002. **14**: p. 317.
25. Colvin, V.L., Schlamp, M. C., Alivisatos, A. P. , *Nature*, 1994. **370**: p. 354.
26. Coe, S., Woo, W. K., Bawendi, M., Bulovic, V. , *Nature*, 2002. **420**: p. 800.
27. Tessler, N., Medvedev, V., Kazes, M., Kan, S. H., Banin, U. , *Science*, 2002. **295**: p. 1506.
28. Hines, M.A., Guyot-Sionnest, P. , *J. Phys. Chem.*, 1996. **100**: p. 468.
29. Peng, X.G.S., M. C.; Kadavanich, A. V.; Alivisatos, A. P. , *J. Am. Chem. Soc.* , 1997. **119**: p. 7019.
30. Battaglia, D., Li, J., Wang, Y., Peng, X., *Angew. Chem., Int. Ed. Engl.*, 2003. **42**: p. 5035.
31. Steckel, J., Zimmer, J.P., Coe-Sullivan., S., Stott, N.E., Bawendi, M.G., *Angew. Chem., Int. Ed. Engl.*, 2004. **43**: p. 2154.
32. Dabbousi, B.O., RodriguezViejo, J., Mikulec, F. V., Heine, J. R., Mattoussi, and R. H.; Ober, Jensen, K. F., Bawendi, M. G. , *J. Phys. Chem. B* 1997. **101**: p. 9463.
33. Reiss, P., Bleuse, J., Pron, A., *Nanolett.*, 2002. **2**: p. 781.
34. Mews, A., Eychmuller, A., Giersig, M., Schooss, D., Weller, H. , *J. Phys. Chem.*, 1994. **98**: p. 934.
35. Harrison, M.T., Kershaw, S. V., Rogach, A. L., Kornowski, A., Eychmüller, A., Weller, H. , *Adv. Mater.* , 2000. **12**: p. 123.
36. Kim, S., Fisher, B., Eisler, H.-J., Bawendi, M. G. , *J. Am. Chem. Soc.* , 2003. **125**: p. 11466.
37. Chen, C.-Y., Cheng, C.-T., Yu, J.-K., Pu, S.-C., Cheng, Y.-M., Chou, P.-T., Chou, Y.-H., Chiu, H.-T., *J. Phys. Chem. B* 2004 **108** p. 10687.
38. Hatami, F., Grundmann, M., Ledentsov, N. N., Heinrichsdorff, F., Bimberg, D., Ruvimov, S. S., Werner, P., Ustinov, V. M., Kopev, P. S., Alferov, Z. I. , *Phys. Rev. B* 1998. **57**: p. 4635.
39. Kim, S., Bawendi, M. G., *J. Am. Chem. Soc.*, 2003. **125**: p. 14652.
40. Huynh, W.U., Dittmer, J. J., Libby, W. C., Whiting, G. L., Alivisatos, A. P., *Adv Funct Mater*, 2003. **13**: p. 73.
41. Huynh, W.U., Dittmer, J. J., Alivisatos, A. P., *Science*, 2002. **295**: p. 2425.
42. Peng, X.G., Manna, L., Yang, W. D., Wickham, J., Scher, E., Kadavanich, A., Alivisatos, and A. P., *Nature*, 2000. **404**: p. 59.

43. Hikmet, R.A.M., Chin, P.T.K., Talapin, D.V., Weller, H., *Adv. Mater.*, 2005. **17**: p. 1346.
44. Cho, K., Talapin, D., Gaschler, W., Murray, C., *J. Am. Chem. Soc.*, 2005. **127**: p. 71470.
45. Li, M., Schnablegger, H., Mann, S., *Nature*, 1999. **402**: p. 393.
46. Li, Y.-D., Liao, H.-W., Ding Y., Qian, Y.-T., Yang, L., Zhou, G.-E. , *Chem. Mater.*, 1998. **10**: p. 2301.
47. Chen, C.-C., Chao, C.-Y., Lang, Z.-H. , *Chem. Mater.* , 2000. **12**: p. 1516.
48. Mohamed, M.B., Ismail, K. Z., Link, S., El-Sayed, M. A., *J. Phys. Chem. B* 1998. **102**: p. 9370.
49. Martin, B.R., Dermody, D. J., Reiss, B. D., Fang, M. M., Lyon, L. A., Natan, M. J., Mallouk, T. E. , *Adv. Mater.* , 1999. **11**: p. 1021.
50. Han, Y.J., Kim, J., Stucky, G. D. , *Chem. Mater.* , 2000. **12**: p. 2068.
51. Hu, J.T., Odom, T. W., Lieber, C. M., *Acc. Chem. Res.*, 1999. **32**: p. 435.
52. Trentler, T.J., Hickman, K. M., Goel, S. C., Viano, A. M., Gibbons, P. C., Buhro, W. E. , *Science*, 1995. **270**: p. 1791.
53. Trentler, T.J., Goel, S. C., Hickman, K. M., Viano, A. M., Chiang, M. Y., Beatty, A. M., Gibbons, P. C., Buhro, W. E. , *J. Am. Chem. Soc.*, 1997. **119**: p. 2172.
54. Manna, L., Scher, E. C., Aliatoviss, A. P. , *J. Am. Chem. Soc.*, 2000. **122**: p. 12700.
55. Peng, Z.A., Peng, X. , *J. Am. Chem. Soc.*, 2002. **124**: p. 3343.
56. Yong, k.T., Sahoo, Y., Swihart, M.T., Prasad, P.N., *Adv. Mater.*, 2006. **18**: p. 1978.
57. Wu, X., Liu, H., Liu, J., Haley, K. N., Treadway, J.A., larson, J. P., Ge, N. F., Peale, F., Bruchez, M. P., *Nat. Biotechnol.*, 2003. **21**: p. 41.
58. Jaiswal, J.K., Mattoussi, H., Mauro, J.M., Simon, S.M., *Nat. Biotechnol.*, 2003. **21**: p. 47.
59. Gao, X., Cui, Y., Levenson, R.M., Chung, L.W.K., Nie, S., *Nat. Biotechnol.*, 2004. **22**: p. 969.
60. Rosenthal, S.J., Tomlinson, I., Adkins, E. M., Schroeter, S., Adams, S., Swafford, L., McBride, J., Wang, Y., DeFelice, L. J., Blakely, R. D., *J. Am. Chem. Soc.*, 2004. **126**: p. 4586.

61. Goldman, E.R., Balighian, E. D., Mattoussi, H., Kuno, M. K., Mauro, J. M., Tran, P. T., Anderson, G. P., J. Am. Chem. Soc., 2002. **124**: p. 6378.
62. Pathak, S.C., S.-K., Arnheim, N., Thompson, M. E., J. Am. Chem. Soc., 2001. **123**: p. 4103.
63. Clapp, A.R., Medintz, I. L., Mauro, J. M., Fisher, B. R., Bawendi, M. G., Mattoussi, H., J. Am. Chem. Soc., 2004. **126**: p. 301.
64. Clapp, A.R., Medintz, I. L., Fisher, B. R., Anderson, G. P., Mattoussi, H., J. Am. Chem. Soc., 2006. **127**: p. 1242.
65. Mamedova, N.N., Kotov, N. A., Rogach, A. L., Studer, J., Nanolett., 2001. **1**: p. 281.
66. Trindade, T., Chem. Mater., 2001. **13**: p. 3843.
67. Brus, L.E., J. Chem. Phys., 1983. **79**: p. 5566.
68. Brus, L.E., J. Chem. Phys., 1984. **80**: p. 4403.
69. Potapova, I.F.C.u.P.J.G.-U., Mainz.
70. Finlayson, C.E., Optical Characterisation of Semiconductor Nanocrystals (PhD), and C. Churchill College, 162 (2001).
71. Weller, H., Schmidt, H. M., Koch, U., Fojtik, A., Baral, S., and A. Henglein, Kunath, W., Weiss, K., Deiman, E. , Chem. Phys. Lett., 1986. **124**: p. 557.
72. Schmidt, H.M., Weller, H. , Chem. Phys. Lett., 1986. **129**: p. 615.
73. Nosaka, Y., J. Phys. Chem., 1991. **95**: p. 5054.
74. Wang, Y., Herron, N. , J. Phys. Chem., 1991. **95**: p. 525.
75. Murray, C.B., Norris, D. J., Bawendi, M. G., J. Am. Chem. Soc. , 1993. **115**: p. 8706.
76. Norris, D.J., Sacra, A., Murray, C. B., Bawendi, M. G., Phys. Rev. Lett., 1994. **72**: p. 2612.
77. Nirmal, M., Brus, L. , Acc. Chem. Res., 1999. **32**: p. 407.
78. Norris, D.J., Bawendi, M. G., Phys. Rev. B, 1996. **53**: p. 16338.
79. Kuno, M., Lee, J. K., Dabbousi, B. O., Mikulec, F. V., Bawendi, M. G., J. Chem. Phys., 1996. **106**: p. 9869.
80. Yu, W.W., Qu, L., Guo, W., Peng, X. , Chem. Mater., 2003. **15**: p. 2854.
81. Qu, L., Peng, Z. A., Peng, X. , Nano Lett., 2001. **1**: p. 333.
82. Schmelz, O., Synthese und Oberflächenchemie von CdSe-Halbleiter-Nanokristallen and F.C.u.F. (Diplomarbeit), Johannes-Gutenberg Universität, Mainz, 85 (1999).

83. Leatherdale, C.A., Woo, W. K., Mikulec, F. A., Bawendi, M., , J. Phys. Chem., 2002. **106**: p. 7619.
84. Striolo, A., Ward, J., Prausnitz, J. M., Parak, W. J., Zanchet, D., Gerion, D., Milliron, D., Alivisatos, A. P., J. Phys. Chem. B, 2002. **106**: p. 5500.
85. Vossmeier, T., Katsikas, L., Giersig, M., Popovic, I. G., Diesner, K., Chemseddine, A., Eychmüller, A., Weller, H., , J. Phys. Chem., 1994. **98**: p. 7665.
86. Peng, X., Wickham, J., Alivisatos, A. P. , J. Am. Chem. Soc., 1998. **120**: p. 5343.
87. Talapin, D., Rogach, A., Haase, M., Weller, H., J. Phys. Chem. B, 2001. **105**: p. 12278.
88. Peng, Z.A., Peng, X., J. Am. Chem. Soc., 2001. **123**: p. 183.
89. Wang, Z.L., Liu, Y., Zhang, Z., In Handbook of Nanophase and Nanostructured Materials, New York, 2003, p 59.
90. Qu, L., Yu, W. W., Peng, X. , Nano Lett., 2004. **4**: p. 465.
91. Wang, X., Qu, L., Zhang, J., Peng, X., Xiao, M. , Nano Lett., 2003. **3**: p. 1103.
92. Peng, X., Wilson, T. E., Alivisatos, A. P., Schultz, P. G. , Angew. Chem., Int. Ed., 1997. **36**: p. 145.
93. Liberato, M., Erik, C. S., Alivisatos, A. P. , J. Am. Chem. Soc., 2000. **122**: p. 12700.
94. Yu, W.W., Peng, X. , Angew. Chem., Int. Ed., 2002. **41**: p. 2368.
95. Talapin, D.V., Haubold, S., Rogach, A. L., Kornowski, A., Haase, and W. M., H. , J. Phys. Chem. B 2001. **105**: p. 2260.
96. Gaponik, N., Talapin, D. V., Rogach, A. L., Hoppe, K., Shevchenko, and K. E. V., A., Eychmueller, A., Weller, H. , J. Phys. Chem. B, 2002. **106**: p. 7177.
97. Hines, M.A., Guyot-Sionnest, P. , J. Phys. Chem. B, 1998. **102**: p. 3655.
98. Lin, S.L., Pradhan, N., Wang, J. Y., Peng, X., Nano Lett., 2004. **4**: p. 2261.
99. Battaglia, D., Y., Peng, X., Nano Lett., 2002. **2**: p. 1027.
100. Steckel, J.S., Coe-sullivan, S., Bulovic, V., Bawendi, M. G., Adv. Mater., 2003. **15**: p. 1862.
101. Wehrenberg, B.L., Wang, C., Guyot-Sionnest, P. , J. Phys. Chem. B, 2002. **106**: p. 10634.
102. Murray, C.B., Sun, S., Gaschler, W., Doyle, H., Betley, T. A., and C.R. Kagan, J. Res. Rev., 2001. **45**: p. 47.

103. Pileni, M., *J. Phys. Chem.*, 1993. **97**: p. 6961.
104. Pileni, M.P., *Catal. Today*, 2000. **58**: p. 151.
105. Macbain, J.W., Salon, S., *J. Am. Chem. Soc.*, 1920. **43**: p. 426.
106. Liu, J., Kim, A. Y., Wang, L. Q., Palmer, B. J., Chen, Y. L., Bruinsma, P., Bunker, B. C., Exarhos, G. J., Graff, G. L., Rieke, P. C., Fryxell, G. E., Virden, J. W., Tarasevich, B. J., Chick, L., A., *Adv. Colloid Interface Sci.*, 1996. **69**: p. 131.
107. Fukui, T., Ando, S., Tokura, Y., Toriyama, T., *Appl. Phys. Lett.*, 1991. **58**: p. 2018.
108. Tanaka, S., Hirayama, H., Aoyagi, Y., Narukawa, Y., Kawakami, and F. Y., S., Fujita, S. , *Appl. Phys. Lett.*, 1997. **71**: p. 1299.
109. Hirayama, H., Tanaka, A., Ramvall, P., Aoyagi, Y., *Appl. Phys. Let.*, 1998. **72**: p. 1736.
110. Ishida, S., Arakawa, Y., Wada, K., *Appl. Phys. Lett.*, 1998. **72**: p. 800.
111. Peng, X.G., *Adv. Mater.*, 2003. **15**: p. 459.
112. Peng, Z.A., Peng, X. , *J. Am. Chem. Soc.*, 2001. **123**: p. 1389.
113. Link, S., Burda, C., Nikoobakht, B., El-Sayed, M. A. , *J. Phys. Chem. B*, 2000. **104**: p. 6152.
114. Manna, L., Milliron Delia, J., Meisel, A., Scher Erik, C., and A.P. Alivisatos, *Nat. Mater.*, 2003. **2**: p. 382.
115. Grebinski, J., Hull, K., Zhang, J., Kosel, T., Kuno, M., *Chem. Mater.*, 2004. **16**: p. 5260.
116. Steigerwald, M.L., Alivisatos, A. P., Gibson, J. M., Harris, T. and K. D., R., Muller, A. J., Thayer, A. M., Duncan, T. M., Douglass, D. C., Brus, L. E. , *J. Am. Chem. Soc.*, 1988. **110**: p. 3046.
117. Murray, C.B., Kagan, C. R., Bawendi, M. G. , *Science*. 1995. **270**: p. 1335.
118. Berry, C.C., Curtis, A. S. G. , *J. Phys. D* 2003. **36**: p. R198.
119. Pinaud, F., King, D., Moore, H.-P., Weiss, S., *J. Am. Chem. Soc.*, 2004. **126**: p. 6115.
120. Mattoussi, H., Mauro, J. M., Goldman, E. R., Anderson, G. P., Sundar, V. C., Mikulec, F. V., Bawendi, M. G., *J. Am. Chem. Soc.*, 2000. **122**: p. 12142.
121. Guo, W., Li, J. J., Peng, X. G., *Chem. Mater.*, 2003. **15**: p. 3125.
122. Hong, R., Fischer, N. O., Verma, A., Goodman, C. M., Emrick, T., Rotello, V. M., *J. Am. Chem. Soc.*, 2004. **126**: p. 739.

123. Michalet, X., Pinaud, F., Bentolila, L., Tsay, J., Doose, S., Li, J., Sundaresan, G., Wu, A., Garmbhir, S., Wweiss, S., *Science*, 2005. **307**: p. 538.
124. Gerion, D., Pinaud, F., Williams, S. C., Parak, W. J., Zanchet, D., Weiss, S.; Alivisatos, A. P., *J. phys. Chem. B*, 2001. **105**: p. 8861.
125. Parak, W.J., Gerion, D., Pellegrino, T., Zanchet, D., Micheel, C., Williams, S. C., Boudreau, R., Gros, M. A., Larabell, C. A., Alivisatos, A. P., *Nanotech.*, 2003. **14**: p. R15.
126. Uyeda, H.T., Medintz, I. L., Jaiswal, J. K., Simon, S. M., Mattoussi, H., *J. Am. Chem. Soc.*, 2006. **127**: p. 3870.
127. Pellegrino, T., Manna, L., Kudera, S., Liedl, T., Koktysh, D., Rogach, A. L., Keller, S., Radler, J., Natile, G., Parak, W. J., *Nano Lett.*, 2004. **4**: p. 703.
128. Osaki, F., Kanamori, T., Sando, S., Sera, T., Aoyama, Y., *J. Am. Chem. Soc.*, 2004. **126**: p. 6520.
129. Wang, X.-S., Dykstra, T. E., Salvador, M. R., Manners, I., Scholes, G. D., Winnik, M. A., *J. Am. Chem. Soc.*, 2004. **126**: p. 7784.
130. Baird, G., Zacharias, D., Tsien, R., *Proc. Natl Acad. Sci.*, 2000. **97**: p. 11984.
131. Medintz, I.L., Konnert, J. H., Clapp, A. R., Stanish, I., Twigg, M. E., Mattoussi, H., Mauro, J. M., Deschamps, J. R, *Proc. Natl. Acad. Sci.*, 2004. **101**: p. 9612.
132. Medintz, I.L., Clapp, A. R., Mattoussi, H., Goldman, E. R., Fisher, B., Mauro, J. M., *nature mater.*, 2003. **2**: p. 630.
133. Murphy, C.J., *Anal. Chem.*, 2002. **74**: p. 520A.
134. Niemeyer, C.M., *Angew. Chem. Int. Ed.*, 2001. **40**: p. 4128.
135. Alivisatos, A.P., *Nature Biotechnol.*, 2004. **22**: p. 47.
136. Gur, I., Fromer, N. A., Geier, M. L., Alivisatos, A. P., *Science*, 2005. **310**: p. 462.
137. Weller, H., *Angew. Chem., Int. Ed.* , 1998. **37**: p. 1658.
138. Klein, D.L., Roth, R., Lim, A. K. L., Alivisatos, A. P., McEuen, P. L. , *Nature*, 1997. **389**: p. 699.
139. Hakimi, F., Bawendi, M. G., Tumminelli, R., Haavisto, J. R., *U.S. Patent* 5, 1993. **260**: p. 957.
140. Steckel, J.S., Snee, P., Coe-Sullivan, S., Zimmer, J. R., Halpert, J. E., Anikeeva, P., Kim, L. A., Bulovic, V., Bawendi, M. G., *Angew. Chem. Int. Ed.*, 2006. **45**: p. 5796.

141. Zhao, J., Bardecker, J. A., Munro, A. M., Liu, M. S., Niu, Y., Ding, I.-K., Luo, J., Chen, B., Jen, A. K.-Y., Ginger, D. S., *Nano Lett.*, 2006. **6**: p. 463.
142. Yang, Y.A., Wu, H. M., Williams, K. R., Cao, Y. C., *Angew. Chem. Int. Ed.*, 2005. **44**: p. 6712.
143. Li, J.J., Wang, Y. A., Guo, W., Keay, J. C., Mishima, T. D., Johnson, M. B., Peng, X. G., *J. Am. Chem. Soc.*, 2003. **125**: p. 12567.
144. Spanhel, L., Haase, M., Weller, H., Henglein, A. , *J. Am. Chem. Soc.*, 1987. **109**: p. 5649.
145. Talapin, D.V., Rogach, A. L., Kornowski, A., Haase, M., Weller, H., *Nano Lett.*, 2001. **1**: p. 207.
146. Wang, Y.A., Li, J. J., Chen, H., Peng, X. , *J. Am. Chem. Soc.*, 2002. **124**: p. 2293.
147. Li, J.J., Wang, Y. A., Guo, W., Keay, J. C., Mishima, T. D., Johnson, M. B., Peng, X. G., *J. Am. Chem. Soc.*, 2005. **125**: p. 12567.
148. Stevenson, A.W., Barnea, Z., *Acta Crystallogr. Sect. B* 1984. **40**: p. 530.
149. Yeh, C., Lu, Z. W., Froyen, S., Zunger, A., *Phys. ReV. B*, 1992. **46**: p. 10086.
150. Saliba, S., Mardix, S. , *Acta Crystallogr., Sect. A* 1983. **39**: p. 933.
151. Scientific software Cerius2, m.e., Accelrys Inc., San Diego, CA.
152. Scherrer, P., *Go'tt. Nachr.*, 1918. **2**: p. 98.
153. Schoos, D., Mews, A., Eychmu'ller, A., Weller, H., *Phys. ReV. B* 1994. **49**: p. 17072.
154. Jun, S., Jang, E., *Chem. Commun.*, 2005: p. 4616.
155. Zhong, X.H., Han, M. Y., Dong, Z. L., White, T. J., Knoll, W. , *J. Am. Chem. Soc.*, 2003. **125**: p. 8589.
156. Zhong, X.H., Feng, Y. Y., Knoll, W., Han, M. Y. , *J. Am. Chem. Soc.*, 2003. **125**: p. 13559.
157. Zhong, X.H., Zhang, Z. H., Liu, S. H., Han, M. Y., Knoll, W., *J. Phys. Chem. B*, 2004. **108**: p. 15552.
158. Qu, L., Peng, X. , *J. Am. Chem. Soc.*, 2002. **124**: p. 2049.
159. Guo, W., Li, J. J., Wang, Y. A., Peng, X. G., *J. Am. Chem. Soc.*, 2003. **125**: p. 3901.
160. Nazzal, A.Y., Wang, X. Y., Qu, L. H., Yu, W., Wang, Y. J., Peng, X. G., and M. Xiao, *J. Phys. Chem. B* 2004. **108**: p. 5507.

161. Schmelz, O., Mews, A., Basche, T., Herrmann, A., Mullen, K. , Langmuir, 2001. **17**: p. 2861.
162. Wang, W.Z., Germanenko, I., El-Shall, M. S. , Chem. Mater., 2002. **14**: p. 3028.
163. Talapin, D.V., Mekis, I., Gotzinger, S., Kornowski, A., Benson, O., Weller, H., J. phys. Chem. B, 2004. **108**: p. 18826.
164. Aharoni, A., Mokari, T., Popov, I., Banin, U., J. Am. Chem. Soc., 2006. **128**: p. 257.
165. Xie, R., Kolb, U., Li, J., Basche, T., Mews, A., J. Am. Chem. Soc., 2005. **127**: p. 7480.
166. Li, J., Wang, X., Peng, X., Angew. Chem. Int. Ed., 2003. **42**: p. 5035.
167. Jun, K., Choi, C., Cheon, J., Chem. Commun., 2001: p. 101.
168. Resch, U., Weller, H., Henglein, A., Langmuir, 1989. **5**: p. 1015.
169. Li, Y., Ding, Y., Wang, Z., Adv. Mater., 1999. **11**: p. 847.
170. Wilke, W., Maierhofer, C., Horn, K.J. Vacuum Science and Technology B 1990, 8, 760., J. Vacuum Science and Technology B, 1990. **8**: p. 760.
171. Mikes, R., Wu, G., Johnson, M., McGill, T., Faurie, J., Sivananthan, S. , Appl. Phys. Lett., 1986. **48**: p. 1383.
172. Su, W., Ya, M., Chiu, Y., Chen, Y., Phys. Rev. B, 2002. **66**: p. 113305.
173. Laheld, U., Pedersen, F., Hemmer, P., Phys. Rev. B, 1995. **52**: p. 2697.
174. Geerts, Y., Quante, H., Platz, H., Mahrt, R., Hopmeier, M., Böhm, A., Müllen, K., J. Mater. Chem., 1998. **8**: p. 2357.
175. Lieber, C.M., solid state commun., 1998. **107**: p. 607.
176. Prasad, P.N., Nanophotonics, Wiley-Interscience, New York, 2004.
177. Du, H., Chen, C., Krishnan, R., Krauss, T. D., Harbold, J. M., Wise, and T. F. W., M. G., Silcox, J. , Nano Lett., 2002. **2**: p. 1321.
178. Pietryga, J.M., Schaller, R. D., Werder, D., Stewart, M. H., Klimov, and H. V. I., J. A. , J. Am. Chem. Soc., 2004. **126**: p. 11752.
179. Duan, X., Huang, Y., Cui, Y., Lieber, C. M., Nature, 2001. **409**: p. 66.
180. Zhong, Z., Qian, F., Wang, D., Lieber, C. M., Nano Lett., 2003. **3**: p. 343.
181. Cui, Y., Lieber, C. M., Science, 2001. **291**: p. 851.
182. Huang, Y., Duan, X., Cui, Y., Lauhon, L., Kim, K., Lieber, C. M, Science, 2001. **294**: p. 1313.
183. Lieber, C.M., Sci. Am., 2001. **285**: p. 58.

184. Lieber, C.M., MRS Bull., 2003. **28**: p. 486.
185. Morales, A.M., Lieber, C. M., Science, 1998. **279**: p. 208.
186. Wu, Y., Yang, P. , J. Am. Chem. Soc., 2001. **123**: p. 3165.
187. Tang, Z., Kotov, N. A., Giersig, M., Science, 2002. **297**: p. 237.
188. Shah, P.S., Novick, B. J., Hwang, H. S., Lim, K. T., Carbonell, R. G., Johnston, K. P., Korgel, B. A., Nano Lett., 2003. **3**: p. 1671.
189. Ohde, H., Ohde, M., Bailey, F., Kim, H., Wai, C. M., Nano Lett., 2002. **2**: p. 721.
190. Holmes, J.D., Bhargava, P. A.; Korgel, B. A., Johnston, K. P., Langmuir, 1999. **15**: p. 6613.
191. Sun, Y.P., Rollins, H. W. , Chem. Phys. Lett., 1998. **288**: p. 585.
192. Yu, W.W., Wang, Y. A., Peng, X., Chem. Mater., 2003. **15**: p. 4300.
193. Milliron, D.J., Hughes, S. M., Cui, Y., Manna, L., Li, J. B., Wang, L. W., Alivisatos, A. P, Nature, 2004. **430**: p. 664.
194. Kanaras, A.G., Sonnichsen, C., Liu, H., Alivisatos, A. P., Nano Lett., 2005. **5**: p. 2164.
195. Zhong, X., Xie, R., Zhang, Y., Basche, t., Knoll, W., Chem. Mater., 2005. **17**: p. 4038.
196. Talapin, D.V., Koeppel, R., Go'tzinger, S., Kornowski, A., Lupton, J. and R. M., A. L., Benson, O., Feldmann, J., Weller, H. , Nano Lett., 2003. **3**: p. 1677.
197. Jun, M., Lee, M., Kang, J., Cheon, J., J. Am. Chem. Soc., 2001. **123**: p. 5350.
198. Gao, F., Liu, Q., Xie, Q., Zhao, D., Adv. Mater., 2002. **14**: p. 1537.
199. Yang, J., Xue, C., Yu, S., Zeng, J., Qian, Y., , Angew. Chem. Int. Ed., 2002. **41**: p. 4697.
200. Li, Y., Liao, H., Ding, Y., Qian, Y., Yang, L., Zhou, G., Chem. Mater., 1998. **10**: p. 2301.
201. Simmons, B., Li, S., John, V., Macpherson, G., Zhou, W., He, J., Nano Lett., 2002. **2**: p. 263.
202. Cozzoli, P.D., Manna, L., Curri, M. L., Kudera, S., Giannini, C., Striccoli, M., Agostiano, A., Chem. Mater., 2005. **17**: p. 1296.
203. Jun, Y., Jung, Y., Cheon, J., J. Am. Chem. Soc., 2004. **124**: p. 615.
204. Xie, R., Zhong, X. Basche, T., Adv. Mater., 2005. **17**: p. 2741.
205. Jun, Y., Lee, S., Kang, N., Cheon, J., J. Am. Chem. Soc., 2001. **123**: p. 5150.
206. Li, L., Hu, J., Yang, W., Alivisatos, A. P., Nano Lett., 2001. **1**: p. 349.

207. Hu, J., Li, L. S., Yang, W., Manna, L., Wang, L., Alivisatos, A. P., *Science*, 2001. **292**: p. 2060.
208. Li, L.S., Pradhan, N., Wang, Y., Peng, X., *Nano Lett.*, 2004. **4**: p. 2261.
209. Potapova, I., Mruk, R., Hubner, C., Zentel, R., Basche, T., Mews, A., *J. Am. Chem. Soc.*, 2003. **125**: p. 320.
210. Clapp, A.R., Medintz, I. L., Mauro, J. M., Fisher, B. R., Bawendi, M. G., and H. Mattoussi, *J. Am. Chem. Soc.* , 2004. **126**: p. 301.
211. Potapova, I., Mruk, R., Hubner, C., Zentel, R., Basche, T., Mews, A., *Angew. Chem. Int. Ed.*, 2005. **44**: p. 2437.
212. Jin, T., Fujii, F., Sakata, H., Tamura, M., Kinjo, M., *Chem. Comm.*, 2005: p. 2829.
213. Tomasulo, M., Yildiz, I., Raymo, F. M., *J. Phys. Chem. B*, 2006. **110**: p. 3835.
214. Feng, J., Ding, S., Tucker, M., Hemmel, M., Kim, Y., Zhang, S., Keyes, B., Rumbles, g., *Appl. Phys. Lett.*, 2005. **86**: p. No.033108.
215. Eliseev, A.V., *J. Am. Chem. Soc.*, 1994. **116**: p. 6081.
216. Hacket, F., Simova, S., Schneider, H. J., *J. Phys. Org. Chem.*, 2001. **14**: p. 159.
217. Depalo, N., Comparelli, R., Striccoli, M., Curri, M. L., Fini, P., Giotta, L., Agostiano, A., *J. Phys. Chem. B*, 2006. **110**: p. 17388.
218. Nishijo, J., Nagai, M., Yasuda, M., Ohno, E., Ushiroda, Y., *J. Pharm. Sci.*, 1995. **84**: p. 1420.
219. Dotsikas, Y., Kontopanou, E., Allagiannis, C., Loukas, Y. L., *J. Pharm. Biomed. Anal.*, 2000. **23**: p. 997.
220. Szejtli, J., *Chem. Rev.*, 1998. **98**: p. 1743.
221. Skoulika, S., Georgiou, C., Polissiou, M., *J. Incl. Phen. Macr. Chem.*, 1999. **34**: p. 85.
222. Nazzal, A.Y., Qu, L.; Peng, X., Xiao, M., *Nano Lett.*, 2003. **3**: p. 819.
223. Lakowicz, J., R. *Principles of Fluorescence Spectroscopy*, 2nd., Kluwer Academic, New York, 1999.
224. Turro, N., *J. Modern Molecular Photochemistry*, University Science Books, Mill Vally, CA, 1991.
225. Chan, W.C.W., Nie, S., *Science* 1998, . **281**: p. 2016.